HAL open science

The high-frequency dynamics of liquids and supercritical fluids

Filippo Bencivenga

To cite this version:

Filippo Bencivenga. The high-frequency dynamics of liquids and supercritical fluids. Fluid Dynamics [physics.flu-dyn]. Université Joseph-Fourier - Grenoble I, 2006. English. NNT : . tel-00121509

HAL Id: tel-00121509

https://theses.hal.science/tel-00121509v1

Submitted on 20 Dec 2006

HAL is a multi-disciplinary open access archive for the deposit and dissemination of scientific research documents, whether they are published or not. The documents may come from teaching and research institutions in France or abroad, or from public or private research centers.

L'archive ouverte pluridisciplinaire **HAL**, est destinée au dépôt et à la diffusion de documents scientifiques de niveau recherche, publiés ou non, émanant des établissements d'enseignement et de recherche français ou étrangers, des laboratoires publics ou privés.

THESE DE DOCTORAT DE L'UNIVERSITE
JOSEPH FOURIER

Spécialité

PHYSIQUE

présentée par

M. Filippo BENCIVENGA

Pour obtenir le grade de

DOCTEUR de l'UNIVERSITE JOSEPH FOURIER

Dynamique à haute fréquence des systèmes liquides et supercritiques

soutenue le 13 Octobre 2006

devant le jury composé de:

Mr. Hubert RENEVIER	Président
MM. Jean-Pierre BOON, Lars BÖRJESSON	Rapporteurs
MM. Giancarlo RUOCCO, Walter KOB	Examinateurs
MM. Francesco SETTE, Michael KRISCH	Directeurs de thèse

THESE PREPAREE AU SEIN DU LABORATOIRE:
EUROPEAN SYNCHROTRON RADIATION FACILITY - GRENOBLE

The high frequency dynamics of liquids and supercritical fluids

Filippo Bencivenga

A Marta

Contents

Contents **3**

Introduction (français) **7**

Introduction **11**

1 The liquid-vapor phase transition **17**
1.1 Liquid-vapor phase transition and critical point 17
1.2 van der Waals equation of state 20

2 Fluctuations and Hydrodynamics **27**
2.1 Introduction 27
2.2 Fluid dynamics: time correlation functions 28
2.2.1 Static correlation functions 31
2.2.2 Frequency sum rules 32
2.3 Classical approach: hydrodynamic limit 33
2.3.1 Mass conservation 33
2.3.2 Momentum conservation 33
2.3.3 Energy conservation 34
2.3.4 Linearized hydrodynamics and Rayleigh-Brillouin spectrum . . . 35
2.4 The memory function approach 40
2.4.1 Rephrasing of the many body dynamical problem 40
2.4.2 Time dependence of the memory function 41
2.4.3 The case of density fluctuations 43
2.4.4 Relaxation processes 45
2.4.5 The proposed memory function 52
2.5 The single particle limit 53

3 Inelastic X-Ray Scattering from fluids **57**
3.1 IXS cross-section 57
3.2 Dynamic structure factor and phonons 61
3.3 X-rays or Neutrons? 62
3.4 IXS spectrometer: beamline ID-28 at ESRF 65
3.5 Experimental apparatus 69
3.5.1 The Cunsolo cell 69
3.5.2 Low temperature assembly for neon and nitrogen 71

3.5.3 High temperature assembly for water 71
3.5.4 Set-up for ammonia and supercritical water 73

4 Experimental results 77
4.1 Choice of the samples and thermodynamic path 77
4.2 Data analysis 81
4.2.1 Data treatment 82
4.2.2 Model function 83
4.2.3 Fitting procedure 84
4.2.4 Longitudinal current spectra 85
4.2.5 Viscosity 92
4.2.6 Comparison with structural data 92
4.3 Experimental results 93
4.3.1 Dispersion relations 93
4.3.2 Structural relaxation 99
4.3.3 Instantaneous relaxation 102
4.3.4 Viscosity 104
4.4 Conclusions 106

5 The high-frequency dynamics of liquids and supercritical fluids 109
5.1 Sound dispersion 109
5.1.1 Positive sound dispersion 109
5.1.2 "Negative" sound dispersion 111
5.2 Structural relaxation 113
5.2.1 Strength of structural relaxation 113
5.2.2 Timescale of structural relaxation 114
5.2.3 Compliance relaxation time 116
5.3 Instantaneous relaxation 120

Conclusions 123

Conclusions (français) 125

References 128

Introduction

L'existence de trois états d'agrégation de la matière, qui se transforment l'un dans l'autre, est un phénomène commun dans l'expérience quotidienne : l'eau se transforme en vapeur et la vapeur en glace. Ces changements d'états d'agrégation s'appellent transitions de phase. Les mouvements incessants de l'eau d'une phase à l'autre sont une condition "sine qua non" pour la vie sur Terre. Les transitions de phase ont toujours eu la plus grande importance technologique, et donc politique et culturelle : la fusion des métaux pour faire des épées, l'évaporation de l'eau dans un moteur à vapeur, la condensation de l'essence dans une raffinerie de pétrole ... La liste pourrait être facilement plus longue que cette thèse.

La première tentative de décrire les diverses phases de la matière et de leurs transitions a été entreprise par le philosophe grec Aristote [1]. Selon cette illustre personne tout dans le monde se compose de la combinaison de quatre éléments : terre, eau, feu et air. Le but final de chaque élément est d'arriver à rejoindre son "endroit naturel". Par exemple la mer est l'endroit normal pour l'eau. Par conséquent la pluie, qui est "un peu d'eau dans le ciel", chute vers le bas et, par les fleuves, entre dans la mer.

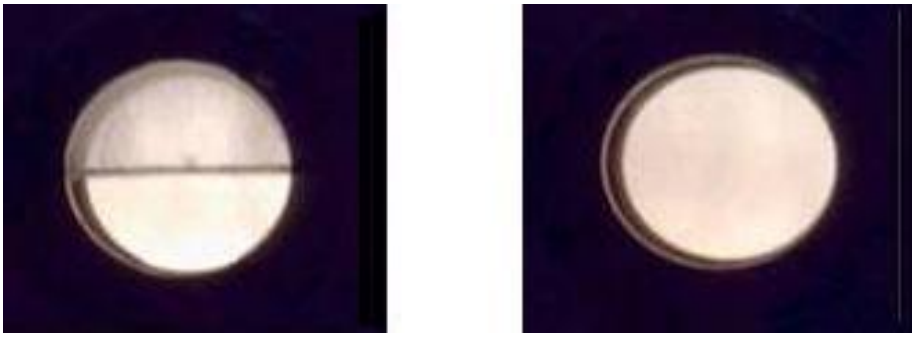

Figure 1: Panneau à gauche: un liquide en équilibre avec sa vapeur. Panneau à droite: le même liquide après avoir été chauffé au-dessus de la température critique.

Si nous regardons la photo à gauche sur la figure 1 nous pouvons voir une situation très courante. Un liquide (dans le fond) est en équilibre avec sa vapeur (dessus), les deux phases sont clairement séparées. Aristote expliquerait cette situation de la façon suivante : le liquide est principalement fait d'eau et cette eau tend à aller vers le bas pour arriver à la mer, tandis que la vapeur est fait principalement d'air et tend à aller au ciel, son "endroit naturel".

La vision aristotélicienne du monde a été conservée pendant 20 siècles. Peut-être que sa vision du monde aurait été révisée plus tôt, si Aristote avait eu la possibilité de chauffer l'eau au-dessus de 647 K et d'appliquer une pression plus grande que 221 bar. Dans ce cas lá il aurait observé la situation rapportée dans l'image à droite de la figure 1, cas dans laquel le système est homogène, les deux "éléments" sont remplacés par un seul. D'une part le nouvel élément est "similaire à l'air", puisqu'il est volatile si on casse le gobelet. D'autre part le nouvel élément est "similaire à l'eau", puisqu'il est visqueux et ne transmet pas la lumière sans la perturber. En outre, si on le refroidit en augmentant ou diminuant la pression, on peut obtenir soit seulement de la vapeur soit seulement de l'eau. Comment Aristote aurait-il expliqué ceci ?

Aujourd'hui nous savons que chaque matériau peut exister dans trois états différents d'agrégation : solide, liquide et vapeur. Chacune de ces phases a ses caractéristiques : un solide a toujours un volume et une forme bien définis ; un liquide n'a pas de forme définie, mais il a un volume précis ; une vapeur n'a ni forme ni volume bien définis.

Par certaines valeurs de température et de pression, le système peut changer son état d'agrégation, c'est-à-dire il peut subir une transition de phase de premier ordre. Par exemple lors du refroidissement, une quantité de chaleur différente de zéro, la chaleur latente, est échangée avec l'environnement dans un intervalle de température infinitésimal autour de la température de transition. Dans le cas de l'eau une chaleur latente de 334 KJ est libérée par les molécules pour s'organiser elles-mêmes dans un réseau cristallin de glace.

Si nous voulons expliquer la phénoménologie montrée sur la figure 1, nous devrions souligner la première faute que j'ai faite dans cette thèse : la déclaration que la transition de phase liquide-vapeur est de premiér ordre. Ce n'est pas toujours vrai, puisque dans certaines circonstances le liquide peut se transformer en vapeur (et vice versa) sans changer aucune chaleur latente avec l'environnement. Ceci est possible quand on contourne le point critique. C'est un unique point singulier dans le diagramme de phases, au-delà duquel la distinction entre liquide et vapeur n'est plus significative.

Pourquoi est-ce que ceci se produit ? Imaginons que l'on chauffe un liquide dans un récipient fermé. Quand la température augmente la quantité de liquide qui se convertit en vapeur augmente, la pression et la densité de vapeur sont donc plus grandes. En même temps le liquide se dilate ; par conséquent la différence entre la densité du liquide et de la vapeur diminue jusqu'à une certaine température, la température critique (T_c), où cette différence disparaît. Au-dessus de T_c le liquide et la vapeur cessent d'être des entités différentes et le système devient homogène : c'est la phase supercritique.

Récemment les propriétés particulières des fluides supercritiques ont trouvé de nombreuses applications pratiques, qui s'étendent de la nanotechnologie [2] au traitement des déchets dangereux [3, 4]. Par exemple, un réacteur chimique utilisant l'oxydation de l'eau supercritique (SCWO) a été développé récemment, et est employé pour traiter un large éventail de déchets dangereu. Dans la plupart des cas une efficacité de 99.99 % à été obtenue. D'ailleurs, pour une concentration de déchets plus haute que 1 %, le processus est autoentretenu et l'excès de chaleur de la réaction peut être récupéré pour d'autres usages. Il y a aussi le potentiel pour développer des usines de production d'électricité, alimentées par déchets dangereux, basées sur SCWO. C'est, peut-être, l'application finale de SCWO : nettoyer l'environnement et, en même temps, produire

de l'énergie.

D'un point de vue scientifique, de nombreuses études expérimentales et théoriques sur les fluides critiques et supercritiques ont été réalisées depuis la découverte de l'état critique en 1822 par Charles baron Cagniard de la Tour. Aujourd'hui les propriétés macroscopiques (thermodynamiques) des liquides, vapeurs et fluides supercritiques, ainsi que leur structure microscopique, sont bien comprises.

En revanche la connaissance de la dynamique microscopique de ces systèmes est tout à fait insuffisante. Pour cette raison nous avons décidé d'étudier de façon expérimentale la dynamique microscopique des fluides supercritiques. Afin de réaliser une étude générale et systématique nous avons choisi de sonder quatre systèmes différents, dans la phase liquide et supercritique. Les systèmes étudiés sont deux liquides qui présentent des liaisons hydrogènes (l'eau et l'ammoniaque), un liquide moléculaire (l'azote) et un liquide simple (le néon).

Ces systèmes ont été choisis aussi parce qu'ils peuvent être considérés comme des représentants de classes de matériaux. En effet ils possèdent des intéractions et structures intermoléculaires très différentes : la molécule d'eau possède deux liaisons hydrogènes par molécule, avec un rapport donneur/accepteur égal à 1. En autre l'eau présente une structure intermoléculaire presque parfaitement tétraédrique. Ces propriétés fait de l'eau un liquide très structuré et coordonné, même sur des distances plus grandes que la distance typique entre deux molécules. Même l'ammoniaque a des liaisons hydrogènes mais avec un rapport donneur/accepteur déséquilibré (1/3). En conséquence les molécules d'ammoniaque ne peuvent former qu'une seule liaison entre elles. Pour cette raison la structure et le degré de coordination sont beaucoup plus petits que dans l'eau. Le néon comme l'azote ne possèdent pas de liaisons hydrogènes, mais de plus faibles liaisons de van der Waals. En outre le néon présente la structure intramoléculaire la plus simple possible (monoatomique).

Pour enquêter sur la dynamique microscopique d'un système nous avons besoin d'une sonde microscopique et d'une technique sensible à la dynamique. Jusqu'à il y a 10 ans la seule technique expérimentale qui pouvait satisfaire les deux conditions était la Diffusion Inélastique de Neutron (INS). Biènque la technique INS soit un instrument formidable pour ce type d'études, elle a une limite intrinsèque très forte : une gamme dynamique limitée. Cette limitation empêche les neutrons de mesurer la dynamique à hautes valeurs d'énergie échangée (c'est-à-dire à hautes fréquences : ω) et à petites valeurs de moment transféré : Q. De nos jours le développement de la Diffusion Inélastique de Rayons-X (IXS) a fourni une puissante technique complémentaire pour enquêter sur la dynamique microscopique de matériaux. En particulier dans les systèmes désordonnés, l'IXS dépasse certaines des restrictions présentes intrinsèquement dans les expériences d'INS, plus précisément la technique IXS n'a aucune limitation de gamme dynamique. La quantité expérimentelement observable, tant dans les expériences IXS que d'INS, est la transformée de Fourier de la fonction de corrélation de couple de la densité atomique. Cette quantité est communément appelée le facteur de structure dynamique, $S(Q,\omega)$. Il contient toutes les informations pertinentes sur la structure et la dynamique. Ces informations contenues dans $S(Q,\omega)$ concernent des échelles de longueur, λ, et de temps, τ, du même ordre que $1/Q$ et $1/\omega$. Dans le cas d'un système désordonné il est possible de calculer formellement $S(Q,\omega)$ seulement

dans deux cas limites :

- " aux petites valeurs du moment transféré, appelé la limite hydrodynamique. Ici le système est décrit, d'une façon macroscopique, par la théorie hydrodynamique classique [5].
- aux valeurs très élevées du moment transféré, appelé la limite de particule unique. Ici il n'est pas possible d'obtenir des informations sur la dynamique collective [6].

Dans ce travail de thèse nous exploitons principalement la région intermédiaire du moment transféré, c'est-à-dire la région habituellement appelée " mésoscopique ". Cette région est caractérisée par des valeurs de moment transféré près de l'inverse des distances intermoléculaires moyennes (typiquement quelques $\mathring{A}$) et, par conséquent, un développement de la théorie microscopique de la dynamique des liquides est nécessaire. De nos jours il y a de nombreuses façons de décrire ces dynamiques microscopiques. Parmi ces théories, pour décrire nos données expérimentales, nous avons choisi la théorie de l'hydrodynamique moléculaire [7, 8]. Elle est basée sur le formalisme de la fonction mémoire et sur le concept des processus de relaxation. Cette théorie peut très bien décrire la phénoménologie observée expérimentalement. Notre but est de comprendre comment la phénoménologie caractéristique de la phase liquide évolue tandis que le système approche et entre dans la phase supercritique. En particulier notre attention est concentrée sur les excitations collectives, et en particulier sur les modes acoustiques longitudinaux. Les processus de relaxation utilisés pour décrire la dynamique microscopique sont examinés en fonction de l'état thermodynamique des systèmes étudiés, ainsi que leur évolution avec l'augmentation de degré de connectivité du système. Ceci a été rendu possible par une comparaison complète des résultats obtenus pour différents échantillons.

Ce travail de thèse est organisé comme suit:

- Le chapitre 1 est consacré à un bref examen des concepts fondamentaux de la transition de phase liquide-vapeur, avec l'exemple de l'équation d'état de van der Waals.
- Dans le chapitre 2 est développé le formalisme nécessaire pour décrire la dynamique des fluides. Les résultats concernant la limite hydrodynamique et de particule unique sont discutés. En outre, la théorie hydrodynamique moléculaire est présentée avec quelques exemples didactiques.
- Le chapitre 3 discute la technique de la Diffusion Inélastique des Rayon-X comme outil pour étudier la dynamique à hautes fréquences des systèmes désordonnés. L'installation expérimentale est décrite, ainsi que les équipements à haute pression utilisés.
- Le chapitre 4 présente les expériences effectuées, l'analyse de données et les résultats expérimentaux obtenus pour chaque système étudié.
- Le chapitre 5 est focalisé sur la comparaison quantitative entre les résultats obtenus pour différents échantillons. Enfin, une image globale de la phénoménologie observée expérimentalement est fournie.

Introduction

The existence of three aggregate states of matter, that turn one into the other, is a common phenomenon in everyday experience: water transforms into steam and steam into ice. These changes in the nature of the aggregate are called phase transitions. The endless movements of water from one phase to the other is a condition "sine qua non" for life on Earth. Since the earliest time phase transitions were of the greatest technological (and therefore political and cultural) importance: the melting of metals to make swords, the evaporation of water in a steam engine, the condensation of gasoline in an oil refinery ... The list could easily be longer than this thesis itself.

The first attempt to describe the various phases of matter and their transitions was undertaken by the Greek philosopher Aristotle [1]. According to this distinguished personality everything in the world is composed of a weighted combination of four elements: rock, water, fire and air. The ultimate aim of each element is to join its "natural place". For instance the sea is the natural place for water. Therefore the rain, that is "some water in the air", falls down and, through the rivers, goes into the sea.

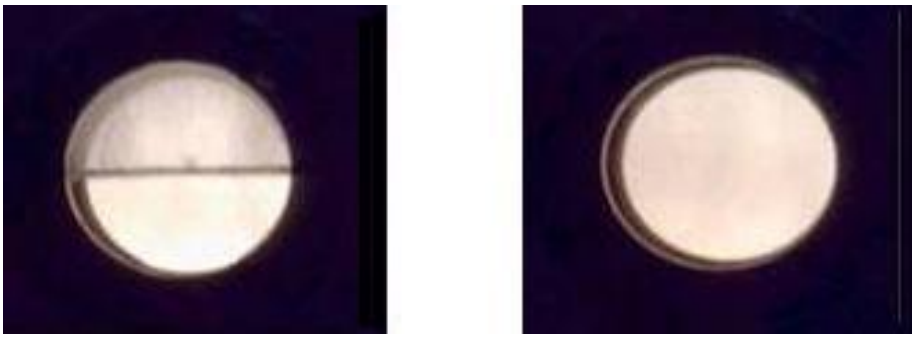

Figure 2: Left panel: a liquid in equilibrium with its vapor. Right panel: the same liquid after being heated above the critical temperature.

If we look at the left photo in figure 1 we can see a very common situation. A liquid (on the bottom) is in equilibrium with its vapor (on the top), and the two phases are clearly separated. This situation was explained by Aristotle in the following way: the liquid, whatever it is, is mainly made out of water and it tends to flow down and join the sea while the vapor is made out of air and it tends to join the sky, its "natural place".

The Aristotelian vision of the world held for nearly 20 centuries. Perhaps his vision would have been revisited earlier, if Aristotle had had the possibility to heat water above 647 K and to apply a pressure greater than 221 bar. In this case he would have observed the situation reported in the right picture of figure 1: the system becomes homogeneous, and the two "elements" are replaced by only one. On one hand the new element is "air-like", since it is volatile if one breaks the ampulla. On the other hand it is "water-like", since it is viscous and does not transmit light unperturbed. Furthermore, on cooling down with either an increase or a decrease in pressure, one obtains water or air, respectively. How would have Aristotle explained this?

Today we know that each material can exist in three different aggregation states: solid, liquid and vapor. Each of these phases has its characteristic features: a solid always has a well defined volume and shape; a liquid does not have a defined shape, but it has a precise volume; a vapor does not have a proper shape or volume.

In specific conditions of temperature and pressure the system can change its state of aggregation, undergoing a so-called first-order phase transition. For example by cooling a non-zero quantity of heat, i.e. the latent heat, is exchanged with the environment in an infinitesimally small range of temperature around the transition temperature. For instance a latent heat of 334 J/g is released by water molecules in order to pack themselves together in a crystalline ice lattice.

If we want to explain the phenomenology shown in figure 1, we should underline the first mistake I did in writing this thesis: the statement that the liquid-vapor phase transition is a first order transition. This is not always true, since under certain circumstances the liquid can transform into vapor (and vice-versa) without involving any latent heat. This is possible by circumventing the critical point, a unique singular point in the thermodynamic plane, above which the distinction between the liquid and vapor is no longer meaningful.

Why does this happen? Imagine heating a closed vessel. When the temperature increases, the quantity of liquid that converts into vapor increases, and so do the vapor pressure and density. Meanwhile the liquid expands thereby decreasing the difference between the liquid and the vapor density; finally, at a certain temperature, i.e. the critical temperature (T_c), this difference vanishes. Above T_c the liquid and the vapor cease to be different entities and the system becomes homogeneous: this is the supercritical phase.

Recently the unique properties of supercritical fluids have found a host of practical applications, ranging from nanotechnology [2] to the treatment of hazardous wastes [3, 4]. For example, a chemical reactor employing supercritical water oxidation (SCWO) has been recently developed, and is used to treat a wide range of hazardous wastes. In most of the cases a 99.99 % destruction and removal efficiency is obtained. Moreover, for waste concentrations higher than 1 %, the process is self-sustaining and the excess heat of reaction can be recovered for use within the process or for external purposes. There is also potential for developing SCWO power generation plants fuelled by raw biomass slurries. This could be the ultimate application of SCWO: cleaning the environment while producing energy.

On the scientific side, experimental and theoretical studies on critical and supercritical fluids have been performed since the discovery of the critical state in 1822 by

Charles Baron Cagniard de la Tour. Today the macroscopic (thermodynamic) properties of liquids, vapors and supercritical fluids, as well as their microscopic structure, are well understood.

The knowledge, however, of their microscopic dynamics is quite poor. For this reason we decided to experimentally investigate the microscopic dynamics of supercritical fluids. In order to achieve a general and systematic study we chose to probe four different systems, in their respective liquid and supercritical phases. The investigated systems are two common hydrogen bonded liquids: water (H_2O) and ammonia (NH_3), a molecular liquid, nitrogen (N_2), and a simple liquid, neon (Ne). They possess very different intermolecular interactions, ranging from strong hydrogen bonds (water) to weak van der Waals bonds (neon).

In order to investigate the microscopic dynamics of a bulk system we need a microscopic probe and a technique sensitive to the dynamics. Up to 10 years ago the only experimental technique that could satisfy both conditions was Inelastic Neutron Scattering (INS). Nowadays Inelastic X-ray Scattering (IXS) has become a powerful complementary technique to investigate the microscopic dynamics of bulk materials. In particular, in disordered systems, IXS overcomes some of the limitations intrinsically present in INS experiments. The experimental observable, in both IXS and INS experiments, is the power spectrum of the atomic density-density pair correlation function, the so-called dynamical structure factor, $S(Q,\omega)$. It contains all the relevant information on the structure and the dynamics. The $S(Q,\omega)$ of a disordered system is formally well known only in two limiting and restrictive cases:

- At small momentum transfer, in the hydrodynamic limit. Here the $S(Q,\omega)$ is described, in a macroscopic fashion, by the classical hydrodynamic theory [5].
- At very high momentum transfer, in the single particle limit [6].

In this thesis work we mainly exploit the intermediate momentum transfer region, usually called "mesoscopic" region. Here the momentum transfer values are close to the inverse of the average intermolecular distances (usually a few $\mathring{A}$), and consequently a microscopic picture of the liquid dynamics is needed. The molecular hydrodynamic theory, based on the memory function formalism and on the concept of relaxation processes, is able to describe the common phenomenology experimentally observed [7, 8]. Therefore this is the formalism employed to describe our data. The aim is to understand how the phenomenology characteristic of the liquid phase evolves while the system approaches and enters the supercritical phase. In particular, our attention is focused on the influence of the local, microscopic dynamics on the collective one. The relevant relaxation processes used in describing the microscopic dynamics are examined as a function of the thermodynamic state of the investigated systems. Their evolution with increasing degree of connectivity of the system is investigated. Finally, a comprehensive comparison of the results obtained for different samples is given.

The work is set out according to the following scheme:

- Chapter 1 is dedicated to a brief review of the fundamental concepts of the liquid-vapor phase transition.

- Chapter 2 is devoted to the description of fluid dynamics. The exact results concerning the hydrodynamic and single particle limit are discussed. Finally, the molecular hydrodynamic theory is presented together with some didactic examples.
- Chapter 3 discusses the Inelastic X-ray Scattering technique as a tool to study the dynamics of disordered systems. The experimental set-up is described, as well as the high-pressure equipments utilized.
- Chapter 4 presents the experimental data and the data analysis. The main results for the investigated systems are given.
- Chapter 5 is dedicated to the results concerning the comparison between the different samples. A global picture of the observed phenomenology is provided.

Résumé du chapitre 1

Le but du chapitre 1 est de discuter de la transition de phase liquide-vapeur et de l'état supercritique d'un point de vue thermodynamique. Une brève introduction aux concepts thermodynamiques est fournie. De plus, l'équation d'état de van der Waals est discutée comme un exemple didactique. L'accent est donné à l'universalité de cette équation d'état, soulignée par l'introduction de la loi d'états correspondants.

Chapter 1

The liquid-vapor phase transition

In the first section of this chapter the fundamental concepts of the liquid-vapor phase transition will be introduced, together with the concept of the critical point. In section 1.2 the van der Waals equation of state is briefly discussed as the didactic example.

1.1 Liquid-vapor phase transition and critical point

The liquid-vapor phase transition is a very common physical phenomenon in everyday life. Together with the solid-liquid transition it is the most didactic example of phase transitions. It takes place at specific values of the thermodynamic parameters pressure (P_t) and temperature (T_t). The whole set of (P_t, T_t)-values is called the liquid-vapor coexistence line. Liquids can be transformed into vapor, and vice-versa, by slightly varying pressure or temperature across the respective coexistence values (P_t and T_t). These transitions involve the exchange of a certain amount of heat -the latent heat- with the environment[1]. For instance a latent heat of 2270 J/g (at 100 ^0C and 1 bar) is released by water molecules in the vapor phase in order to form a hydrogen bond network in the liquid phase.

In general, liquid and vapor systems can be described by thermodynamic state variables. These can be cast into two classes: extensive and intensive. The extensive variables are the ones that are proportional to the number of particles in the system. Conversely, an intensive variable indicates a property of the system regardless of its size. An extensive variable can always be reduced to an intensive one dividing it by the number of particles in the system. For example, the volume and the entropy (V and S) can be divided by the number of particles (N) to obtain the specific volume and entropy ($v = V/N$ and $s = S/N$).

Standard equilibrium thermodynamic theory tells us that the knowledge of one thermodynamic potential as a function of the respective natural variables fully specifies the thermodynamics of the system. The most common thermodynamic potential is the internal energy, $U = TS - PV$, whose natural variables are S and V. If these are chosen as independent variables, $dU(S, V) = TdS - PdV$, heat (TdS) and work (PdV) are

[1]The presence of latent heat can be taken as a definition of a first order phase transition. It fingerprints an abrupt change in the intermolecular structure.

separated. Moreover the partial derivatives of U are physical significant quantities, i.e. pressure and temperature. Assuming that $U(S, V)$ is known, pressure and temperature are easily found:

$$T = (\frac{\partial U}{\partial S})_V \quad \text{and} \quad P = -(\frac{\partial U}{\partial V})_S \tag{1.1}$$

The first of the two previous equations can be used to eliminate S in favor of V and T. The second one can therefore be considered as the Equation of State (EoS) of the system, expressing P as a function of T and V. By manipulating the partial derivatives it is possible to find an expression for any thermodynamic quantity (specific heat, compressibility, sound velocity, etc...), moreover, the other thermodynamic potentials can be formally obtained from U by Legendre transformations.

The most appropriate thermodynamic potential to describe the liquid-vapor phase transition is the (specific) Gibbs free entalpy, $g(P, T) = vP - sT$, with natural variables P and T. The thermodynamic stable phase is the one that presents the minimum value of $g(P, T)$. If this value is the same in the two phases there is equilibrium (i.e. coexistence) between the phases. If $g(P, T)$ is plotted as a surface above the (P, T)-plane, no discontinuities are observed, in contrast to other thermodynamic potentials. For instance the Helmhotz free energy, $df(v, T) = dg(P, T) - d(Pv)$, dramatically decreases across the liquid-vapor phase boundary, because $v_v \gg v_l$. On the other hand, if the transition is not of first order, v will not change abruptly but continuously, and therefore f will not present such discontinuity. In other words, these discontinuities in the thermodynamic potentials are characteristic for first order transitions. Moreover, across this kind of transition, the derivatives of the thermodynamic potentials, including $g(P, T)$, are also discontinuous[2]. These discontinuities can be related to the latent heat, Q_L [10]:

$$Q_L = T(\overline{S}_v - \overline{S}_l) = T[(\frac{\partial g_v}{\partial T})_P - (\frac{\partial g_l}{\partial T})_P] \tag{1.2}$$

Where the suffixes "l" and "v" indicate respectively the liquid ($T < T_t$) and the vapor ($T > T_t$) side of the transition. The liquid vapor coexistence line ends at a certain point. This can be understood by looking at the physical meaning of the liquid-vapor equilibrium. In liquids the particles are strongly bound and confined in a well-defined volume, but some of them are fast enough to escape from the volume that spatially delimits the liquid phase: they evaporate. The particles that are now in the vapor phase are free to move. Some of them can fall again into the volume delimiting the liquid phase: they condensate. The whole system (liquid + vapor) is in equilibrium when the number of particles that evaporate and condensate are equal.

This equilibrium can be perturbed in different ways, for example by heating the liquid. In this case the particles in the liquid will gain energy and consequently are (in average) faster. More and more particles are then fast enough to escape from the liquid (i.e. to evaporate). In order to compensate this enhanced evaporation the number of

[2] According to Herenfest classification, a generic thermodynamic transition is called of the nth-order if the nth-derivative is the lowest one that presents a discontinuity across the transition [9].

particles that condensate must increase and, if this is not possible, all the liquid will turn into vapor after a certain time.

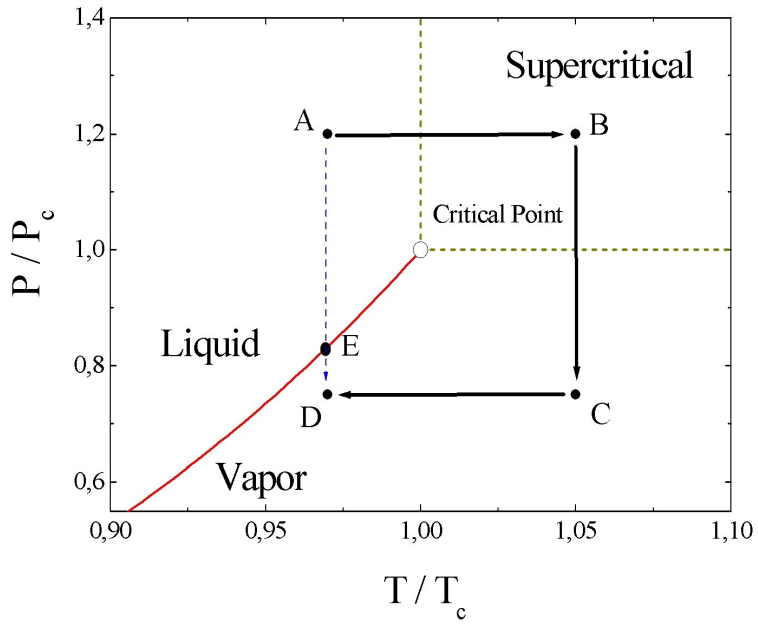

Figure 1.1: *Schematic picture of a liquid-vapor phase diagram expressed in reduced unities, where T/T_c and P/P_c. T_c and P_c denote the critical temperature and pressure, respectively. A liquid can be converted into vapor by decreasing the pressure at constant temperature,* $\mathbf{A} \rightarrow \mathbf{D}$. *This implies the absorption of latent heat (first order transition) when the system crosses the coexistence line* (**E**). *The same transition can be obtained, without involving latent heat, by following the path* $\mathbf{A} \rightarrow \mathbf{B} \rightarrow \mathbf{C} \rightarrow \mathbf{D}$

If the liquid is heated in a closed vessel, the evaporated particles increase the vapor density. This provides an increase of the vapor pressure and a higher condensation, enough to restore the equilibrium. Heating up a closed vessel actually means driving the system in successive equilibrium states along the coexistence line. Meanwhile the liquid density decreases because the liquid expands. The difference between the liquid and the vapor densities therefore decreases with increasing temperature and finally vanishes at T_c, the critical temperature. The associated values of density and pressure are called critical density and pressure, ρ_c and P_c. Above these values of temperature and pressure the liquid and the vapor cease to be different entities. The system becomes homogeneous and this new phase is called supercritical phase. Crossing the supercritical phase an arbitrary quantity of liquid can be converted into vapor (or vice-versa) without involving latent heat. First the liquid is heated up at $T > T_c$ at a pressure higher than P_c. Then, the pressure is reduced by an isothermal expansion. Finally, the system is cooled down to the desired temperature, below T_c. This path is illustrated in fig.1.1.

1.2 van der Waals equation of state

The first successful description of the liquid-vapor phase transition, including the critical point and the supercritical phase, was provided by J. D. van der Waals. He presented his theory in 1873, in his PhD thesis entitled *On the Continuity of the Gaseous and Liquid States*. The fundamental ideas of this theory represent a decisive step forward with respect to the ideal gas theory. The ingredients of the van der Waals equation of state are twofold:

- The particles can interact with each other through an attractive interaction potential.
- The particles have finite dimensions and the volume they occupy is not negligible with respect to the total volume of the system.

The first hypothesis is that the interaction potential of a system made out of N particles can be written as follows:

$$H = \sum_{i,j} h(|\vec{r}_i - \vec{r}_j|) = \sum_{i,j} h(r_{i,j}) \tag{1.3}$$

where $h(r_{i,j})$ is a two-body potential, depending on the relative distances, $r_{i,j}$, between the ith and the jth particles. A potential of this kind is sketched in figure 1.2. There is an attractive part with a negative energy minimum at distance r_m and a hard-core repulsion at distance d. This can therefore be interpreted as the diameter of a particle, considered as an hard sphere. Owing to the presence of interactions the spatial pair distribution function of particles, $g(r)$, is no longer uniform. This function in fact indicates the probability of finding two different particles separated by a distance r. As a consequence of intermolecular interactions, distances $\sim r_m$ are preferred. Furthermore the finite dimension of particles leads to a zero-probability for $d < r_m$ (see fig.1.2).

The average value of the energy, $\langle H \rangle$, in the canonical ensemble is given by:

$$\langle H \rangle = \frac{\int e^{\beta U} \sum h(r_{i,j}) dr_1 ... dr_N}{\int e^{\beta U} dr_1 ... dr_N} \tag{1.4}$$

where $\beta = (k_B T)^{-1}$, and k_B is the Boltzmann constant. After some straightforward algebra, neglecting the density dependence of both interaction potential and radial distribution function, and considering the thermodynamic limit (i.e. $N \to \infty$, $V \to \infty$ but $N/V = \rho$, where ρ is the density) the following equation is obtained [11]:

$$\langle H \rangle = \frac{a}{v} \tag{1.5}$$

where$a$ is a positive constant. Despite its simplicity this equation implies the existence of a volume-dependent contribution to the internal energy, U. Therefore we can derive equation 1.5 and obtain a pressure:

$$P_i = -\frac{\partial \langle H \rangle}{\partial V} = \frac{a}{v^2} \tag{1.6}$$

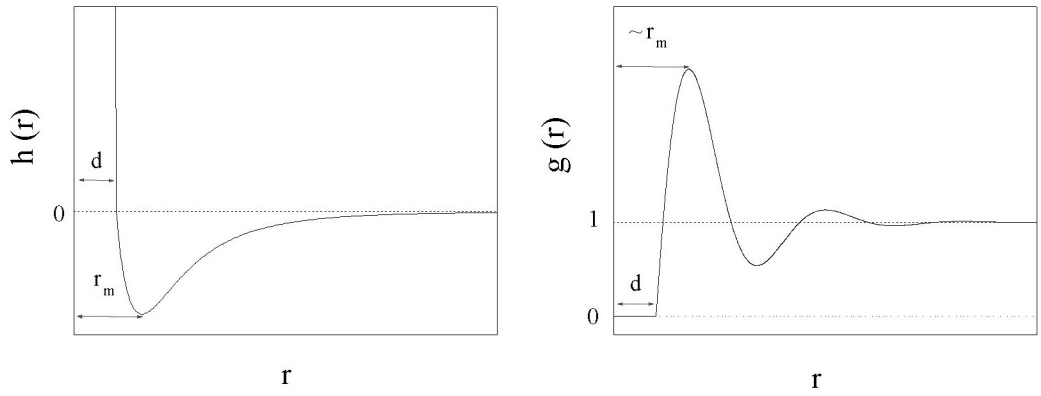

Figure 1.2: Left panel: *Sketch of the pairwise interaction potential,* $h(r)$. Right panel*: Sketch of the spatial pair distribution function.*

This pressure is called "internal pressure", as it accounts for the pressure exercised by the molecules on each other. It is also referred to as "intermolecular cohesion", because it is responsible for the spatially limited extension of liquids. The total pressure is then the sum of this "internal pressure" and the one exerted by the ideal gas, RT/v, where R is the gas constant. Moreover we have to replace the volume, v, with an "effective" volume, $v - b$, where b is the volume per molecule into which the molecules cannot be further compressed. With these two simple modifications the ideal gas equation of state, $P = RT/v$, becomes the van der Waals one:

$$P = \frac{RT}{v-b} - \frac{a}{v^2} \tag{1.7}$$

This equation reduces to the ideal gas equation of state, if v is large enough (rarefied gas[3]). In this case the term $\propto v^{-2}$ can be neglected with respect to the one $\propto v^{-1}$, as well as b with respect to v.

A graphical representation of eq.1.7 is given in fig.1.3, in which we plot the isotherms in the (P, v)-plane (Maxwell construction).

The green and yellow areas correspond to the liquid and vapor phase, respectively. Looking at the isotherm T_1 we notice that on applying pressure the volume can be brought up to v_A, where the condensation occurs: i.e. the volume can be varies from v_A to $v_B \ll v_A$ without changing temperature and pressure. The value of isothermal compressibility:

$$\chi_T = \frac{1}{v}(\frac{\partial v}{\partial P})_T \tag{1.8}$$

changes smoothly for $v > v_A$, but grows rapidly for $v < v_B$. Despite the fact that the points **a** and **b** have the same pressure and temperature, the respective values of

[3]For instance in real gases $b \sim 10^{-5}\ m^3/mole$ while $v \gg 10^{-3}\ m^3/mole$.

the compressibility (i.e. the inverse of the slope of the blue lines, tangent in **a** and **b** in fig.1.3) are very different. This fingerprints the transition from the vapor to the liquid phase. The area delimited by the concave blue dotted curve therefore represents the liquid-vapor coexistence. In the liquid phase the "internal pressure", $\propto v^{-2}$, is much bigger than the one exerted by the vapor (ideal gas). This provides the cohesion that keeps the liquid system spatially limited, even without an external constraint. In a closed thermodynamic loop such as **a** → **a‘** → **d** → **b‘** → **b** → **d** → **a**, the relation $\oint dg(P,T) = 0$ must hold. Along an isotherm this relation reduces to $\oint (\frac{\partial g(P,T)}{\partial P})_T dP = \oint v dP = 0$. Thus, the hatched areas **a-a‘-d** and **d-b‘-b** are equal (Maxwell rule). From this condition the concave blue dotted curve in fig.1.3, which corresponds to condensation (or boiling), can be obtained. Moreover, the area $P \cdot (v_a - v_b)$ is equal to the specific heat of the transition.

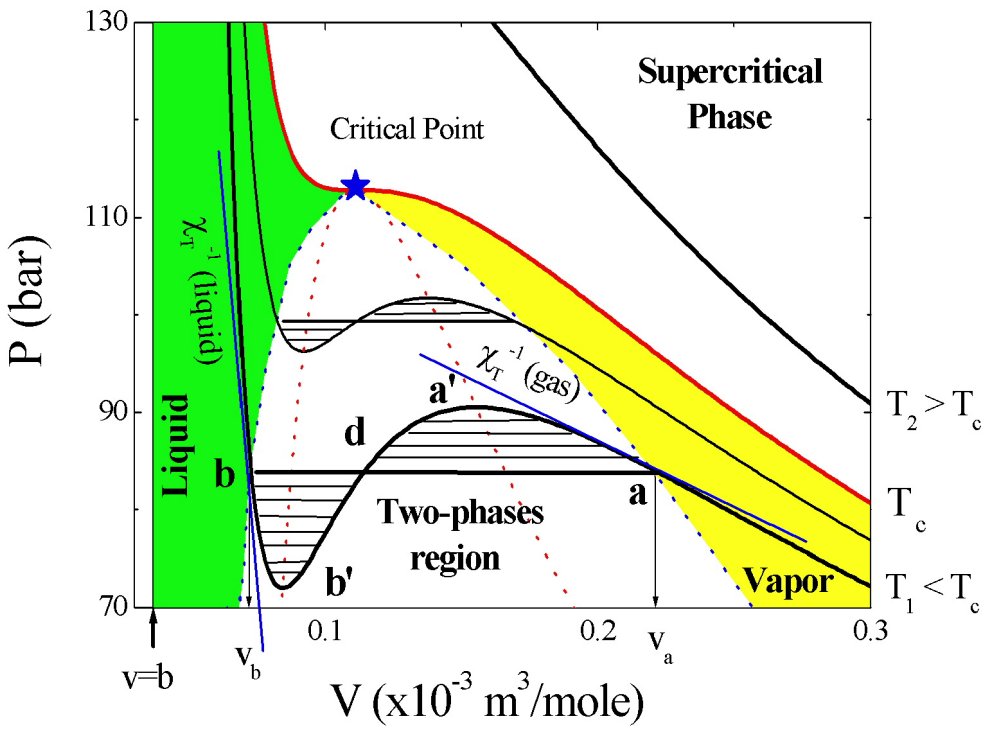

Figure 1.3: *van der Waals equation of state for ammonia:* $b = 0.037 * 10^{-3}\ m^3/mole$ *and* $a = 4.17 * 10^{-6}\ bar * m^6/mole^2$. See text for further details.

Even if the main features of the two phases and the liquid-vapor transition are reproduced, the real isotherms are different with respect to the ones calculated from eq.1.7. In particular, in the two-phases region the S-shape feature is replaced by straight lines (thick horizontal lines in fig.1.3). The reason for this discrepancy is simple: the van der Waals theory does not take into account the presence of two different phases or any mechanism for the liquid-vapor transition. The relevant result of this theory is

in fact that the liquid-vapor transition arises as a natural consequence of interactions among finite size particles. The liquid state is then a direct consequence of a non negligible interaction between particles. This is an universal statement, valid for any kind of material with (attractive) interactions.

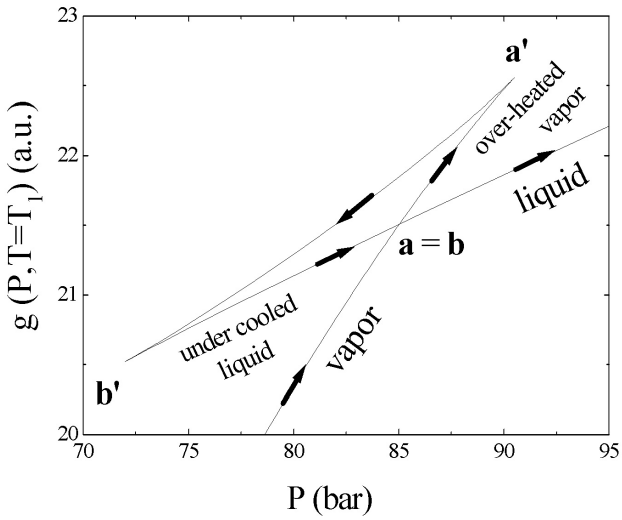

Figure 1.4: *Gibbs free enthalpy for ammonia at the temperature T_1 of fig.1.3, the* ***a-a‘*** *and* ***b-b‘*** *states are metastable, since they have values of $g(P, T = T_1)$ higher than the respective stable states, the liquid and the gas ones.*

The Gibbs free enthalpy[4], $g(P, T)$, for the isotherm T_1 (referring to fig.1.3) is shown in fig.1.4. From this figure it can be seen that the S-shape feature (from **a** to **b** in fig.1.3) predicted by the van der Waals EoS corresponds to two metastable phases: the supercooled liquid (from **b** to **b‘**) and the overheated vapor (from **a** to **a‘**). These are two out-of-equilibrium phases, that can be experimentally observed in very pure materials. The difference between the left and right derivatives of $g(P_a = P_b, T_1)$ corresponds to the latent heat. The section of the curve between **a‘** and **b‘**, instead, does not have a physical meaning, since it implies increasing volumes with increasing pressures (see fig.1.3).

The two points, **a‘** and **b‘**, are singular points at which the compressibility, defined in eq.1.8, diverges. The coordinates of these points (concave red dotted curve in fig.1.3) can been obtained by putting the first derivative of van der Waals EoS equal to zero:

$$(\frac{\partial P}{\partial v})_T = 0 = -\frac{RT}{(v-b)^2} + \frac{2a}{v^3} \tag{1.9}$$

The other remarkable result of this equation is the prediction of a unique special point, the critical point. In fig.1.3 it can be seen that the volume difference, $v_A - v_B$, between the liquid and the vapor phase decreases with increasing temperature, and

[4]The analytical form of this thermodynamic potential is $g = -RTln(1-b/v)+RTb/(v-b)-2a/v^2$

consequently the latent heat. At the same time the two singular points come closer, and finally coincide at the critical point. At temperatures higher than T_c, the isotherms never enter the two-phases region. This means that there is no liquid-vapor coexistence and no latent heat has to be given in order to further decrease the volume of the system. This is the so called supercritical phase. Here the derivative of the Gibbs potential, as well as the isothermal compressibility, does not present discontinuities for any P and T. The system is therefore always homogeneous and the difference between liquid and vapor ceases to be meaningful. Once again this result is a universal feature, valid for all existent material. The presence of the critical point and the supercritical phase is a direct consequence of the existence of the liquid and the vapor phase.

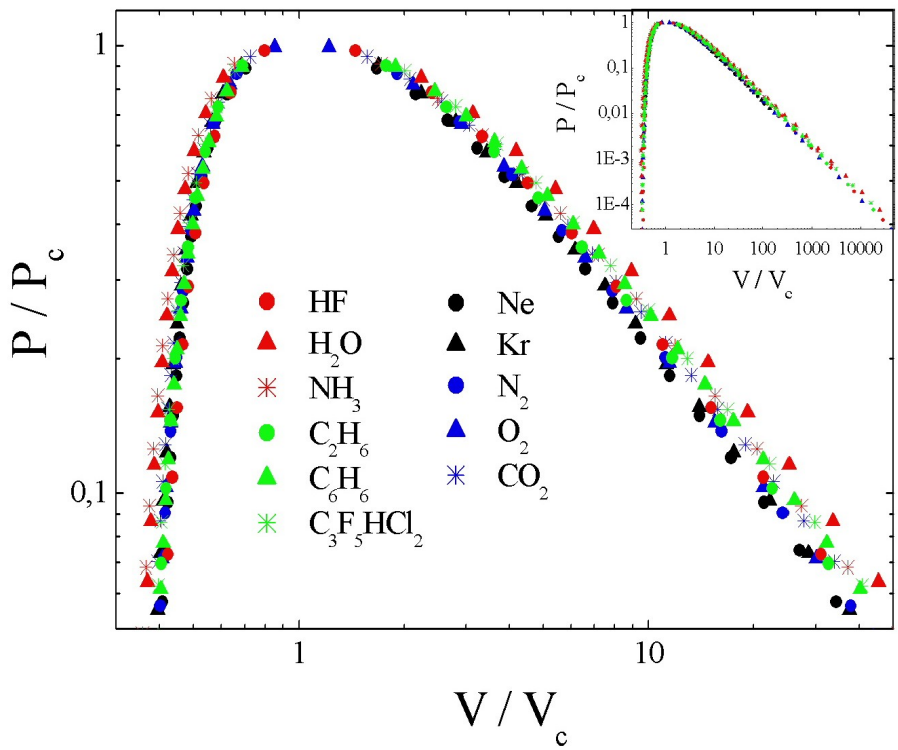

Figure 1.5: *Graphical representation of the law of corresponding states. The inset reports the same curves on a larger scale.*

Excluding the "theoretical" singular points **a‘** and **b‘**, the critical point is the only one that presents a singularity. Moreover, it is a horizontal tangent flex, that means that not only the first derivative is equal to zero, but also the second one:

$$(\frac{\partial^2 P}{\partial v^2})_T = 0 = \frac{2RT}{(v-b)^3} - \frac{6a}{v^4} \tag{1.10}$$

From eqs.1.9, 1.10 and 1.7, the thermodynamic coordinates of the critical point can be derived:

$$v_c = 3b \quad P_c = \frac{a}{27b^2} \quad T_c = \frac{8a}{27Rb} \tag{1.11}$$

Writing the van der Waals equation of state in reduced units ($v^* = v/v_c$, $P^* = P/P_c$ and $T^* = T/T_c$), the system-dependent quantity, a and b, can be eliminated:

$$(P^* - \frac{3}{v^{*2}})(v^* - \frac{1}{3}) = \frac{8}{3}T^* \tag{1.12}$$

where $8/3 = RT_c/P_cv_c$ is the critical coefficient, that is independent of the specific material. Equation 1.12 is called the law of corresponding states. An example of this universal law is given in fig.1.5, where the boundary of the two phases region is reported in reduced units for a selection of different materials.

The qualitative agreement of this theory with the real behavior of liquids and vapors is remarkable in many respects:

- The occurrence of the liquid-vapor phase transition can be quantitatively predicted.
- The existence of two unfavorable thermodynamic states (metastability).
- All materials must have a critical point and a supercritical phase.
- The liquid-vapor transition can always be considered as a continuous transition instead of a first-order one.
- In the supercritical phase the liquid-vapor transition as well as the concept of liquid and vapor as two different thermodynamic states no longer exist.
- If the equation of state is expressed in reduced units (law of corresponding states), the liquid-vapor phase transition is not only phenomenologically similar in all materials, but it is strictly the same.

Nevertheless the quantitative discrepancies are quite large. The measured critical coefficient is usually $20 \div 30$ % different from the predicted value (for instance in water the measured one is 2.29 instead of 2.67=8/3). These discrepancies are mostly due to the crude approximations made in order to describe the interactions and the finite size of the molecules. Although the interpretation of intermolecular attractive forces in terms of only one parameter, a, is quite good and not very different from the more modern mean field approach, the repulsive hard-spheres potential can be treated in a much better way.

Résumé du chapitre 2

Le chapitre 2 est consacré au développement du formalisme théorique capable de décrire les réponses statiques et dynamiques d'un fluide. Le formalisme fondamental des fonctions de corrélation de temps, ainsi que leur relation avec la quantité expérimentalement observable, c'est-à-dire le facteur de structure dynamique, $S(Q,\omega)$, est présenté. Une expression explicite pour le facteur de structure dynamique est dérivée dans le cadre de l'hydrodynamique classique: c'est-à-dire quand le moment transféré (Q) et la fréquence (ω) sont beaucoup plus petits que l'inverse des distances intermoléculaires caractéristiques (λ_0) et des temps d'intéraction (τ_0). Dans la deuxième partie du chapitre, une expression plus générale pour $S(Q,\omega)$, qui est valide aussi quand $Q \sim 1/\lambda_0$ et $\omega \sim 1/\tau_0$, est introduite. Par le concept de processus de relaxation, cette expression peut tenir compte de la dynamique microscopique du système.

Chapter 2

Fluctuations and Hydrodynamics

The basic concepts of hydrodynamics, as well as the theoretical formalism used to describe its rich phenomenology, are discussed in this chapter. It is divided as follows: in section 2.1 basic insights on the relevant quantities used to describe the response of a fluid to an applied perturbation are given. In section 2.2 the hydrodynamic limit is discussed, while in sections 2.3-2.5 the memory function formalism and its application to hydrodynamics are presented. Finally, in section 2.6, the single particle regime is briefly discussed.

2.1 Introduction

When a perturbation acts on a fluid, the disturbance is damped by dissipation phenomena: diffusions, viscous flows and thermal exchanges. Even without an external perturbation, spontaneous microscopic fluctuations are present in the fluid. These naturally occur in a broad band of wavelengths and frequencies. Spontaneous fluctuations, according to the dissipation-fluctuation theorem [12], are dissipated in the same way as the applied perturbation. For this reason, studying the response of the system as a function of frequency and momentum of the induced perturbation, gives basic information on the structure and the dynamics of the unperturbed system at different length- and timescales. Formally, the response of a fluid to an applied perturbation is known only in two limiting cases:

- At low momentum and frequency: the hydrodynamic limit. Here information on the macroscopic properties of the system are recovered, while microscopic information can be obtained only indirectly.
- At very high momentum: the single particle limit. Here the system behaves as a non-interactive ensemble of particles; therefore information on collective dynamics cannot be retrieved.

At wavelengths comparable to intermolecular distances (mesoscopic region) both local structures and dynamics become important. This is the most interesting region because information on the local arrangement of molecules and the interactions among

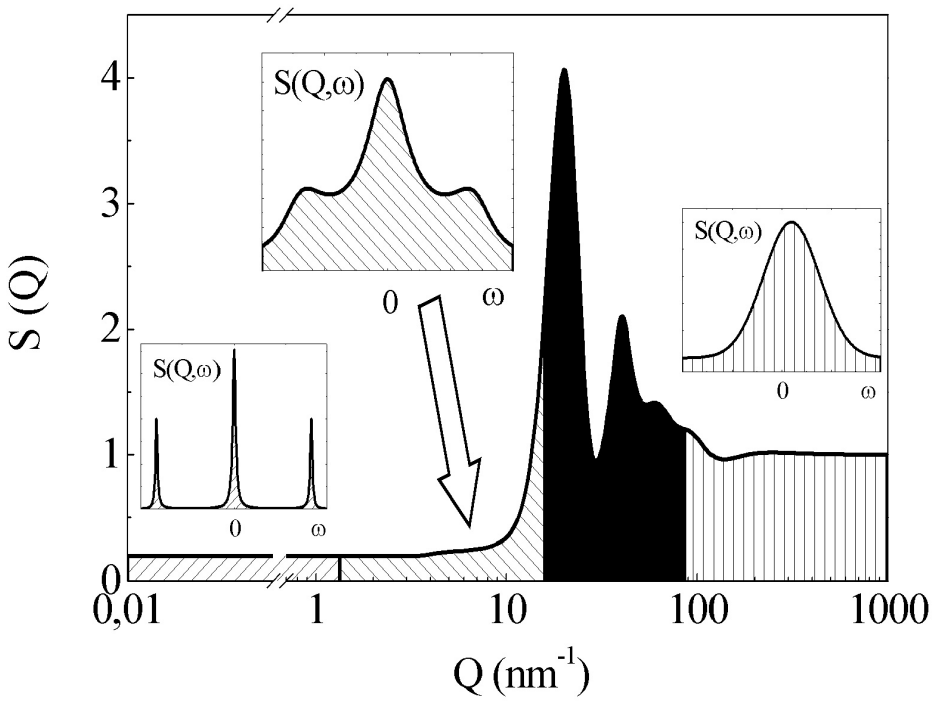

Figure 2.1: *Static structure factor, $S(Q)$, of a generic fluid. The insets show the shape of the dynamic structure factor, $S(Q,\omega)$, in the hydrodynamic (left panel), the mesoscopic (center panel) and the single particle regime (right panel).*

them can be obtained. Unfortunately neither the hydrodynamic nor the single particle limit can describe the response of the system in this range. To date, a formally exact description of the fluid dynamics in the mesoscopic region does not exist. Nevertheless there are some approaches, as the one based on the memory function, able to sufficiently well describe the observed phenomenology.

The three ranges described above (hydrodynamic, mesoscopic and single-particle) are sketched in fig.2.1, in which the static structure factor, $S(Q)$, of a generic liquid system is shown. The insets of this figure schematically depict the aspect of the corresponding dynamic structure factors, $S(Q,\omega)$.

2.2 Fluid dynamics: time correlation functions

The main role in the description of fluid dynamics is played by the time correlation functions. A time correlation function is defined as the thermodynamic average of the product of two dynamical, i.e. time-dependent, variables. Each one represents an instantaneous deviation (fluctuation) of the physical quantity, $A(\vec{r},t)$, with respect to its equilibrium value, $\langle A \rangle$:

$$\delta A(\vec{r},t) = A(\vec{r},t) - \langle A \rangle \tag{2.1}$$

The average, $\langle ... \rangle$, is carried out over the phase coordinates of all molecules in the fluid with an equilibrium ensemble as weighting function. Considering the spatial and temporal invariance of the liquid[1], the time correlation function, $C_{A,B}(\vec{r}_1, \vec{r}_2, t_1, t_2)$, of the dynamical variables $A(\vec{r}_1, t_1)$ and $B(\vec{r}_2, t_2)$ is therefore:

$$C_{A,B}(\vec{r}_1, \vec{r}_2, t_1, t_2) = V\langle \delta A(\vec{r}_1, t_1)\delta B(\vec{r}_2, t_2)\rangle = V\langle \delta A(\vec{r}, t)\delta B(0,0)\rangle = C_{A,B}(\vec{r}, t) \tag{2.2}$$

where $\vec{r} = \vec{r}_2 - \vec{r}_1$, $t = t_2 - t_1$ and V is the volume. For $t = 0$ $C_{A,B}(\vec{r}, t)$ assumes its maximum value, while for $t \to \infty$ it tends to zero [10], indicating the loss of any correlation between the two variables when they are evaluated at very different times.

Among all possible fluctuating variables describing the dynamics of fluids, a crucial role is played by density fluctuations since they are directly probed by a large number of spectroscopic techniques. The density function can be expressed as follows:

$$n(\vec{r}, t) = \frac{1}{\sqrt{N}} \sum_{i=1}^{N} \delta(\vec{r} - \vec{R}_i(t)) \tag{2.3}$$

where N is the number of particles and $\vec{R}_i(t)$ is their position; moreover $\langle n(r,t)\rangle = \sqrt{N}/V$. The density-density correlation function can then be written as:

$$G(\vec{r}, t) = V\langle \delta n(\vec{r}_1, t_1)\delta n(\vec{r}_2, t_2)\rangle = \frac{V}{N}\langle \sum_{i,j=1}^{N} \delta(\vec{r}_1 - \vec{R}_i(t_1))\delta(\vec{r}_2 - \vec{R}_j(t_2))\rangle + n \tag{2.4}$$

where $n = N/V$. $G(\vec{r}, t)$ is also called the Van Hove pair correlation function [13]. In inelastic spectroscopic measurements the experimental observable is the time and space fourier transform of $G(\vec{r}, t)$, which is usually called the dynamical structure factor, $S(\vec{Q}, \omega)$:

$$S(\vec{Q}, \omega) = \int_V d\vec{r} \int_{-\infty}^{+\infty} G(\vec{r}, t) e^{i(\vec{Q}\cdot\vec{r} - \omega t)} dt \tag{2.5}$$

Where $\vec{Q}$ is the momentum and ω is the angular frequency. They are the Fourier conjugates of the position $\vec{r}$ and the time t, respectively. It is convenient to introduce the intermediate scattering function, $F(\vec{Q}, t)$, which is the spatial Fourier transform of $G(\vec{r}, t)$ or, equivalently, the inverse time Fourier transform of the $S(\vec{Q}, \omega)$:

$$F(\vec{Q}, t) = \langle n^*(\vec{Q}, 0) n(\vec{Q}, t)\rangle + n(2\pi)^3 \delta(\vec{Q}) = \int_{-\infty}^{+\infty} e^{i\omega t} S(\vec{Q}, \omega) d\omega \tag{2.6}$$

where:

[1] The temporal invariance holds as far as the thermodynamic average is defined in a time independent ensemble.

$$n(\vec{Q},t) = \frac{1}{\sqrt{N}} \sum_{i=1}^{N} e^{i\vec{Q}\cdot\vec{R}_i(t)} \tag{2.7}$$

Another important time correlation function is the current-current pair correlation function:

$$J_{\alpha\beta}(\vec{r},t) = V\langle j_\alpha(\vec{r}_1,t_1) j_\beta(\vec{r}_2,t_2)\rangle \tag{2.8}$$

where α and β are the cartesian indexes and $\vec{j}(\vec{r},t)$ is the current density:

$$\vec{j}(\vec{r},t) = \frac{1}{\sqrt{N}} \sum_{i=1}^{N} \vec{v}_i(t)\delta(\vec{r} - R_i(t)) \tag{2.9}$$

where $\vec{v}_i(t)$ is the velocity of the ith particle. For spherical symmetrical systems, such as fluids, only the purely longitudinal and transverse components, $J_l(\vec{r},t)$ and $J_t(\vec{r},t)$, are meaningful [5, 7, 8]. Moreover, only the modulus of the momentum, $|\vec{Q}| = Q$, needs to be considered.

Employing the continuity equation and straightforward algebra the following relation can be derived [7]:

$$J_l(Q,\omega) = \frac{\omega^2}{Q^2} S(Q,\omega) \tag{2.10}$$

where $J_l(Q,\omega)$ is the time and space Fourier transform of $J_l(\vec{r},t)$.

In order to interpret the experimental observations, a general expression for $S(Q,\omega)$ or, alternatively, for $J_l(Q,\omega)$ is needed. In both cases an N-body dynamical problem has to be solved. Except the cases of an ideal Bravais lattice or an ideal gas, the formal solution of this N-body dynamical problem is in practice impossible. Nevertheless, in the case of dense and interactive fluids, it is possible to obtain some excellent approximations for $S(Q,\omega)$, as will be shown in the following.

We conclude this section with a remark. In quantum mechanics the dynamical variables evaluated at different times do not necessarily commute. The order in which they appear in the thermal average is therefore important. In this case the spectrum of a general correlation function at thermodynamic equilibrium, $C_{A,B}(r,t)$, must satisfy the following relation, usually called the detailed balance [14]:

$$C_{A,B}(Q,\omega) = e^{\hbar\omega/k_B T} C_{A,B}(-Q,-\omega) \tag{2.11}$$

where k_B is the Boltzmann constant and T is the temperature. This means that the spectrum $C_{A,B}(Q,\omega)$ is not symmetric in ω. The energy gain side (Stokes) is higher than the energy loss one (Anti-Stokes). For isotropic systems it the Q-dependence of $C_{A,B}(Q,\omega)$ is expected to be $\propto Q^2$, therefore the change $Q \to -Q$ is irrelevant. For this reason the spectra are symmetrical in the classical limit, i.e. $\hbar \to 0$.

2.2.1 Static correlation functions

Before explicitly calculating $S(Q,\omega)$ in the various approximations, it is convenient to learn more about the general properties of time correlation functions.

If we evaluate A and B in eq.2.2 at the same time ($t_1 = t_2$) the following static correlation function is obtained[2]:

$$C_{A,B}(r,0) = V\langle \delta A(r_1,0)\delta B(r_2,0)\rangle \tag{2.12}$$

This correlation function does not depend on time, but contains precious information on the equilibrium properties of the system. In particular, the static correlation function associated with density fluctuations is of the greatest importance. Using the definitions given in eqs.2.6 and 2.7, and defining the equilibrium pair distribution function, $g(r)$, as follows:

$$g(r) = \sum_{i\neq j}\langle \delta(r-R_i)\delta(R_j)\rangle \tag{2.13}$$

$F(Q,0)$ can be derived:

$$F(Q,0) = 1 + n\int_V d^3r e^{iQ\cdot r}[g(r)-1] \equiv S(Q) \tag{2.14}$$

The quantity $S(Q)$ is called static structure factor. It can be directly measured in an X-ray or neutron diffraction experiment and it contains all the relevant information on the equilibrium structure of the system. As will be shown in the following sections this quantity is extremely useful in order to analyze and interpret our data. Using the definition of $F(Q,t)$ and $S(Q)$ given in eqs.2.6 and 2.14, the following relation is readily found:

$$S(Q) = F(Q,0) = [\int_{-\infty}^{+\infty} e^{i\omega t}S(Q,\omega)d\omega]_{t=0} = \int_{-\infty}^{+\infty} S(Q,\omega)d\omega \tag{2.15}$$

An important property of $S(Q)$ is its limiting values for $Q \to 0$, and for $Q \to \infty$. The latter is equal to unity, indicating the vanishing of correlation at very short distances, while the former limit is the important compressibility relation [7, 8]:

$$S(Q\to 0) = 1 + n\int_V d^3r[g(r)-1] = \frac{n\chi_T}{k_BT} \tag{2.16}$$

where χ_T is the isothermal compressibility.

Moreover, the static structure factor of a fluid shows a clear maximum, called the first sharp diffraction peak, at Q-values, Q_m, in the range $15 \div 25\ nm^{-1}$. It is related to the average intermolecular distances, r_m, represented by the maximum of the pair distribution function, $g(r)$ ($Q_m \sim 2\pi/r_m$). For completeness, we recall that other important static correlation functions are the ones that define the high-frequency shear and bulk moduli and the viscous flow (see chapter 2.3 of [7]).

[2]Exploiting the temporal invariance and stationarity of the time correlation function, we can consider $t_1 = t_2 = 0$

2.2.2 Frequency sum rules

In the previous chapter it was shown that $S(Q) = \int_{-\infty}^{+\infty} S(Q,\omega)d\omega$. This relation is an example of frequency sum rules. These rules characterise the short-time behavior of $F(Q,t)$. In fact, starting from eq.2.6, we can write a Taylor series expansion for $F(Q,t)$:

$$F(Q,t) = \omega^0(Q) + i\omega^1(Q)t - \omega^2(Q)\frac{t^2}{2!} - i\omega^3(Q)\frac{t^3}{3!} + ... \tag{2.17}$$

where:

$$\omega^n(Q) = (i)^n[\frac{\partial^n}{\partial t^n}F(Q,t)]_{t=0} = \int_{-\infty}^{+\infty} \omega^n S(Q,\omega)d\omega \tag{2.18}$$

are called n^{th} frequency sum rules or n^{th} spectral moment [7, 8]. From the knowledge of the coefficients, $\omega^n(Q)$, the time dependence of $F(Q,t)$ can be obtained, and through a Fourier transform, the $S(Q,\omega)$. This procedure seems appealing, but, unfortunately, the expressions of the high order spectral momenta are very complicated, thus unusable in practice.

In table 2.1 the classical results concerning the lower frequency sum rules, for the relevant correlation functions usually employed in the description of fluid dynamics, are reported [3]. The coefficients Ω_0 (Einstein frequency), Γ_l and Γ_t can be calculated from the pairwise interaction potential, $h(r)$, and the pair distribution function, $g(r)$, through the relations: $\Omega_0 = \frac{Nm}{V}\int_V d\vec{r}g(r)\frac{\partial^2 h(r)}{\partial x_l^2}$, $\Gamma_l = \frac{Nm}{V}\int_V d\vec{r}g(r)(1-cos(Qr))\frac{\partial^2 h(r)}{\partial x_l^2}$ and $\Gamma_t = \frac{Nm}{V}\int_V d\vec{r}g(r)(1-cos(Qr))\frac{\partial^2 h(r)}{\partial x_t^2}$, where x_l and x_t are, respectively, the components of $\vec{r}$ parallel and perpendicular to $\vec{Q}$. The 4th spectral momenta of current correlation functions have a very complicated analytical form [7], while the calculation of higher order momenta can be found in [15, 16, 17, 18].

Dynamical variable	0th spectral momentum	2nd spectral momentum	4th spectral momentum
$G(r,t)$	$S(Q)$	$\frac{k_BTQ^2}{m}$	$3(\frac{k_BTQ^2}{m})^2 + \frac{k_BTQ^2}{m}\Gamma_l$
$G_s(r,t)$	1	$\frac{k_BTQ^2}{m}$	$\frac{k_BTQ^2}{m}[\frac{k_BTQ^2}{m} + \Omega_0^2]$
$J_l(r,t)$	$\frac{k_BT}{m}$	$3(\frac{k_BTQ}{m})^2 + \frac{k_BT}{m}\Gamma_l$	–
$J_t(r,t)$	$\frac{k_BT}{m}$	$(\frac{k_BTQ}{m})^2 + \frac{k_BT}{m}\Gamma_t$	–
$J_s(r,t)$	1	Ω_0^2	–

Table 2.1: *Lower order sum rules in the classical limit.*

[3] All the odd moments vanish since the power spectra of classical dynamical variables are even functions of ω. This is no longer true in quantum mechanics due to the detailed balance factor.

2.3 Classical approach: hydrodynamic limit

Within the framework of classical hydrodynamics an exact expression for $S(Q,\omega)$ in the long-time and long-wavelength limit, i.e. in the low frequency and momentum region, can be obtained. The adjective "long" in the previous sentence must be read as: wavelengths "much longer than" the intermolecular distance (r_0) and times "much longer than" the typical relaxation time (τ). Classical hydrodynamics then probe dynamics involving a large number of particles, in a characteristic "time-window" much longer than any microscopic time-scale. The corresponding $S(Q,\omega)$ is characterized by long-living collective modes, which are related to purely macroscopic quantities. These can provide only time-averaged information and any direct insights into microscopic structures and dynamics are lost.

This classical description is based on the study of conserved variables, which are ruled by mass, momentum and energy conservation laws. These express the balance between the rate of change of the density of a certain variable, inside a considered volume, and the flux of the corresponding current through the surface delimiting the volume itself.

2.3.1 Mass conservation

The conservation of matter requires the fulfilment of the so-called continuity equation:

$$\frac{\partial}{\partial t}\rho(\vec{r},t) + \nabla \cdot \vec{J}(\vec{r},t) = 0 \tag{2.19}$$

where $\vec{J}(\vec{r},t) = \rho(\vec{r},t)\vec{v}(\vec{r},t)$ is the mass current field given by the product between the mass density, $\rho(\vec{r},t)$, and the particles velocity field, $\vec{v}(\vec{r},t)$.

2.3.2 Momentum conservation

Cauchy's law of motion for isotropic media can be written as [7]:

$$\rho(\vec{r},t)\frac{dv_i(\vec{r},t)}{dt} = \frac{\partial}{\partial t}\sum_j[-P(\vec{r},t)\delta_{i,j} + \pi_{i,j}(\vec{r},t)] \tag{2.20}$$

where $P(\vec{r},t)$ is the hydrostatic pressure, the subscripts i and j denote the cartesian indexes, and $\delta_{i,j}$ is the Kronecker delta function. Finally $\pi_{i,j}(\vec{r},t)$ is the stress tensor assumed to be linear in the two viscosity coefficients, namely the shear (η_s) and the dilatational (η_d) one:

$$\pi_{i,j}(\vec{r},t) = (2\eta_s + \eta_d\delta_{i,j})\Delta_{i,j}(\vec{r},t) \tag{2.21}$$

Here $\Delta_{i,j}(\vec{r},t)$ is the rate of deformation tensor that, in a Newtonian fluid, has the following form:

$$\Delta_{i,j} = (\frac{\partial v_i(\vec{r},t)}{\partial r_j} + \frac{\partial v_j(\vec{r},t)}{\partial r_i}) \tag{2.22}$$

If η_s and η_d are considered to be constant eqs. 2.20-2.22 can be used to obtain the Navier-Stokes equation for a Newtonian fluid:

$$\rho(\vec{r},t)\frac{\partial}{\partial t}\vec{J}(\vec{r},t)+(\vec{J}(\vec{r},t)\cdot\nabla)\vec{J}(\vec{r},t)+\nabla P(\vec{r},t)-\eta_s\nabla^2\vec{J}(\vec{r},t)-(\eta_s+\eta_d)\nabla(\nabla\cdot\vec{J}(\vec{r},t))=0 \tag{2.23}$$

2.3.3 Energy conservation

If u denotes the internal energy per unit mass, energy conservation implies that the rate of change of u must be compensated by both thermal exchange and mechanical dissipations:

$$\rho(\vec{r},t)\frac{du}{dt}=\sum_{j,k}-P(\vec{r},t)\frac{\partial v_j(\vec{r},t)}{\partial r_j}+\Phi_{j,k}(\vec{r},t)-\frac{\partial J^u_j(\vec{r},t)}{\partial r_j} \tag{2.24}$$

where $J^u(\vec{r},t)$ is the heat flux and $\Phi_{j,k}(\vec{r},t)=\pi_{j,k}(\vec{r},t)\Delta_{j,k}(\vec{r},t)$ are the viscous dissipations. With the general assumption that the thermodynamic state of the system can be fully described by three state variables, related by the equation of state (EoS), the energy conservation equation reads [5]:

$$\begin{aligned}C_V[\rho(\vec{r},t)\frac{\partial T(\vec{r},t)}{\partial t}+\vec{J}(\vec{r},t)\cdot\nabla T(\vec{r},t)]&=k\nabla^2T(\vec{r},t)\\ -\frac{T(\vec{r},t)}{\rho}(\frac{\partial P(\vec{r},t)}{\partial T})_{\rho(\vec{r},t)}\nabla\cdot\vec{J}(\vec{r},t)&+\Phi_\eta(\vec{r},t)\end{aligned} \tag{2.25}$$

where $T(\vec{r},t)$ is the temperature, C_V is the specific heat at constant volume and k is the thermal conduction. All the ingredients needed to solve the classical hydrodynamic equations are contained in eqs.2.19, 2.23 and 2.25. These equations are expressed in terms of four unknown quantities: $\rho(\vec{r},t)$, $T(\vec{r},t)$, $P(\vec{r},t)$ and $\vec{J}(\vec{r},t)$. Furthermore the EoS can be used to eliminate one of the three thermodynamic variables. The problem is then in principle solved, since we are dealing with a closed set of three equations in three variables (5 scalar equations in 5 scalar variables).

In summary, in order to solve the hydrodynamic equations, the following assumptions have been made:

- The fluid is a continuous and homogeneous medium. It is isotropic, viscous and thermally conducting.
- The local thermodynamic equilibrium is assumed to be fully determined by three state variables, related to each other through the EoS.
- The fluid obeys the Newtonian equation of motion.
- Thermal and viscous dissipations are assumed to be described by linear laws, and the transport coefficients (i.e. thermal conduction and viscosity) are assumed to be constant parameters.

Within these assumptions the hydrodynamic equations are formally correct, as well as the analytical form of $S(Q,\omega)$ that will be derived in the next section.

2.3.4 Linearized hydrodynamics and Rayleigh-Brillouin spectrum

As already pointed out the goal is to calculate $S(Q,\omega)$, the quantity describing the dynamics of the system. The first step is to rewrite eqs.2.19, 2.20 and 2.25 in terms of fluctuating quantities:

$$\delta X(\vec{r},t) = X(\vec{r},t) - \langle X \rangle \tag{2.26}$$

where $X(\vec{r},t)$ is the local value of any physical quantity and $\langle X \rangle$ its average value, calculated over the whole system. $\delta X(\vec{r},t)$ is thus a quantity that fluctuates around zero, both in time and space.

As "local value" of the variable X one considers the value that it assumes in a small volume, ξ. Within this volume, characterized by the spatial coordinate $\vec{r}$, X is considered not to change significantly. Moreover ξ cannot be arbitrarily small, because it must contain enough particles in order to carry out a meaningful ensemble average, otherwise the value of a (classical) physical quantity is not well defined. Therefore $X(\vec{r},t)$ is not a microscopic quantity, but a "local" macroscopic value.

Using eq. 2.26 one can rewrite eqs.2.19, 2.20 and 2.25 in terms of the respective fluctuations[4]. For small enough fluctuations, the terms of orders higher than one in $\delta X(\vec{r},t)$ can be neglected. The three hydrodynamic equations can therefore be linearized and, using some general thermodynamic relations, the following solutions can be obtained in the Fourier-Laplace space:

$$s\delta\rho(Q,s) + i\vec{Q}\cdot\vec{J}(Q,s) = \delta\rho(Q,0) \tag{2.27}$$

$$i\frac{c_s^2}{\gamma}\vec{Q}\delta\rho(Q,s) + (s+\nu_L Q^2)\vec{J}(Q,s) + i\alpha\langle\rho\rangle\frac{c_s^2}{\gamma}\delta T(Q,s) = \vec{J}(Q,0) \tag{2.28}$$

$$i\frac{\gamma-1}{\alpha}\vec{Q}\cdot\vec{J}(Q,s) + (s+\gamma D_T Q^2)\langle\rho\rangle\delta T(Q,s) = \langle\rho\rangle\delta T(Q,0) \tag{2.29}$$

Where $D_T = k(\rho C_P)^{-1}$ is the thermal diffusivity, $c_s = (\partial P/\partial\rho)_s$ is the adiabatic sound velocity[5], $\alpha = \rho(\partial V/\partial T)_P$ is the thermal expansion, $\gamma = C_P/C_V$ is the specific heat ratio and ν_L is the longitudinal kinematic viscosity, whose explicit expression will be given later. This set of 3 equations (eqs.2.27, 2.28 and 2.29) in 3 variables can be cast into a 3×3 matrix and solved with respect to $\delta\rho(Q,s)$:

[4]Since the whole system does not flow, the mean value of the current, $\langle J \rangle$, is equal to zero; therefore $\delta J(\vec{r},t) = J(\vec{r},t)$.

[5]The index "s" in the partial derivative stands for constant entropy

$$\delta\rho(Q,s) = \frac{det\begin{pmatrix} \delta\rho(Q,0) & i\vec{Q} & 0 \\ \vec{J}(Q,0) & (s+\nu_L Q^2) & i\alpha\langle\rho\rangle\frac{c_s^2}{\gamma} \\ \langle\rho\rangle\delta T(Q,0) & i\frac{\gamma-1}{\alpha}\vec{Q} & (s+\gamma D_T Q^2)\langle\rho\rangle \end{pmatrix}}{det\begin{pmatrix} s & i\vec{Q} & 0 \\ i\frac{c_s^2}{\gamma}\vec{Q} & (s+\nu_L Q^2) & i\alpha\langle\rho\rangle\frac{c_s^2}{\gamma} \\ 0 & i\frac{\gamma-1}{\alpha}\vec{Q} & (s+\gamma D_T Q^2)\langle\rho\rangle \end{pmatrix}} \tag{2.30}$$

The denominator of equation 2.30 (the coefficients determinant) can be expressed in terms of a dispersion relation: $\prod_{i=1}^{5}(s-s_i)$, where s_i are the matrix eigenvalues. These range from 1 to 5 because they are scalar numbers, while eq.2.28 is vectorial. Moreover, they are independent of the base, i.e. the eigenvalues are independent of the chosen set of variables.

The EoS can thus be used to pass from ρ and T to P and s, where $s = S/N$ is the entropy per unity molecule. Moreover, passing from the vectorial current field, $\vec{J}(r,t)$, to the longitudinal current, $w = \nabla\cdot\vec{J}$, and the two components of the transverse current, $\mu_{1,2} = (\nabla\times\vec{J})_{1,2}$, the following set of equations is obtained:

$$[\frac{\partial}{\partial t} - (\gamma-1)D_T\nabla^2]\delta P(r,t) + c_s^2 w(r,t) - \langle\rho\rangle\alpha^{-1}(\gamma-1)D_T\nabla^2\delta s(r,t) = 0 \tag{2.31}$$

$$[\frac{\partial}{\partial t} - \nu_L]w(r,t) + \nabla^2\delta P(r,t) = 0 \tag{2.32}$$

$$(\frac{\partial}{\partial t} - D_T\nabla^2)\delta s(r,t) - \alpha\langle\rho\rangle^{-1}D_T\nabla^2\delta P(r,t) = 0 \tag{2.33}$$

$$(\frac{\partial}{\partial t} - \nu_s\nabla^2)\mu_1(r,t) = 0 \tag{2.34}$$

$$(\frac{\partial}{\partial t} - \nu_s\nabla^2)\mu_2(r,t) = 0 \tag{2.35}$$

Where $\nu_s = \eta_s\rho^{-1}$ and $\nu_B = (\eta_s + \frac{2}{3}\eta_d)\rho^{-1}$ are called kinematic shear and bulk viscosity, respectively; $\nu_L = \frac{4}{3}\nu_s + \nu_B$ then denote the longitudinal kinematic viscosity. With this choice of variables the hydrodynamic dispersion equation is straightforwardly obtained by a double Laplace-Fourier transform of eqs.2.31-2.35, and by constructing its coefficient determinant [5, 7]:

$$\begin{pmatrix} [s+(\gamma-1)D_T Q^2] & c_s^2 & \langle\rho\rangle\alpha^{-1}(\gamma-1)D_T Q^2 & 0 & 0 \\ -Q^2 & [s+(\nu_L)] & 0 & 0 & 0 \\ \langle\rho\rangle^{-1}\alpha D_T Q^2 & 0 & [s+D_T Q^2] & 0 & 0 \\ 0 & 0 & 0 & [s+\nu Q^2] & 0 \\ 0 & 0 & 0 & 0 & [s+\nu Q^2] \end{pmatrix} \tag{2.36}$$

The 2×2 minor on the bottom right yields two degenerate solutions:

$$s = -\nu_s Q^2 \tag{2.37}$$

They correspond to non propagating shear modes. These are decoupled from the rest of the matrix and, in particular, from the experimentally observable density fluctuations. For this reason their existence is not experimentally detectable, at least not in the hydrodynamic limit. Mathematically, they factorize in equation 2.30, and the hydrodynamic matrix is simplified to the 3×3 top-left minor, which produces the following 3rd order dispersion equation:

$$s^3 + s^2(\gamma D_T Q^2 + \nu_L Q^2) + s(c^2 Q^2 + \gamma D_T \nu_L Q^4) + D_T c^2 Q^4 = 0 \tag{2.38}$$

Neglecting the Q^4 terms, with respect to the Q^2 ones, the following solutions are obtained:

$$s_0 = -D_T Q^2 \tag{2.39}$$

and

$$s_\pm = \pm i c_s Q - \Gamma Q^2 \tag{2.40}$$

where

$$\Gamma = \frac{1}{2}[\nu_L + (\gamma - 1) D_T] \tag{2.41}$$

The first solution is related to the coupling between entropy and density fluctuations. It corresponds to a thermal diffusive mode, accounting for non-propagating entropy fluctuations at constant pressure. The two imaginary (oscillatory) solutions arise from the coupling between the longitudinal velocity field and density fluctuations. They fingerprint the existence of propagating modes, corresponding to isentropic pressure fluctuations, also referred to as longitudinal acoustic (LA) modes. They propagate with the adiabatic sound velocity, c_s, and have a lifetime (damping) given by $(\Gamma Q^2)^{-1}$. The LA and thermal diffusive modes are coupled together through the $(1, 3)$ and $(3, 1)$ matrix elements. This coupling is weak for ordinary fluids in the hydrodynamic limit. In summary, the 5 hydrodynamic modes are:

a) Two shear modes, decoupled from all the other modes and decoupled from density fluctuations.

b) Three longitudinal modes, coupled to density fluctuations. They consist of one non-propagating entropy mode, associated to thermal diffusion process, and two propagating (acoustic) modes.

These five hydrodynamic modes are summarized in fig.2.2:

Acoustic Modes		
	Entropy Modes	
		Shear Modes

Figure 2.2: *Schematic sketch of the five hydrodynamics modes.*

The formal correlation function for density fluctuations in the Fourier-Laplace space is then derived from equation 2.30, considering only the 3×3 minor[6]:

$$\langle \delta\rho(Q,0)^* \delta\rho(Q,s)\rangle = \frac{(s+\nu_L Q^2)(s+\gamma D_T Q^2) + (1-\gamma^{-1})c_s^2 Q^2}{(s-s_0)(s-s_+)(s-s_-)} \langle \delta\rho^*(Q,0)\delta\rho(Q,0)\rangle \tag{2.42}$$

where s_0 and $s_\pm$ are the solutions of the dispersion relation, given in eqs.2.39 and 2.40, while $\langle \delta\rho^*(Q,0)\delta\rho(Q,0)\rangle$ is the static structure factor, $S(Q)$. Passing from Laplace to Fourier space and neglecting the terms $\propto Q^4$ with respect to the ones $\propto Q^2$, after some straightforward algebra, the so-called Rayleigh-Brillouin spectrum is obtained:

$$\begin{aligned} \frac{S(Q,\omega)}{S(Q)} &= \frac{\gamma-1}{\gamma}\frac{2D_T Q^2}{\omega^2 + (D_T Q^2)} + \frac{1}{\gamma}\Big[\frac{\Gamma Q^2}{(\omega + c_s Q)^2 + (\Gamma Q^2)^2} + \frac{\Gamma Q^2}{(\omega - c_s Q)^2 + (\Gamma Q^2)^2}\Big] + \\ &+ \frac{Q}{\gamma c_s}[\Gamma + (\gamma-1)D_T]\Big[\frac{(\omega + c_s Q)}{(\omega + c_s Q)^2 + (\Gamma Q^2)^2} - \frac{(\omega - c_s Q)}{(\omega + c_s Q)^2 + (\Gamma Q^2)^2}\Big] \end{aligned} \tag{2.43}$$

This spectrum is composed of a sum of three Lorentian functions (see fig.2.3). The peak centered at $\omega = 0$, whose width is given by $D_T Q^2$, is usually called the Rayleigh peak. It accounts for the non-propagating density fluctuations (thermal diffusive mode). The other two Lorentians are symmetrically centered at $\pm c_s Q$ and have a width given by ΓQ^2. These two side peaks are usually referred to as the Stokes and anti-Stokes component of the Brillouin doublet. They represent the constant entropy density fluctuations (longitudinal acoustic modes), that propagate with the adiabatic sound velocity, and are damped by both thermal diffusion and viscous dissipations (see eq.2.41). There is also a small asymmetric term that ensures the fulfilment of the 1th sum rule for a classical fluid. On the other hand this asymmetric term vanishes by integration over ω, so that the correct value of $S(Q)$ (0th sum rule) is preserved. Moreover, the ratio between the integrated intensities of Brillouin ($2I_B$) and Rayleigh (I_R)

[6]It can be demonstrated that $\langle \rho^*(Q,0)J(Q,0)\rangle = \langle \rho^*(Q,0)\delta T(Q,0)\rangle = 0$.

peaks is related to the specific heat ratio: $\gamma = (I_R/2I_B) - 1$. This relation is usually called the Landau-Placzek ratio.

Despite the fact that the Rayleigh-Brillouin spectrum describes the experimentally measured spectral density of simple fluids in their hydrodynamic limit extremely well, the measured spectra have high-frequency tails that decrease faster than a Lorentian function. Furthermore, the spectrum represented in eq.2.43 does not obey the 2nd sum rule; in fact the integral over ω of $\omega^2 S(Q,\omega)$ diverges.

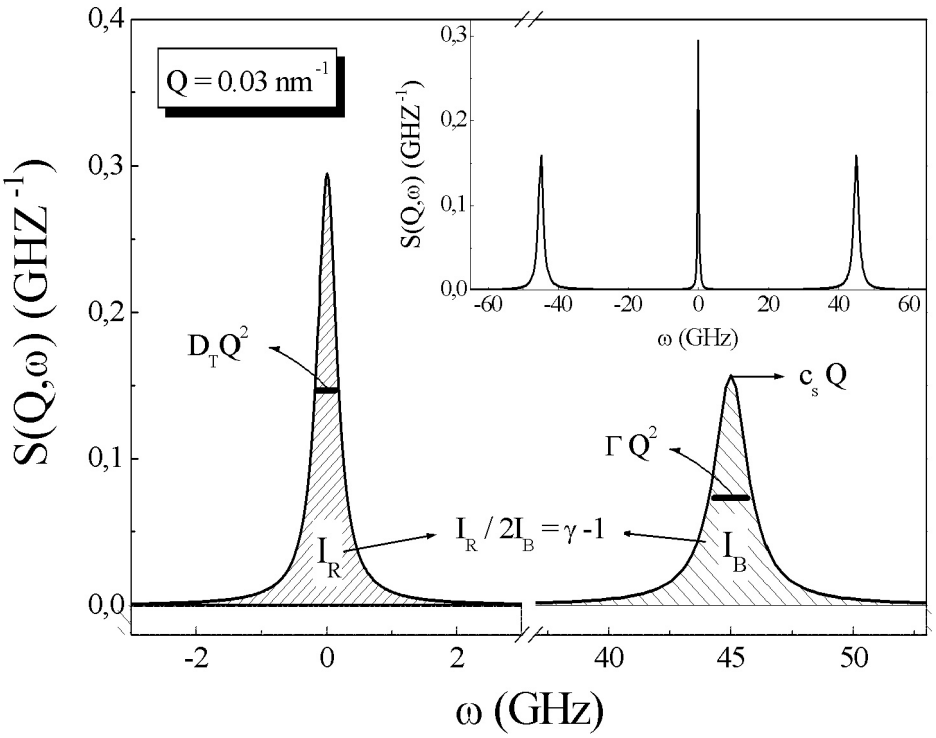

Figure 2.3: *Example of a Rayleigh-Brillouin spectrum for a generic liquid with the following parameters:* $\gamma = 1.2$, $D_T = 200\ nm^2/ps$, $c_s = 1500\ m/s$, $\Gamma_L = 900\ nm^2/ps$ *and* $Q = 0.03\ nm^{-1}$. *The inset reports the total spectrum, including the Anti-Stokes side.*

An alternative description consists of replacing the two symmetric side Lorentians and the asymmetric term by a damped harmonic oscillator (DHO) function:

$$\frac{S(Q,\omega)}{S(Q)} = \frac{1}{\pi}\frac{\Omega_0\Gamma_0^2}{[\omega^2 - \Omega_0^2]^2 + \omega^2\Gamma_0^2} \tag{2.44}$$

This function is the (Q,ω)-expression of the equation of motion of a harmonic oscillator that oscillates with frequency Ω_0 and is damped by a factor $e^{-\Gamma_0 t}$. Inspecting the two conjugate roots of eq.2.40, it is straightforward to associate Ω_0 with $c_s Q$ and Γ_0 with Γ. Equation 2.44 can be derived directly from eq.2.30, if the terms $\propto Q^4$ are

not neglected. It is then natural to use this function to describe the Brillouin peaks. Furthermore, if we limit our consideration only to the acoustic part of the spectra, the DHO expression preserves the sum rules up to the 3rd order.

2.4 The memory function approach

The main idea of this theoretical approach is to describe the complex dynamics of a strongly interacting system, such as a liquid, using a limited number of dynamical variables. The first step is thus to rewrite the equations of the N-body dynamics in terms of these variables in a formally exact fashion.

2.4.1 Rephrasing of the many body dynamical problem

The Hamiltonian, H, of a system made of N interacting particles depends on the coordinates, r_i, and momenta, p_i, of each particle. Considering a set of $\nu < N$ dynamical variables, $A_\nu(t)$, and neglecting an explicit temporal dependence of H, the equation of motion of $A_\nu(t)$ is ruled by the Liouville operator, iL [7, 8]:

$$\frac{dA_\nu(t)}{dt} = [dA_\nu(t), H] = iLA_\nu(t) \tag{2.45}$$

Where $[..., ...]$ are the Poisson brackets. In the case that the particles i and j interact with each other through a pairwise central potential, $h(r_{i,j})$, the Liouville operator assumes the following form:

$$iL = \frac{1}{m}\sum_{i=1}^{N} p_i \cdot \frac{\partial}{\partial r_i} - \sum_{i\neq j} \frac{\partial h(r_{i,j})}{\partial r_i}\frac{\partial}{\partial p_i} \tag{2.46}$$

Equation 2.45 can be formally solved yielding:

$$A_\nu(t) = e^{iLt}A_\nu(0) \tag{2.47}$$

The solution is thus given in terms of the propagator e^{iLt}. Eq.2.47 is too complicated to be applied in practice. Nevertheless, the problem can be rephrased in a different way. First, one defines a projector operator, $\wp$, as follows:

$$\wp \equiv (\vec{A}(0), ...) \cdot (\vec{A}(0), \vec{A}(0))^{-1}\vec{A}(0) \tag{2.48}$$

where $\vec{A}$ is an n-dimensional vector whose components are the A_ν, and $(..., ...)$ denotes the scalar product. If $\wp$ is applied to an arbitrary dynamical variable, the "portion" of such variable that lies in the subspace defined by the set (A_ν) can be extracted. After some straightforward algebra, the equation of motion can be reformulated as follows [7, 8]:

$$\frac{d\vec{A}(t)}{dt} = i\Omega \cdot \vec{A}(t) - \int_0^t K(\tau) \cdot \vec{A}(t-\tau)d\tau + \vec{f}(t) \tag{2.49}$$

The quantities appearing in eq.2.49 have the following meaning:

- $i\Omega = (\vec{A}(0), iL\vec{A}(0)) \cdot (\vec{A}(0), \vec{A}(0))^{-1}$ is an $n \times n$ antisymmetrical matrix, called proper frequency matrix. It can be valuated in terms of equilibrium (statical) properties of the system[7].
- $\vec{f}(t) = e^{i(1-\wp)Lt} i(1-\wp)L\vec{A}(0)$ is called fluctuating force. The presence of the term $(1-\wp)$ has the important consequence that $(\vec{A}(0), \vec{f}(t)) = 0$. The fluctuating force is always orthogonal to $\vec{A}(0)$.
- $K(t) = (\vec{f}, \vec{f}(t)) \cdot (\vec{A}(0), \vec{A}(0))^{-1}$ is a $n \times n$ matrix, called memory matrix or memory function if the set A_ν reduces to only one variable.

From eq.2.49 it is easy to construct the equation of motion for the correlation matrix $C(t) = \langle \vec{A}(t)\vec{A}(0)\rangle$. Exploiting the orthogonality of $\vec{A}(0)$ and $\vec{f}(t)$ one obtains:

$$\frac{dC(t)}{dt} = i\Omega \cdot C(t) - \int_0^t K(\tau) \cdot C(t-\tau) d\tau \tag{2.50}$$

Equations 2.49 and 2.50 are the so-called memory equations or generalized Langevin equations. Since Ω can be calculated from statical properties of the system, the dynamical problem is now transposed from $C(t)$ to $K(t)$.

2.4.2 Time dependence of the memory function

The static, $t = 0$, behavior of $K(t)$ is related to the normalized frequency momenta, $\langle \omega^n \rangle$, of $C(\omega)$, the Fourier transform of $C(t)$ [7, 8]:

$$\langle \omega^n \rangle = i^n [\frac{d^n C(t)}{dt^n}]_{t=0} \cdot [C(0)]^{-1} = \int_{-\infty}^{+\infty} \omega^n C(\omega) d\omega \cdot [C(0)]^{-1} \tag{2.51}$$

The following relations can be obtained:

$$\Omega = \langle \omega \rangle \tag{2.52}$$

$$K(0) = \langle \omega^2 \rangle - \langle \omega \rangle \cdot \langle \omega \rangle \tag{2.53}$$

$$\dot{K}(0) = i[\langle \omega^3 \rangle - 2\langle \omega^2 \rangle \cdot \langle \omega \rangle + \langle \omega \rangle \cdot \langle \omega \rangle \cdot \langle \omega \rangle] \tag{2.54}$$

$$\ddot{K}(0) = -\langle \omega^4 \rangle + 2\langle \omega^3 \rangle \cdot \langle \omega \rangle + \langle \omega^2 \rangle \cdot \langle \omega^2 \rangle + \langle \omega \rangle \cdot \langle \omega \rangle \cdot \langle \omega \rangle \cdot \langle \omega \rangle \tag{2.55}$$

The above relations can be simplified if the vector of dynamical variables, $\vec{A}$, consists of only one component (single-variable case). In this case all the odd frequency moments of $C(\omega)$ vanish. In the following only this case will be considered. The initial behavior of $K(t)$ can be therefore obtained by a Taylor series expansion:

$$K(t) = K(0) + \ddot{K}(0)\frac{t^2}{2} + ... = K(0)[1 - (\frac{t}{\tau_0})^2 + ...] \tag{2.56}$$

[7] note that from eq.2.45 $iL\vec{A}(0) = [\frac{d\vec{A}(t)}{dt}]_{t=0}$

Where $K(0) = \langle\omega^2\rangle$ and $\ddot{K}(0) = \langle\omega^2\rangle^2 - \langle\omega^4\rangle$ and thus:

$$\tau_0 = [\frac{-\ddot{K}(0)}{2K(0)}]^{-1/2} = [\frac{\langle\omega^4\rangle - \langle\omega^2\rangle^2}{2\langle\omega^2\rangle}]^{-1/2} \tag{2.57}$$

Within this very crude approximation the short time behavior of the memory function is simply governed by a characteristic time-decay, τ_0. A more accurate description of the time dependence of the memory function implies the exploitation of higher order spectral momenta, which are very difficult to handle in practice.

Nevertheless, the mathematical structure of eq.2.50 allows the obtention of a recursive formula, called the continued fraction expansion [7, 8]. In fact, eq.2.50 reads in the Laplace space:

$$C(s) = \frac{C(0)}{s + K(s)} \tag{2.58}$$

The memory function $K(t)$ is the correlation function of the fluctuating force, $f(t)$. Therefore another projector operator can be defined:

$$\wp_1 \equiv \frac{(f(0), ...)}{(f(0), f(0))} f(0) \tag{2.59}$$

where $\wp_1$ projects on the functional sub-space of f. Using this operator a generalized Liouville equation for $f(t)$ can be written:

$$\frac{df(t)}{dt} = -\int_0^t K_1(\tau) f(t-\tau) d\tau + f_1(t) \tag{2.60}$$

where $f_1(t)$ is a new fluctuating force, orthogonal both to $A(t)$ and $f(t)$, while $K_1(t) = (f_1(0), f_1(t))/(f(0), f(0))$ is called the 2nd order memory function. This name is rather clear because, in analogy to eq.2.50, one obtains an exact memory equation for the memory function itself:

$$\frac{dK(t)}{dt} = -\int_0^t K_1(\tau) \cdot K(t-\tau) d\tau \tag{2.61}$$

eq.2.61, in Laplace space, reads:

$$K(s) = \frac{K(0)}{[s + K_1(s)]} \tag{2.62}$$

Iterating the procedure, an infinite set of equations such as 2.58 and 2.62 can be obtained. Combining all of them, the so-called continued fraction expansion can be derived:

$$\frac{C(s)}{C(0)} = [s + \frac{\Delta_1}{s + \frac{\Delta_2}{s + \frac{\Delta_3}{s + ...}}}]^{-1} \tag{2.63}$$

where the terms Δ_i are the $t = 0$ values of the ith order memory function. They are static quantities and can be expressed in terms of spectral momenta:

$$\Delta_1 \equiv K(0) = \langle \omega^2 \rangle \tag{2.64}$$

$$\Delta_2 \equiv K_1(0) = -\frac{\ddot{K(0)}}{2K(0)} = \frac{\langle \omega^4 \rangle}{\langle \omega^2 \rangle} - \langle \omega^2 \rangle \tag{2.65}$$

$$\Delta_3 \equiv K_2(0) = -\frac{\ddot{K_1(0)}}{2K_1(0)} = \frac{1}{\Delta_2}[\frac{\langle \omega^6 \rangle}{\langle \omega^2 \rangle} - (\frac{\langle \omega^4 \rangle}{\langle \omega^2 \rangle})^2] \tag{2.66}$$

2.4.3 The case of density fluctuations

An expression for the intermediate scattering function in the Laplace space can be easily obtained using equation 2.63 for the space Fourier transform of the Van-Hove pair correlation function:

$$\frac{F(Q,s)}{F(Q,0)} = [s + \frac{\Delta_1}{s + \frac{\Delta_2}{s + \frac{\Delta_3}{s + \ldots}}}]^{-1} \tag{2.67}$$

where $F(Q,0) = S(Q)$ and the Δ_i are now expressed in terms of spectral momenta of density fluctuations, i.e. the sum rules of $S(Q,\omega)$, tabulated in table 2.1. If the expansion is limited to the second order, one obtains:

$$\frac{F(Q,s)}{S(Q)} = [s + \frac{\langle \omega^2 \rangle}{s + m_L(Q,s)}]^{-1} \tag{2.68}$$

where $m_L(Q,s)$ is the second order memory function for density fluctuations and $\langle \omega^2 \rangle$ is the second spectral moment of the $S(Q,\omega)$. It can be related to the finite-Q generalization of the isothermal sound velocity, $c_T(Q)$, through the relation [7, 8]:

$$\langle \omega^2 \rangle = K_B T Q^2 / M S(Q) = c_T^2(Q) Q^2 \tag{2.69}$$

Exploiting the relation between the Laplace and Fourier transform, the dynamical structure factor can be directly obtained from eq.2.68:

$$\frac{S(Q,\omega)}{S(Q)} = \frac{1}{\pi}\Re[\frac{F(Q,s=i\omega)}{S(Q)}] = \frac{1}{\pi}\Re[i\omega + \frac{c_T^2(Q)Q^2}{i\omega + m_L(Q,s=i\omega)}]^{-1} \tag{2.70}$$

This can be cast into the more common expression:

$$\frac{S(Q,\omega)}{S(Q)} = \frac{1}{\pi}\frac{(c_T(Q)Q)^2 m_L'(Q,\omega)}{[\omega^2 - (c_T(Q)Q)^2 - \omega m_L''(Q,\omega)]^2 + \omega^2[m_L'(Q,\omega)]^2} \tag{2.71}$$

where $m_L'(Q,\omega)$ and $m_L''(Q,\omega)$ are, respectively, the real and imaginary part of the memory function in Fourier space.

Since the $t = 0$ value of the memory function is known from eq.2.65, $S(Q,\omega)$ can be fully determined once the time dependence of the memory function is known. The starting point to calculate this time dependence is to compare the result of the intermediate scattering function, both obtained through the memory function formalism

(eq.2.68) and from the classical hydrodynamics theory (eq.2.42). The latter, after some algebra, reads:

$$[\frac{F(Q,s)}{S(Q)}]_{hydro} = [s + \frac{(c_T Q)^2}{s + 2\Gamma Q^2 + \frac{(\gamma-1)(c_T Q)^2}{s+D_T Q^2}}]^{-1} \tag{2.72}$$

Comparing eqs.2.68 and 2.72, the following expression for the memory function can be derived in the time domain:

$$m_{L,RB}(Q,t) = (\gamma-1)(c_T Q)^2 e^{-\gamma D_T Q^2 t} + 2\Gamma Q^2 \delta(t) \tag{2.73}$$

The subscript "RB" emphasizes the fact that this memory function has been directly derived from the comparison with the Rayleigh-Brillouin spectrum.

This memory function contains two terms which account for its time decay from the initial ($t = 0$) value down to zero. The second term on the right hand side of eq.2.73 describes an instantaneous (i.e. $\propto \delta(t)$) time decay. The first term, instead, has a finite decay time: $\tau_T = 1/\gamma D_T Q^2$. In the following, this will be referred to as thermal relaxation time. The Fourier transform of eq.2.73 yields:

$$m'_{L,RB}(Q,\omega) = (\gamma-1)(c_T Q)^2 \frac{\tau_T}{1+(\omega\tau_T)^2} + \Gamma Q^2 \tag{2.74}$$

$$\omega m''_{L,RB}(Q,\omega) = (\gamma-1)(c_T Q)^2 \frac{(\omega\tau_T)^2}{1+(\omega\tau_T)^2} \tag{2.75}$$

In order to compare the results of the Raleigh-Brillouin spectrum (eq.2.43) with the spectra derived from eqs.2.71, 2.74 and 2.75, the hydrodynamic (i.e. the low-Q and low-ω) limit of the latter equations must be considered. In this limit τ_T is much longer than the period of inelastic excitations, $\Omega_L^{-1}(Q)$, since the latter is $\propto Q^{-1}$ while the former is $\propto Q^{-2}$. As a consequence, the condition $\omega\tau_T \gg 1$ is always satisfied, and eqs.2.74 and 2.75 reduce to:

$$m'_{L,RB}(Q,\omega) \simeq \Gamma Q^2 \tag{2.76}$$

$$\omega m''_{L,RB}(Q,\omega) \simeq [(c_s Q)^2 - (c_T Q)^2] \tag{2.77}$$

where the general thermodynamic relation: $c_s(Q) = \gamma^{1/2} c_T(Q)$ has been exploited. The comparison between the Raleigh-Brillouin spectrum and the spectrum obtained using the memory function formalism is shown in fig.2.4. The memory function expressed in eq.2.73 is thus able to reproduce the Rayleigh-Brillouin spectrum very well. Moreover, at frequencies much higher than the Brillouin peak position, the spectral tails decay as $\propto \omega^{-4}$, and the 2nd sum rule is always preserved, contrary to the classical hydrodynamic description.

The agreement between the memory function and the classical hydrodynamic description is a direct consequence of the assumption: $\omega\tau_T \gg 1$. Experimentally this assumption is always satisfied if ultrasonic (US) or light-scattering (LS) inelastic spectroscopies are employed. The only exception is the case of liquid metals [19]. Here,

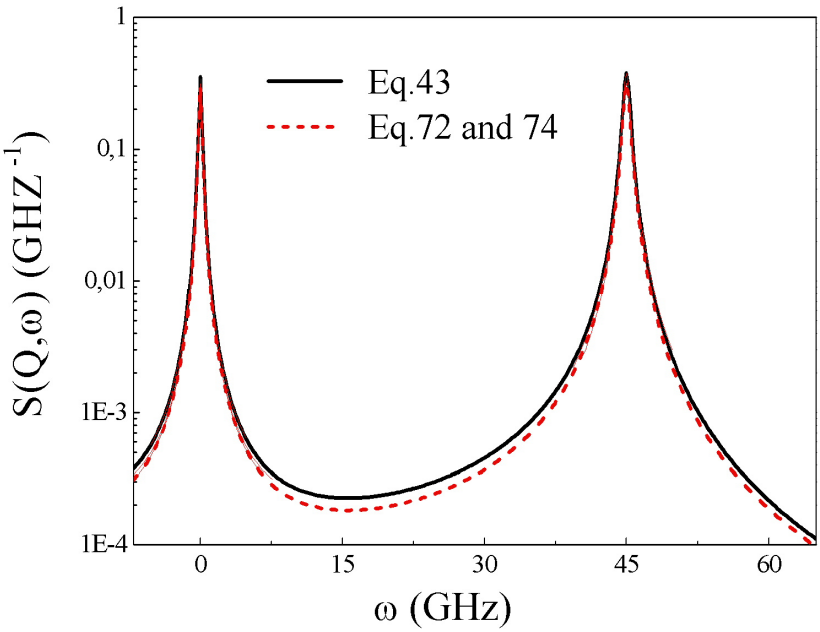

Figure 2.4: *Comparison between the Rayleigh-Brillouin spectrum (eq.2.43), black solid line, and the spectrum obtained from eqs.2.71 and 2.73, red dashed line.*

the thermal diffusivity is so high -and consequently τ_T so short-, that the condition $\omega\tau_T \sim 1$ can be fulfilled in the LS region.

2.4.4 Relaxation processes

In the previous section the results of classical hydrodynamics were derived with a particular choice for the time decay (i.e. the relaxation) of the memory function. It is then worthwhile to point out the effects of the relaxation processes of the memory function on $S(Q,\omega)$.

A simple sketch of a generic relaxation process is reported in fig.2.5. A perturbation of magnitude P_1 is applied to the system at time t_1. The effect of such a perturbation is to bring the system from its unperturbed equilibrium position, R_0, to a new equilibrium one, R_1. At the time t_2 the perturbation is removed, and the system returns to R_0[8]. The transition between these equilibrium positions is the relaxation process, which occurs on a characteristic time scale, τ (relaxation time).

An acoustic wave travelling with momentum (Q) and frequency (Ω_L) is an example of a time-dependent perturbation. This wave creates compression-rarefaction zones (CRZ), which are periodic in time ($T = 1/\Omega_L$) and space ($\Lambda = 1/Q$). The wave locally compresses the system, and the energy associated to such compression locally brings the

[8]After the removing of the perturbation the final equilibrium position (i.e. for $t \gg t_2$) could be different from the initial one (i.e. for $t \ll t_1$)

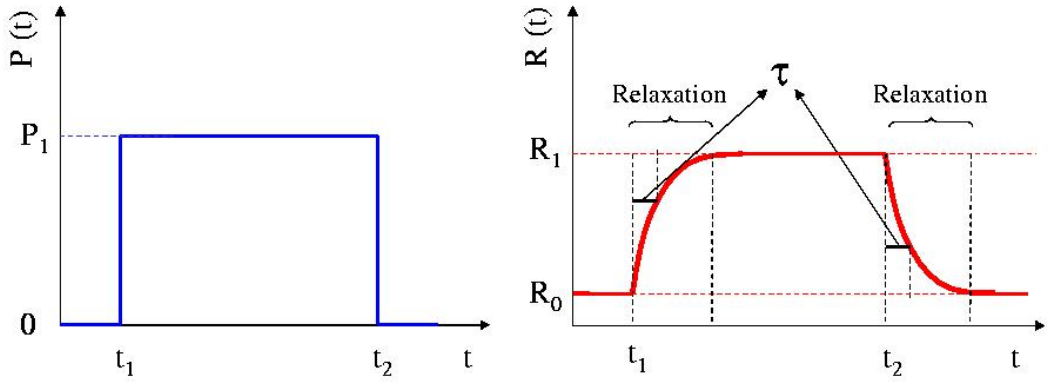

Figure 2.5: *Relaxation process: a time dependent perturbation, $P(t)$ (left panel), is applied to the system. Its response, $R(t)$ is reported in the right panel.*

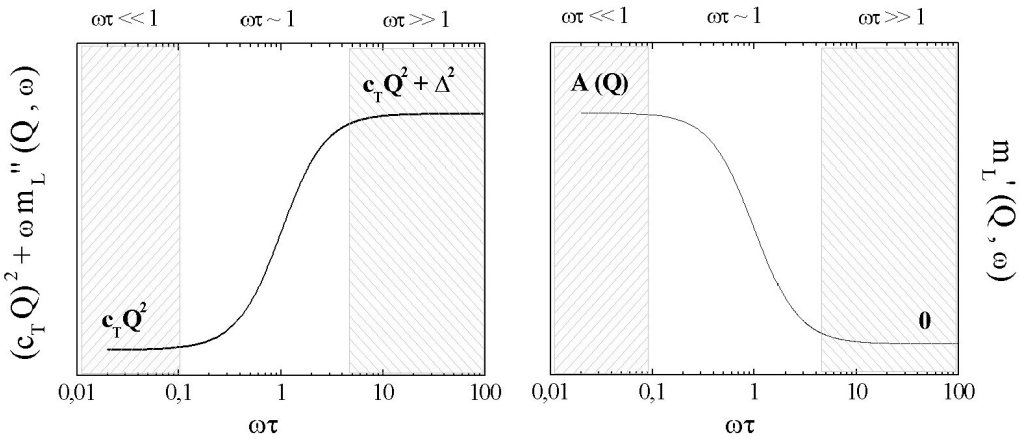

Figure 2.6: *Resonant (left panel) and dissipative (right panel) term of eq.2.71. These quantities represent, respectively, the (squared) characteristic frequency and damping of LA modes.*

system out of the equilibrium. Then the system relaxes into a new equilibrium position after a characteristic time (τ), dissipating the excess of energy. If $T \gg \tau$ the system has enough time to relax into its equilibrium position before the successive perturbation. This situation is also referred to as fully relaxed limit. On the other hand, when $T \ll \tau$ the successive perturbation occurs before the system can relax. This situation is also referred to as fully unrelaxed limit. The intermediate situation, $\tau \sim T$, defines the crossover between the two regimes. Dissipation phenomena that can be associated with a relaxation process are numerous in fluids: e.g. thermal diffusivity, viscous flows, inter-particles collisions, intramolecular vibrations or rotations [20, 21, 22, 23].

Beside the characteristic timescale, also a characteristic strength, Δ^2, can be associated with a relaxation process. In the memory function formalism, Δ^2 represents the $t = 0$ value of the considered relaxation in the memory function. Within the assumption of a single exponential relaxation of the memory function (i.e. $m_L(Q,t) = \Delta^2 e^{-t/\tau}$) the resonant, $(c_T Q)^2 + \omega m''_L(Q,\omega)$, and dissipative, $m'_L(Q,\omega)$, part of the spectra of eq.2.71 behaves as shown in fig.2.6.

The information one can obtain from the analysis of the spectral density, $S(Q,\omega)$, depends on the considered regime:

- Fully relaxed regime ($\omega\tau \ll 1$): the time-decay of $m_L(Q,t)$ is so short compared to the frequency window that it can be approximated by a $\delta(t)$-function: i.e. $m(Q,t) \to 2A(Q)\delta(t)$, with $A(Q) = \int_0^{+\infty} m_L(Q,t)dt$. The only information which can be derived from the $S(Q,\omega)$ is the integral of $m_L(Q,t)$ and the value of c_T.

- Fully unrelaxed regime ($\omega\tau \gg 1$): the physical process responsible for the relaxation occurs on such a long time-scale that the energy carried by acoustic waves cannot be dissipated in this channel. The only information one can derive from $S(Q,\omega)$, once the value of c_T is known, is the relaxation strength, Δ^2, which is responsible for the sound wave velocity increase from c_T to $\sqrt{c_T^2 + \Delta^2}$.

- The crossover regime ($\omega\tau \sim 1$) is the most interesting one, since it is sensitive to both relaxation time (τ) and strength (Δ^2).

In the following, the three relaxation processes, relevant in the present context, are discussed in details.

Thermal Relaxation

The excess of energy stored in the compressed zones can be dissipated via the thermal diffusion process (thermal relaxation). This process is not instantaneous, the time needed to transfer a quantity of heat through the surface surrounding the compressed volume in order to equalize the temperature of CRZ (that are spatially limited $\sim Q^{-3}$) is given by the characteristic time for thermal relaxation: $\tau_T = (\gamma D_T Q^2)^{-1}$. CRZ are not stable in time, but they appear and disappear according to the period of the acoustic wave: $T = 1/\Omega_L(Q) \propto Q^{-1}$. In the low-$Q$ limit thermal diffusion is much slower than the interval between two successive compressions, i.e. $\tau_T \gg T$. As a consequence, successive compressions occur before energy can flow from compressed

to rarefied zones through thermal diffusion. This situation corresponds to the fully unrelaxed limit for the thermal relaxation and characterizes the hydrodynamic regime. As Q increases, the temporal periodicity ($\propto Q^{-1}$) and the spatial extension of the CRZ decrease, leading to a decrease of $\tau_T \propto Q^{-2}$. At a certain point the time needed for heat to flow out of the volume will become so short that a non negligible quantity of energy can be exchanged in between two successive compressions. On further increase of Q the mechanism of energy dissipation through thermal diffusion becomes very efficient, since thermal diffusion becomes rapidly much faster than the acoustic wave.

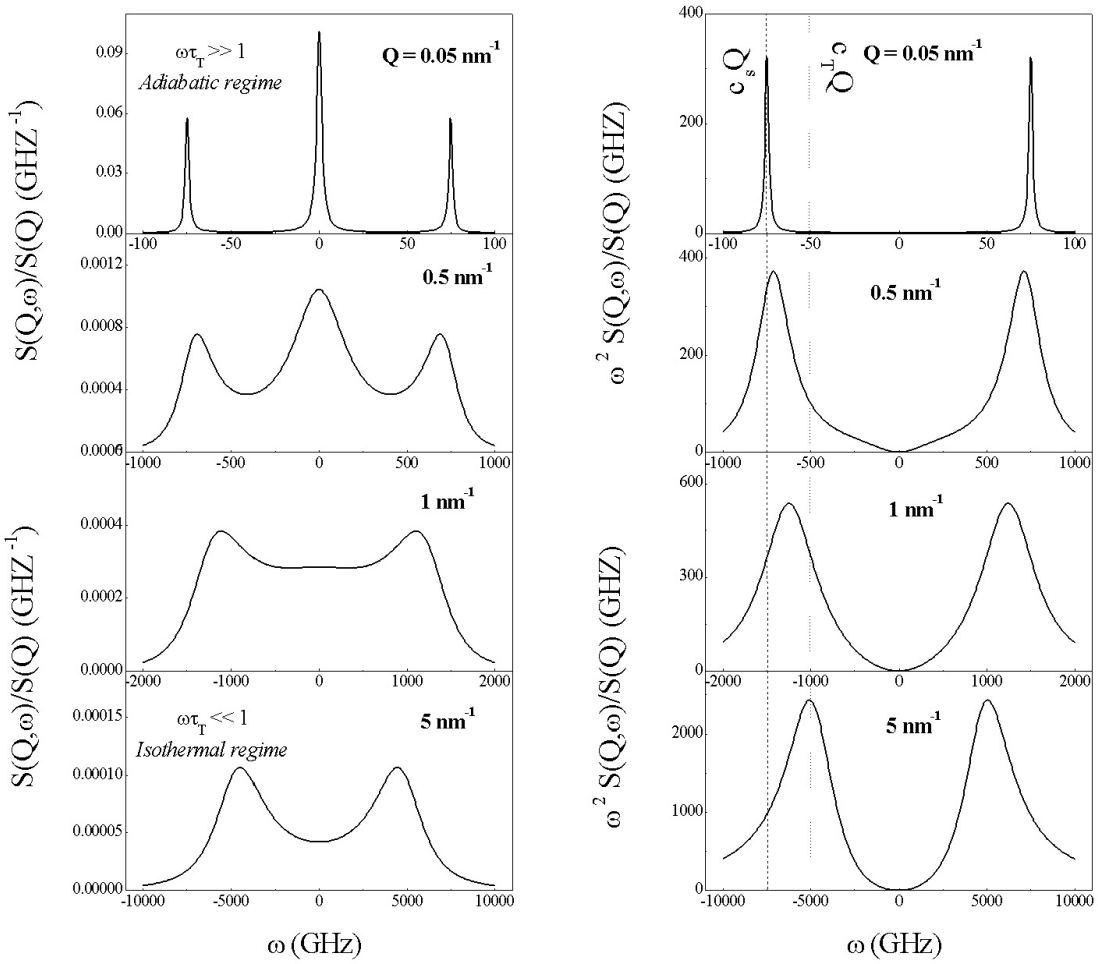

Figure 2.7: Left panels: $S(Q,\omega)$ *as a function of* Q. *The numerical values used to compute these spectra are:* $c_s = 1500\ m/s$, $D_T = 700\ nm^2/ns$, $\Gamma = 100\ nm^2/ns$ *and* $\gamma = 2.25$. Right panels: *corresponding longitudinal current spectra. The vertical lines indicate the expected frequencies of the longitudinal modes in the adiabatic (dashed) and isothermal (dotted) regimes.*

In this fully relaxed limit, $\omega\tau_T \ll 1$, the energy can be dissipated through thermal diffusion in order to equalize the temperature of compressed and rarefied zones. The set of CRZ is therefore in isothermal equilibrium rather than in an adiabatic one. In this limit eqs.2.74 and 2.75 can be approximated as follows:

$$m'_{L,RB}(Q,\omega) \simeq (\gamma - 1)\tau_T(c_T Q)^2 + \Gamma Q^2 \tag{2.78}$$

$$\omega m''_{L,RB}(Q,\omega) \simeq 0 \tag{2.79}$$

The corresponding $S(Q,\omega)$ consists of a DHO function (without the Rayleigh peak) whose maxima are $\pm c_T(Q)Q$, and a damping given by eq.2.78. In the crossover region between the fully relaxed and unrelaxed regimes the three hydrodynamic modes are no longer well separated. The entropy (Rayleigh) mode becomes broader ($\propto Q^2$) and overlaps with the acoustic (Brillouin) ones. The characteristic frequency of the latter, $\Omega_L(Q)$, is no longer equal to $c_s Q$, but lies somewhere in between $c_s Q$ and $c_T Q$. The whole phenomenology is schematically depicted in fig.2.7, where the $S(Q,\omega)$ and the corresponding longitudinal current spectra are reported as a function of Q. The maxima of these spectra correspond to the characteristic frequency of longitudinal modes, Ω_L. In conclusion, a transition from the adiabatic to the isothermal regime of sound propagation is expected to be observed with increasing Q [24, 25]. An estimation of the crossover Q can be obtained by comparing the period of acoustic waves, $1/c_s Q$, with the inverse of the thermal relaxation time, $(\gamma D_T Q^2)^{-1}$. This comparison yields a characteristic crossover Q in the order of $c_s/\gamma D_T$.

Structural Relaxation

The phenomenology of structural relaxation -or viscoelasticiy- has been used since a long time [26, 27, 28] in order to interpret the experimental results concerning the frequency dependence of the sound velocity in the US and LS regimes [21, 22, 23, 29, 30, 31]. In particular this approach is able to correctly explain the very strong frequency and temperature dependence of the sound velocity in glass forming systems near their glass transition temperature [32, 33, 34, 35, 36].

More recently this approach has been successfully employed to interpret the dispersive behavior of longitudinal modes in the Thz range [19, 37, 38, 39, 40, 41, 42, 43]. The starting point is to identify a characteristic time, τ_α, for intermolecular interactions, such as the characteristic life-time of intermolecular bonds or the time between intermolecular collisions. In most liquids, such a characteristic time scale is in the order of ps. When the system is probed on a timescale much shorter than τ_α it appears as "frozen", since the particles have neither the time to move significantly nor to make/break bonds. The response of the system is then expected to be similar to the one of an amorphous solid. In particular, at high-frequencies the characteristic frequency/damping of longitudinal modes is expected to be higher/lower than at low frequencies. This is due to the fact that part of the energy used by the acoustic wave to establish CRZ cannot be dissipated into intermolecular interactions, because of the very short time periodicity of these CRZ, and it contributes to an increase of the sound velocity.

The structural relaxation phenomenology can be easily introduced into the memory function formalism replacing the instantaneous term $(2\Gamma Q^2\delta(t))$ in eq.2.73 by an exponential time decay with time constant τ_α:

$$m_L(Q,t) = (\gamma - 1)(c_T Q)^2 e^{-\gamma D_T Q^2 t} + \Delta_\alpha^2 e^{-t/\tau_\alpha} \tag{2.80}$$

where Δ_α^2 is the strength of the structural relaxation. This substitution does not affect the fulfilment of the correct hydrodynamic limit, since the exponential decay reduces to a delta function for long time scales[9]. In order to quantitatively obtain the hydrodynamic limit, the following assumption has to be made:

$$\Delta_\alpha^2 \tau_\alpha = \Gamma Q^2 \tag{2.81}$$

it can be noted that both $\Delta_\alpha^2 \tau_\alpha$ and ΓQ^2 represent the time integral (i.e. the area) of the "viscous" part of the respective memory functions. Neglecting for simplicity the thermal relaxation in eq.2.80 (e.g. by setting γ=1), the real and imaginary part of the memory function read:

$$m'_L(Q,\omega) = \Delta_\alpha^2 \frac{\tau_\alpha}{1 + (\omega\tau_\alpha)^2} \tag{2.82}$$

$$\omega m''_L(Q,\omega) = \Delta_\alpha^2 \frac{(\omega\tau_\alpha)^2}{1 + (\omega\tau_\alpha)^2} \tag{2.83}$$

The effect of the structural relaxation on the dispersive behavior of longitudinal modes can be predicted by inspecting fig.2.8. For frequencies much lower than τ_α^{-1} (i.e. $\ll THz$) the fully relaxed limit is reached. In this region the sound velocity, $\Omega_L(Q)/Q$, is the adiabatic one[10], and the mode damping is given by eq.2.81. This fully relaxed limit is also called viscous regime, because the system behaves like a viscous fluid that obeys the hydrodynamic laws.

On increasing Q, $\Omega_L(Q)$ linearly increases, up to become comparable to τ_α^{-1}. In this region the sound velocity increases and the damping decreases (see fig.2.6). If Q is increased further, $\Omega_L(Q)$ becomes much larger than τ_α^{-1}. In this fully unrelaxed limit, also called elastic regime, the sound velocity does not increase further, but remains constant. This high frequency sound velocity is usually called c_∞. The relation between c_∞, c_s and Δ_α^2 is:

$$c_\infty^2 - c_s^2 = \Delta_\alpha^2 / Q^2 \tag{2.84}$$

In conclusion, a dispersion of the sound velocity, from a low frequency limit (c_s) to an high frequency one (c_∞), is observed as a function of $\Omega_L(Q)\tau_\alpha$ (positive sound dispersion). The crossover condition can be estimated by comparing τ_α with the period of an acoustic wave, $1/c_s Q$. This comparison yields a crossover Q in the order of $1/c_s\tau_\alpha$. The evolution of the $S(Q,\omega)$ within the viscoelastic scenario is reported in fig.2.8. In the left panels the spectra of a generic viscoelastic liquid (calculated from eqs.2.71 and 2.80) are shown as a function of Q. The fact that there is no Raleigh peak in the low-Q (hydrodynamic limit) is due to the assumption that $\gamma = 1$. Once the unrelaxed limit is approached, a central component becomes visible in the spectra. The width

[9]This is the case of experimental techniques, such as LS or US, that probe an ω-range up to GHz, i.e. $\sim$ three orders of magnitude "slower" than τ_α.

[10]For $\gamma = 1$ there is no difference between adiabatic and isothermal sound velocity.

of this central peak is given by the inverse of the so-called compliance relaxation time $\tau_C = \tau_\alpha c_\infty^2/c_s^2$. In the right panels the corresponding longitudinal current spectra are reported. The vertical lines represent the adiabatic (dashed line) and infinite (dotted line) dispersions. It can be noticed that the sound velocity, $\Omega_L(Q)/Q$, passes from c_s to c_∞ across the transition between the viscous ($\omega\tau_\alpha \ll 1$) and the elastic ($\omega\tau_\alpha \gg 1$) regime.

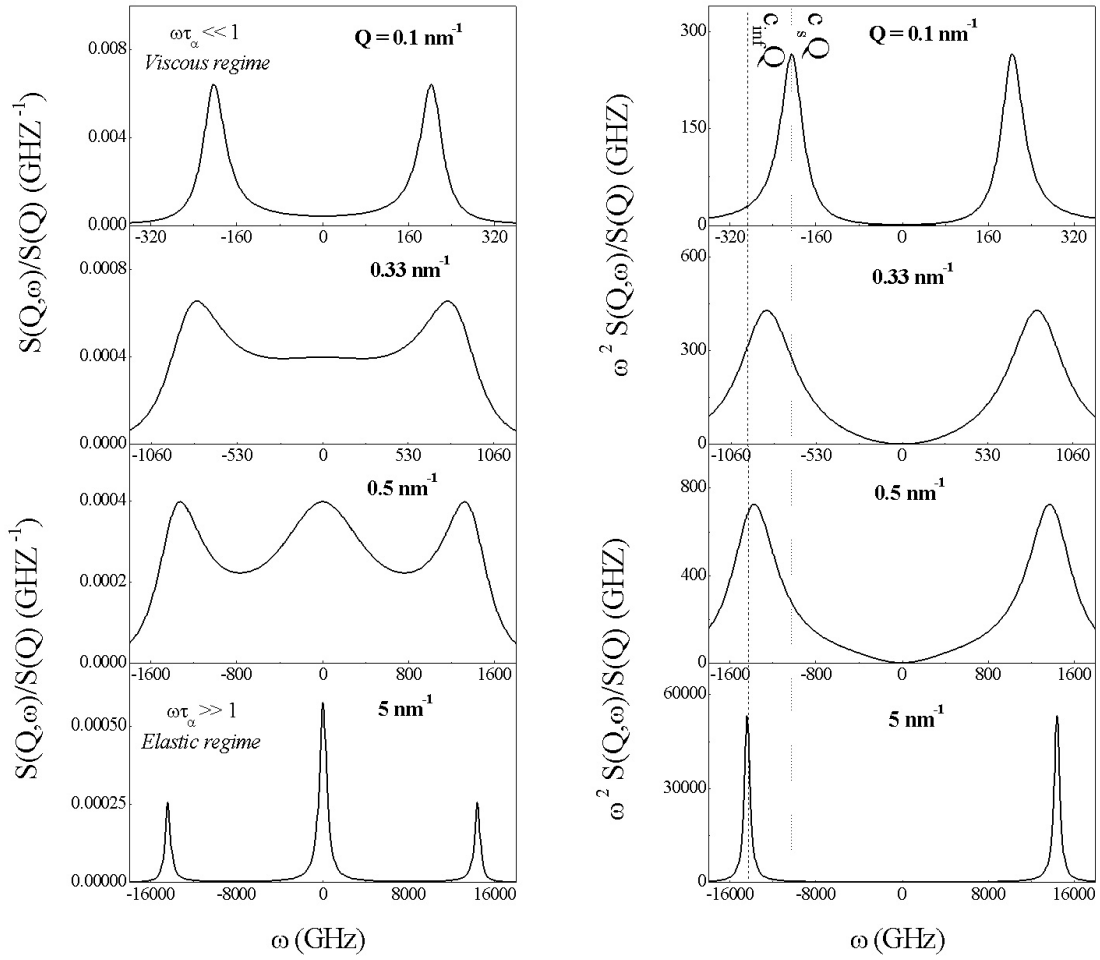

Figure 2.8: Left panels: $S(Q,\omega)$ *of a viscoelastic liquid at the indicated* Q *values. The numerical values used to compute these spectra are:* $c_s = 2000\ m/s$, $c_\infty = 3000\ m/s$ *and* $\tau_\alpha = 1\ ps$. Right panels: *corresponding longitudinal current spectra. The vertical lines indicate the adiabatic (dash) and infinite (dot) dispersion.*

Instantaneous relaxation

On a general ground other dynamical phenomena can take place in fluids. These phenomena can give rise to extra relaxation processes, usually called "microscopic" relaxations. In molecular fluids some of the energy carried by acoustic waves can be dissipated, exciting intramolecular degrees of freedom. In the present context the

only intramolecular degree of freedom is represented by fast intramolecular vibrations. The timescales, τ_μ, of these dynamics are extremely fast. For instance, the period of vibration of N atoms in a N_2 molecule is $\sim 12\ fs$. Moreover, also the topological disorder could give rise to a relaxation process. In fact, when a fluid is probed in its elastic regime, the system appears as "frozen" and its response is similar to the one of the corresponding disordered solid (i.e. the corresponding glass). In this case the eigenstates of the system, in the investigated Q-range, cannot be identified with plane waves [44]. As a consequence, an experimentally excited plane wave results in a projection into different eigenstates with different eigenvalues (frequencies). These eigenstates, after a certain characteristic time, τ_d, dephase each other. This mechanism leads to a relaxation process taking place over a characteristic timescale, τ_d, accounting for energy exchanges between the excited wave and the eigenstates of the system. In principle, several additional terms can be added in the memory function to describe such relaxations [19, 45, 46].

In the present context, these fast dynamics have been taken into account by adding the following term in the memory function:

$$2\Gamma_\mu \delta(t) \tag{2.85}$$

This "instantaneous" time decay of the memory function describes very well the fully relaxed, i.e. $\omega\tau_\mu \ll 1$, region for microscopic relaxations. This condition is likely fulfilled both because τ_μ is quite short[11], and because the very low sound velocity of supercritical samples reduces the ω-region where one is most sensitive to these fast relaxation processes.

2.4.5 The proposed memory function

In the previous section the relevant relaxation processes (thermal, structural and instantaneous) have been discussed. In this section the simultaneous presence of all these effects is briefly illustrated. The memory function we propose to interpret the experimental $S(Q,\omega)$ is derived from eq.2.80, with inclusion of the term in eq.2.85:

$$m_L(Q,t) = (\gamma(Q)-1)(c_T(Q)Q)^2 e^{\tau_T(Q)Q^2 t} + \Delta_\alpha^2(Q) e^{t/\tau_\alpha(Q)} + 2\Gamma_\mu(Q)\delta(t) \tag{2.86}$$

Furthermore, all parameters in eq.2.86 are considered as Q-dependent quantities. This memory function presents two finite time scales, $\tau_T(Q)$ and $\tau_\alpha(Q)$. As one can see from fig.2.7 and 2.8, these relaxations have a competing dispersive effect. The thermal (structural) one is fully unrelaxed (relaxed) at low Q while it is relaxed (unrelaxed) at high Q. In fact, the thermal (structural) relaxation brings the sound velocity to values lower (higher) than the adiabatic one, with increasing Q. The two competing dispersive effects are sketched in fig.2.9, where the arrows indicate the crossover conditions. Nevertheless the crossover condition for the isothermal and the viscoelastic transition can be varied independently, by changing the thermodynamic state of the sample.

[11] With τ_μ we refer to the characteristic timescale of all these fast relaxation processes.

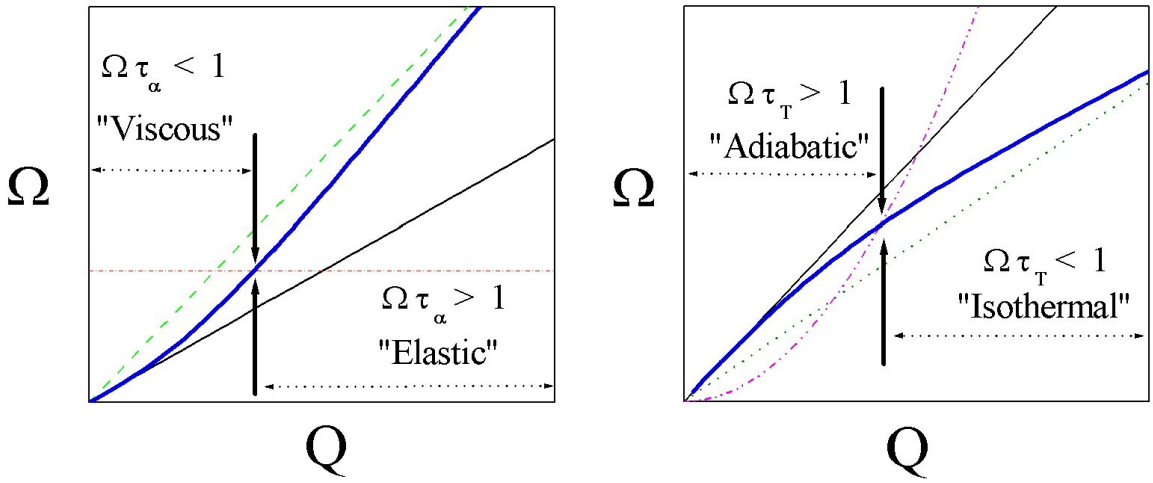

Figure 2.9: *Schematic representation of the dispersive effect of structural relaxation, left panel, and thermal relaxation, right panel. The dispersion of longitudinal modes, $\Omega_L(Q)$, is represented by the thick blue line. The expected adiabatic dispersion is represented by the full black line, while the infinite and isothermal ones are the light-green dashed line and the dark-green dotted one, respectively. The values of τ_T and τ_α are the red dash-dotted line and the magenta dash-double-dotted one, respectively. The crossover between the various regimes is highlighted by the two vertical arrows.*

These two relaxations also influence the damping of longitudinal modes. Moreover, this damping is also affected by the instantaneous relaxation, which leads to an increase of viscous dissipation. On the other hand, the instantaneous relaxation cannot influence the dispersion of longitudinal modes.

The relation between the hydrodynamic viscosity and the relaxations can be obtained by comparing the time integrals of the respective viscous parts of the hydrodynamic (eq.2.73) memory function and the one proposed in eq.2.86. The result is the following:

$$[\Delta_\alpha^2(Q)\tau_\alpha(Q) + \Gamma_\mu(Q)]_{Q\to 0} = \nu_L \tag{2.87}$$

2.5 The single particle limit

In this section we briefly introduce the main features of the single particle limit, which is reached at very high Q-values. The correlation function that plays the crucial role in the description of the single particle behavior is the (self) density correlation function:

$$G_s(\vec{r},t) = \langle \sum_{i=1}^{N} \delta(\vec{r} - (\vec{r_i}(t) - \vec{r_i}(0))) \rangle \tag{2.88}$$

The associated intermediate scattering function is:

$$F_s(\vec{Q},t) = \langle \sum_{i=1}^{N} e^{i\vec{Q}\cdot(\vec{r_i}(t)-\vec{r_i}(0))} \rangle \tag{2.89}$$

whose time Fourier transform is the (self) dynamical structure factor: $S_s(Q,\omega)$. Following the same procedure as in section 2.2.2, $F_s(Q,t)$ can be expanded into a Fourier series, whose coefficients are the spectral momenta of $S_s(Q,\omega)$. The first observation is that for $Q \to \infty$ the spectral momenta of $S(Q,\omega)$ reduce to that of $S_s(Q,\omega)$ (see table 2.1). Therefore the Taylor expansion of $F(Q,t)$ and $F_s(Q,t)$ coincide at high-Q. As a consequence the corresponding spectra are related to each other by the following relation, also referred to as incoherent approximation:

$$S(Q \to \infty, \omega) = S_s(Q \to \infty, \omega) \tag{2.90}$$

$S_s(Q,\omega)$ can be easily calculated in the case of an ideal gas, in which the interactions are mutual collisions, instantaneous and localized in space. The calculation of $G_s(r,t)$ is not particularly challenging in this case, since the probability for a particle to move over a distance r is simply proportional to its velocity, $v = r/t$. This is given by the Maxwell-Boltzmann distribution. Thus $G_s(r,t) \propto e^{-mv^2/2k_BT}$, where m is the mass of the gas particle. Employing the normalization of $G_s(r,t)$ and, double Fourier transforming it, one obtains:

$$S_s(Q,\omega) = (\frac{m}{2\pi k_B T Q^2})^{1/2} e^{-\frac{m}{2k_BTQ^2}\omega^2} \tag{2.91}$$

This is a Gaussian function centered at $\omega = 0$ with variance k_BTQ^2/m. Employing quantum mechanical corrections, the Gaussian function shifts and is centered at the recoil energy, $\Omega_r = \hbar^2 Q^2/2m$ [6, 47].

In order to have a feeling for the Q-region in which this kind of approach is valid, a characteristic length scale for the system has to be defined. One suitable choice is the Enskog mean free path, $L_E = 2/\pi n d^2 g(d)$, where d is the diameter of the particles, here considered as hard spheres. This description is valid when $Q \gg 2\pi/L_E$, and it can be extended to lower values of Q, if final states effect are taken into account.

From the 2nd sum rule of the (self) velocity correlation function, a quantity that plays an important role in the description of fluid dynamics, the Einstein frequency (Ω_0), can be derived. It can be expressed in terms of the second derivative of the pairwise interaction potential, $h(\vec{r})$:

$$\Omega_0 = \frac{Nm}{V} \int_V d\vec{r} g(r) \frac{\partial^2 h(r)}{\partial x^2} \tag{2.92}$$

where x is the component of $\vec{r}$ parallel to $\vec{Q}$. Ω_0 corresponds to the vibration frequency of a molecule inside the cage formed by the nearest neighborhoods potential. These cages are not stable in time, and therefore a real oscillatory motion cannot be rigorously defined. Nevertheless, in dense fluids on short timescales, the motion of a particle can be better described in terms of these time-localized vibrations, rather than pure diffusive motions due to random intermolecular collisions. In this case the inverse

of the Einstein frequency is a more suited parameter to characterize the timescale of microscopic dynamics.

Résumé du chapitre 3

Ce chapitre se concentre sur les aspects expérimentaux de la présente étude. La section efficace pour la Diffusion Inélastique de Rayons-X (IXS) et sa relation avec le facteur de structure dynamique, $S(Q, \omega)$, sont calculées formellement. Une comparaison entre IXS et la Diffusion Inlastique de Neutron (INS), c'est-à-dire la technique expérimentale alternative à IXS, est donnée. A la fin de ce chapitre les principes de fonctionnement d'un spectromètre IXS, ainsi que les appareils expérimentaux employés, sont présentés.

Chapter 3

Inelastic X-Ray Scattering from fluids

In the first sections of this chapter the theory of Inelastic X-ray Scattering (IXS) is presented. Moreover, the basic working principles of an IXS spectrometer, with reference to beamline ID-28 at the European Synchrotron Radiation Facility (ESRF), are illustrated. The use of large volume pressure cells (LVC) is discussed in the final section of this chapter.

3.1 IXS cross-section

The IXS spectrum provides a direct determination of the coherent dynamical structure factor, $S(Q, \omega)$, whenever the listed hypotheses hold [48, 49]:

- The scattering process is dominated by the Thomson term and both the resonant and the spin-dependent contributions to the electron-photon interaction can be neglected.
- The center of mass of the electron cloud follows without delay the nuclear motion, i.e. the adiabatic approximation is valid.
- There are no electronic excitations in the considered energy transfer range.

The IXS scattering schematics are illustrated in fig.1. Here, and in the following, the suffixes "i" and "f" refer to the incident and scattered photon, respectively. The incoming photon is characterized by its energy, $\hbar\omega_i$, wave-vector, $\vec{k}_i$, and polarization, $\widehat{\varepsilon}_i$. It is scattered by the sample into an angle 2θ within a solid angle $d\Omega$. The scattered photon energy, wave-vector and polarization are denoted by $\hbar\omega_f$, $\vec{k}_f$ and $\widehat{\varepsilon}_f$, respectively. According to energy and momentum conservation laws the momentum and energy transfer to the sample are:

$$\hbar\omega \equiv \hbar(\omega_f - \omega_i) \qquad \text{and} \qquad \hbar\vec{Q} \equiv \hbar\left(\vec{k}_f - \vec{k}_i\right) \tag{3.1}$$

In the limit $\omega \ll \omega_i$ -which is the case of IXS-, the modulus of $\vec{k}_i$ and $\vec{k}_f$ are basically the same, and the modulus of the exchanged momentum is entirely determined by the scattering angle 2θ:

$$|\vec{Q}| = 2|\vec{k}_i|sin(2\theta/2) \tag{3.2}$$

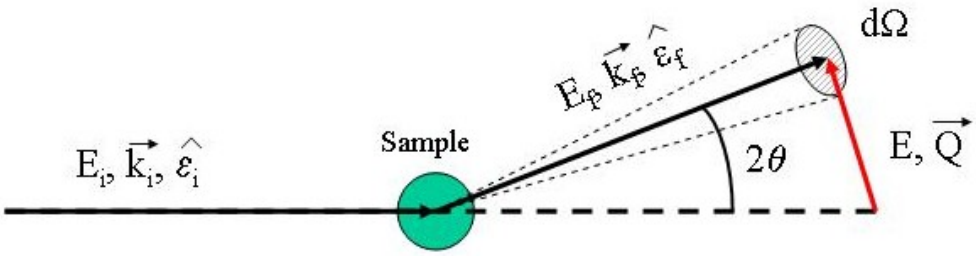

Figure 3.1: *Kinematics of a scattering experiment.*

The double differential cross section, $\partial^2\sigma/\partial\Omega\partial\omega_f$, represents the fraction of photons, having frequency $\omega_f \pm d\omega_f$, scattered into a solid angle $d\Omega$ around the direction defined by $\vec{k}_f$. It can be calculated within the frame of linear response theory assuming a weak coupling between the probe and the system. In this approximation the double differential cross section can be regarded as an intrinsic property of the unperturbed sample, being independent of the incident photon flux. Neglecting the interaction of the photon electromagnetic field with the nuclei, the probe-system interaction, in the weak relativistic limit, is described by the photon-electron interaction Hamiltonian, H_{int}. It consists of four different terms [50]:

$$\begin{aligned} H_{int} = \frac{e^2}{2mc^2}\sum_j \vec{A}(\vec{r}_j,t)\cdot\vec{A}^*(\vec{r}_j,t) + \frac{e}{2mc}\sum_j \vec{A}(\vec{r}_j,t)\cdot\vec{p}_j(\vec{r}_j,t) \\ -\frac{e}{mc}\sum_j \vec{s}_j\cdot\nabla\times\vec{A}(\vec{r}_j,t) - \frac{e^2}{2m^4c^4}\sum_j \vec{s}_j\cdot(\frac{d\vec{A}}{dt}(\vec{r}_j,t)\times\vec{A}(\vec{r}_j,t)) \end{aligned} \tag{3.3}$$

The sum extends over all the electrons in the system, while electron positions, momenta and spins are indicated as $\vec{r}_j$, $\vec{p}_j$ and $\vec{s}_j$, respectively. m and e are the electron mass and charge, while c is the speed of light. Finally $\vec{A}(\vec{r}_j,t)$ is the vector potential of the photon electromagnetic field, which, in the quantum electrodynamic representation with the gauge $\nabla\cdot\vec{A}(\vec{r}_j,t) = 0$, can be written as [51]:

$$\vec{A}(\vec{r}_j,t) = (\frac{4\pi c^2}{V})^{1/2}\sum_\lambda [a_\lambda\hat{\epsilon}_\lambda e^{i(\vec{Q}_\lambda\cdot\vec{r}_j)} + a^*_\lambda\hat{\epsilon}_\lambda e^{-i(\vec{Q}_\lambda\cdot\vec{r}_j)}] \tag{3.4}$$

where a_λ and a^*_λ are the λ-th component of the photon annihilation and creation operator, and $\hat{\epsilon}_\lambda$ is the polarization of the electromagnetic field.

The first term in equation 3.3 describes the diamagnetic coupling between electron current and photon electric field (Thomson scattering). The second term accounts for

the paramagnetic coupling responsible for the absorption/emission of a photon by the electron system. The last two terms describe the coupling of the electron spins to the photon magnetic field and the spin-orbit interaction.

For photon energies of the order of 20 keV (i.e. $\ll mc^2$, the rest mass of the electron) the magnetic terms are by a factor 10^{-2} smaller than the first two terms, and will therefore be neglected in the following. Furthermore, the paramagnetic contribution can be neglected if we consider photons with energies that are far from any absorption resonance. The interaction Hamiltonian therefore simplifies to:

$$H_{int} = \frac{e^2}{2mc^2} \sum_j \vec{A}(\vec{r}_j, t) \cdot \vec{A}^*(\vec{r}_j, t) \tag{3.5}$$

The double-differential cross-section can be determined in the framework of first order perturbation theory, according to Fermi's golden rule [52]. Considering the initial and final photon states, $|I\rangle$ and $|F\rangle$, as plane waves the double-differential cross-section can be written as:

$$\frac{\partial^2 \sigma}{\partial \Omega \partial \omega_f} = r_0^2 \left(\frac{k_f}{k_i}\right) (\hat{\varepsilon}_f \cdot \hat{\varepsilon}_i)^2 \sum_{I,F} P_I \left| \left\langle F \left| \sum_j e^{i\vec{Q} \cdot \vec{r}_j} \right| I \right\rangle \right|^2 \delta(\hbar(\omega - \omega_F + \omega_I)) \tag{3.6}$$

where $r_0 = e^2/mc^2$ is the classical electron radius and P_I is the statistical weight, i.e. the equilibrium population of the initial states.

Within the validity of the adiabatic approximation, the atomic quantum state, $|S\rangle$, can be factorized into its electronic, $|S_e\rangle$, and nuclear, $|S_n\rangle$, part. This approximation is particularly good for exchanged energies that are small with respect to the electron excitation energies. In this case the contribution to the total scattering coming from the valence electrons close to the Fermi level is small compared to the contribution coming from the core electrons. Consequently, the difference between the initial and final state is substantially due to excitations of the ion system. The double differential cross section, under these hypotheses, can be written as:

$$\frac{\partial^2 \sigma}{\partial \Omega \partial \omega_f} = r_0^2 \left(\frac{k_f}{k_i}\right) (\hat{\epsilon}_f \cdot \hat{\epsilon}_i)^2 \sum_{I_n, F_n} P_{I_n} \left| \left\langle F_n \left| \sum_j f_j(Q)\, e^{i\vec{Q} \cdot \vec{R}_j} \right| I_n \right\rangle \right|^2 \delta(\hbar(\omega - \omega_F + \omega_I)) \tag{3.7}$$

where $f_j(Q)$ is the atomic form factor of the jth atom with position vector $\vec{R}_j$, while the suffix "n" refers to the nuclear states. Now the sum extends over all the atoms of the system. Assuming that all the scattering units in the system are equal, this expression can be further simplified by the factorization of the form factor. In the limit $Q \to 0$, $f(Q)$ is equal to the number of electrons in the atom. For increasing values of Q the form factor decays almost exponentially, with a decay constant determined by the radial distribution of the electrons in the atomic shells of the considered atom. Using the Van Hove pair correlation function defined in eq.2.4, $S(Q, \omega)$ can be formally written as [53]:

$$S(\vec{Q},\omega) = \frac{1}{2\pi N}\int_{-\infty}^{+\infty} e^{i\omega t}\langle\sum_{jk} e^{i\vec{Q}\cdot\vec{R}_j(t)}e^{-i\vec{Q}\cdot\vec{R}_k(0)}\rangle dt \tag{3.8}$$

where N is the number of particles in the system. Combining eqs.3.8 and 3.7 one obtains:

$$\frac{\partial^2\sigma}{\partial\Omega\partial\omega_f} = r_0^2(\frac{k_f}{k_i})(\hat{\epsilon}_f\cdot\hat{\epsilon}_i)^2|f(Q)|^2 S(\vec{Q},\omega) \tag{3.9}$$

This derivation is strictly valid for monatomic systems, but it can be easily generalized to molecular systems with several atomic species by replacing the atomic form factor with the molecular one. In the case of non-crystalline samples with different atoms the procedure to determine the scattering cross section is more complicated. Nevertheless the factorization of the form factor is still possible. The formalism introduced here is still valid if we assume that the cross section splits into two components: a coherent and an incoherent term. The latter is associated with fluctuations of the form factor while the former is proportional, through the mean value of the form factor, to $S(\vec{Q},\omega)$:

$$\frac{\partial^2\sigma}{\partial\Omega\partial\omega_f} = r_0^2(\frac{k_f}{k_i})(\hat{\epsilon}_f\cdot\hat{\epsilon}_i)^2[\langle f(Q)\rangle^2 S(\vec{Q},\omega) + \langle\delta f(Q)^2\rangle S_s(\vec{Q},\omega)] \tag{3.10}$$

Here $\langle f(Q)\rangle^2$ is the average value of the form factor over the whole system, while $\langle\delta f(Q)^2\rangle$ is the average of its fluctuation. The incoherent part of the cross section is related to $S_s(Q,\omega)$ which (see section 2.4) describes the single particle dynamics rather than the collective one.

Besides the cross-section, the realization of an IXS experiment requires also the knowledge of the scattering signal. In order to derive the actual count rate, absorption processes have to be considered. The number of photons (N) that are scattered into the solid angle ($d\Omega$) and in the frequency interval ($d\omega$) per unit time is given by [54]:

$$N = N_0\frac{\partial^2\sigma}{\partial\Omega\partial\omega}d\Omega d\omega\rho L e^{-\mu L} \tag{3.11}$$

where N_0 is the number of incident photons per seconds, ρ is the density of the scattering sample, L is its length along the scattering path and μ is the total absorption coefficient. The maximum IXS signal is achieved for $L = 1/\mu$, and consequently $N \propto 1/\mu$. Considering X-ray energies of $\approx 20\ KeV$ and $Z > 3$, μ is almost completely determined by the photoelectric absorption process. In this process $\mu \propto Z^4$, with important modifications at energies close to the photon absorption edges. Consequently, the scattering volume of high Z materials is very much reduced, while, on the other hand, the cross section increases as Z^2. Fig.2 reports the effective scattering intensity for an IXS experiment as a function of Z for a sample with optimum thickness and an incident photon energy of 17.8 KeV.

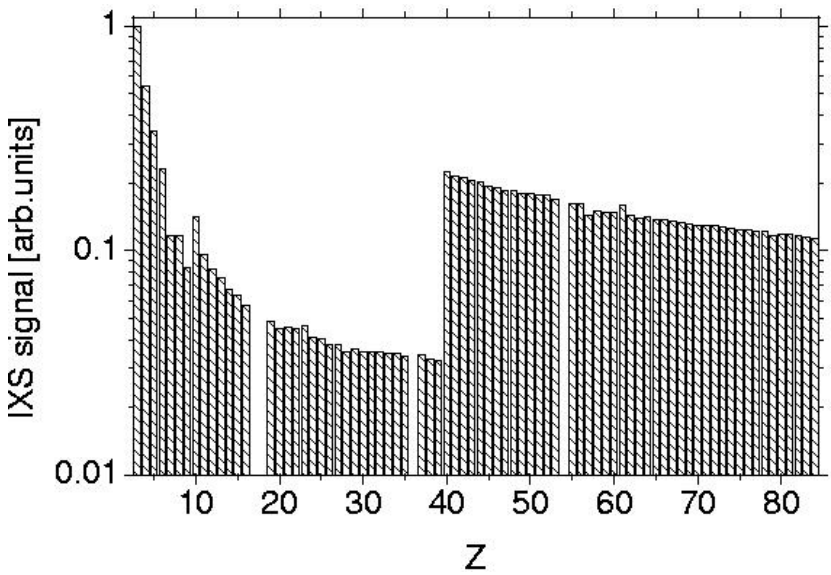

Figure 3.2: *Relative IXS signal as a function of the atomic number Z at the photon energy of 17.8 KeV, in the small Q-limit (i.e. $f(Q) = Z$), for an optimum sample thickness ($L = 1/\mu$). The large discontinuity between $Z = 39$ and $Z = 40$ is due to the K absorption edge of Zirconium.*

3.2 Dynamic structure factor and phonons

In this paragraph it is shown how the dynamic structure factor is directly linked to the quanta of the vibrational field: the phonons [53]. The simplest case is represented by an ideal Bravais lattice with only one atom per unit cell. Being $\vec{u}_j(t)$ the atomic displacement of atom j with respect to its lattice equilibrium position, $\vec{R}_j$, its instantaneous position, $\vec{R}_j(t)$, can be expressed as follows:

$$\vec{R}_j(t) = \vec{R}_j + \vec{u}_j(t) \tag{3.12}$$

The dynamic structure factor (eq.3.8) reads:

$$S(Q,\omega) = \frac{1}{2\pi N}\sum_{j,k} e^{i\vec{Q}\cdot(\vec{R}_j-\vec{R}_k)}\int_{-\infty}^{+\infty} e^{i\omega t}\langle e^{-i\vec{Q}\cdot\vec{u}_k(0)}e^{i\vec{Q}\cdot\vec{u}_j(t)}\rangle dt \tag{3.13}$$

In the framework of the second quantization the displacement is given by [53]:

$$\vec{u}_j(t) = \sqrt{\frac{1}{2MN}}\sum_{s,\vec{q}}\frac{\hat{\epsilon}_{s,\vec{q}}}{\sqrt{\omega_s(\vec{q})}}[ae^{i(\vec{q}\cdot\vec{R}_j-\omega_s(\vec{q})t)} + a^+e^{-i(\vec{q}\cdot\vec{R}_j-\omega_s(\vec{q})t)}] \tag{3.14}$$

here the suffix "s" indicates the cartesian indexes and a and a^* are the annihilation and creation phonon operators, respectively. $\vec{q}$ and $\omega_s(\vec{q})$ represent the phonon momentum and frequency, while $\hat{\epsilon}_{s,\vec{q}}$ is the phonon polarization. Exploiting the commutation rules of a and a^+, and some general relations, eq. 3.13 becomes [53]:

$$S(\vec{Q},\omega) = \frac{1}{2\pi N}\sum_j e^{i\vec{Q}\cdot\vec{R}_j - 2W(Q)} \int_{-\infty}^{+\infty} e^{-i\omega t} e^{\langle(\vec{Q}\cdot\vec{u}_0(0))(\vec{Q}\cdot\vec{u}_j(t))\rangle} dt \tag{3.15}$$

Where the quantity $e^{-2W(Q)} = e^{-\langle(Q\cdot u_i(0))^2\rangle}$ is usually called the Debye-Waller factor. Since we are dealing with small displacements, the argument of the integral can be expanded as [53]:

$$e^{\langle(\vec{Q}\cdot\vec{u}_0(0))(\vec{Q}\cdot\vec{u}_j(t))\rangle} = 1 + \langle(\vec{Q}\cdot\vec{u}_0(0))(\vec{Q}\cdot\vec{u}_j(t))\rangle + ... \tag{3.16}$$

The first term leads to elastic Bragg scattering, while the second one represents the inelastic scattering with the creation or annihilation of one phonon. Higher order terms can be omitted since only small momentum transfers, compared to the inverse of the typical atomic displacements, are considered. Within this approximation the dynamic structure factor can be expressed as:

$$\begin{aligned} S(Q,\omega) &= \frac{1}{4\pi MN} e^{-W(Q)} \sum_j e^{i\vec{Q}\cdot\vec{R}_j} \frac{(\vec{Q}\cdot\hat{\epsilon}_{s,\vec{q}})^2}{\omega_s(\vec{q})} \int_{-\infty}^{+\infty} e^{i\omega t}[e^{-i(\vec{q}\cdot R_j - \omega_s(\vec{q})t)}\langle n_q + 1\rangle \\ &+ e^{-i(\vec{q}\cdot R_j + \omega_s(\vec{q})t)}\langle n_q\rangle]dt \end{aligned} \tag{3.17}$$

where $\langle n_q\rangle$ represents the Bose occupation number of the excited phonon mode. For crystals with more than one atom per unit cell, the unit cell form factor has to be taken into account in the calculation of the one phonon process scattering cross section. For disordered systems the lack of translational periodicity makes the treatment more complicated, because the eigenvectors depend also on the equilibrium positions of the atoms [55, 56, 57]. As a consequence it is impossible to factorize the term $e^{i\vec{Q}\cdot(\vec{R}_j - \vec{R}_k)}$, as in eq.3.13.

3.3 X-rays or Neutrons?

The other experimental technique able to measure the $S(Q,\omega)$ at wavelengths comparable to intermolecular distances and energies comparable to the ones of collective excitations is Inelastic Neutron Scattering (INS). Neutrons directly couple to the nuclei through the Fermi pseudo-potential. Moreover, they have a spin of 1/2, and therefore the magnetic interaction with matter is non negligible. The double differential cross section for neutrons reads [53]:

$$\frac{\partial^2\sigma}{\partial\Omega\partial\omega_f} = (\frac{k_f}{k_i})[|\langle b\rangle|^2 S(\vec{Q},\omega) + (|\langle b\rangle|^2 - \langle|b|^2\rangle)S_s(\vec{Q},\omega)] \tag{3.18}$$

where b is the neutron scattering length. Comparing this equation with the equivalent for IXS (eq.3.10), it can be noticed that they are identical, once $f(Q)$ is replaced by b. The difference between these two quantities arises from the fact that $f(Q)$ is the expression of a (photon-electron) electromagnetic interaction, while b results from a purely (neutron-nuclei) nuclear interaction. For this reason X-rays are scattered

by different materials according to the number of electrons (Z) of the atomic species ($f(Q) \propto Z$). On the other hand, b depends on Z, A (the atomic number) and $\vec{J}$, the total (electron + nuclear) magnetic moment. The resulting scattering strength can therefore be very different for different isotopes of the same material, but also for the same isotope with a different orientation of its total magnetic moment. This "sensitivity" can produce very strong deviations of the actual scattering length with respect to its average value, thus leading to a significant contribution of the incoherent term ($\propto |\langle b \rangle|^2 - \langle |b|^2 \rangle$) in the neutron cross section.

On the other hand, neutrons present an enormous advantage. Neutrons with a De Broglie wavelength of $\sim \mathring{A}$ have energies of $\sim 10 \div 100\ meV$, the same order of magnitude as typical inelastic excitations. A moderate ($\sim 10^{-2}$) instrumental resolution in energy ($\Delta E/E$) and momentum ($\Delta Q/Q$) is therefore sufficient to determine the $S(Q,\omega)$ in the $\mathring{A}^{-1}$ and meV range. In contrast to this, X-rays with wavelengths of a few $\mathring{A}$ have energies of some KeV. A much higher instrumental energy resolution ($\Delta E/E \sim 10^{-7}$) is then needed in order to resolve the same excitations. This leads to an important reduction of the photon flux.

Another important difference between IXS and INS concerns the accessible dynamical range. The dynamical range consists of the set of (Q,E) values for which the scattering process is allowed. For neutrons it can be derived by using the general conservation laws (eq.3.1) and the quantum mechanical relation between energy and momentum:

$$E = \frac{\hbar^2 |\vec{k}|^2}{2M_n} \tag{3.19}$$

where M_n is the neutron mass. The equation that defines the dynamical range for neutrons is then:

$$\frac{|\vec{Q}|^2}{|\vec{k_i}|^2} = 2 - \frac{2M_n E}{\hbar^2 |\vec{k_i}|^2} + 2cos(2\theta)\sqrt{1 - \frac{2M_n E}{\hbar^2 |\vec{k_i}|^2}} \tag{3.20}$$

This equation can be considered as the equivalent of eq.3.2 for X-rays. It is evident that the momentum transfer, $\vec{Q}$, is not only determined by the scattering angle, but also by the energy transfer. Plotting eq.3.20 in the (Q,E)-plane, a set of curves, corresponding to different 2θ values, can be derived. The points lying on these curves are the only ones that can satisfy the energy and momentum conservation laws. In the left panel of fig.3.3 the typical dynamical range for thermal (300 K) neutrons ($k_i = 35$ nm^{-1} and $E_i = 25.8\ meV$) is reported. In the right panel of the same figure the equivalent quantity for X-rays employed in the present study ($k_i = 110\ nm^{-1}$ and $E_i = 21.747\ KeV$) is depicted. In both panels typical values for sound-like excitations are reported as straight lines. Inspecting fig.3.3 it is clear that X-rays can measure high energy excitations even at low-Q (notice the factor 20 between the two energy scales). The limitations imposed by the dynamical range are of primary importance in the study of amorphous systems, such as glasses or fluids, where the lack of translational periodicity does not allow the definition of Brillouin zones. As a consequence, the experiment has to be performed at small momentum transfer, at Q-values below the

first diffraction peak. In these cases, the energy of neutrons has to be increased in order to enlarge the dynamical range, at the expense of the energy resolution.

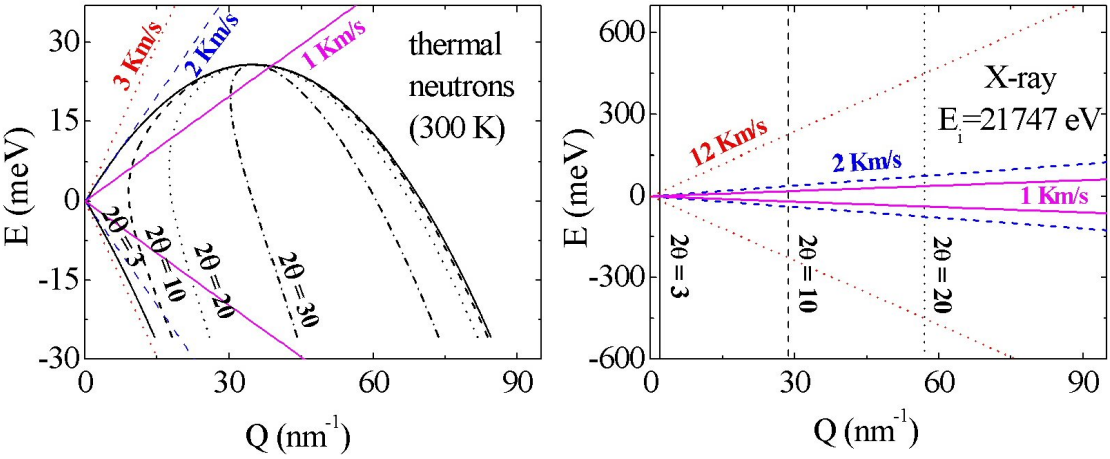

Figure 3.3: *Dynamical range for neutrons (left panel) and photons (right panel). Typical values for sound-like excitations, propagating with the velocity indicated in the respective panels, are plotted as straight lines.*

Finally, another important difference between the two techniques regards the shape of the instrumental energy resolution function. For INS this shape is Gaussian, while for IXS it is close to a Lorentian. The high tails of the Lorentian shape represent a big disadvantage for resolving the fine details of the $S(Q, \omega)$, in particular, for low energy features the contrast is much reduced with respect to the most favorable Gaussian shape of the INS resolution function. Other differences between IXS and INS are listed in table 3.1.

In conclusion the main advantages/disadvantages in using IXS rather than INS to study liquid systems are the following:

- In some cases, using INS, it is impossible to separate the coherent and incoherent contributions.
- X-rays are not limited by kinematic constraints (dynamical range). They can probe high values of energy transfer even at small momentum transfer.
- IXS presents a Q-resolution higher than INS.
- The Gaussian shape of the INS resolution function considerably enhances the contrast for low energy excitations.

In the last decade, the complementarity of IXS was successfully employed in the study of the collective dynamics in those cases where INS is difficult to apply (kinematic limitations, large incoherent scattering, multiple scattering, very high momentum resolution, or small samples).

IXS	INS
no correlation between momentum and energy transfer	strong correlation between momentum and energy transfer
$\Delta E/E \sim 10^{-7} \div 10^{-8}$	$\Delta E/E \sim 10^{-1} \div 10^{-2}$
$\partial^2\sigma/\partial\Omega\partial E_f \sim r_0^2 Z^2$ (for small Q)	$\partial^2\sigma/\partial\Omega\partial E_f \sim b^2$
strong photoelectric absorption $\Rightarrow$ no multiple scattering	weak absorption $\Rightarrow$ multiple scattering
negligible incoherent scattering	incoherent scattering
insensitive to magnetic excitations	study of magnetic excitations
small beam size: 100 μm or smaller	large beam size: $\sim cm$
small beam divergence: $\sim mrad$	large beam divergence: $\sim rad$
Lorentian shape of resolution function ($1 \div 8$ meV, FWHM)	Gaussian shape of resolution function ($0.5 \div 5$ meV, FWHM)
Q resolution ~ 0.1 nm^{-1}	Q resolution ~ 1 nm^{-1}
"infinite" dynamical range	limited dynamical range

Table 3.1: *Main characteristic of IXS and INS instruments.*

3.4 IXS spectrometer: beamline ID-28 at ESRF

In this section the IXS beamline ID-28 at the European Synchrotron Radiation Facility (ESRF) in Grenoble [58] is briefly described. The instrument layout is reported in fig.3.4.

The instrumental concept is based on a triple axis spectrometer [53]. The first axis is the one of the monochromator crystal. Its role is to determine the energy, $\hbar\omega_i$, of the incident photons. The second axis is located at the sample position, and determines the momentum transfer. The third axis is the analyzer crystal, its role is the determination of the scattered photon energy, $\hbar\omega_f$. The ID28 beamline is equipped with 5 analyzer systems which allow the collection of 5 different IXS spectra, corresponding to 5 different transfer momenta, at the same time.

The X-ray source consists of three undulators of 32 mm magnetic period, placed in a straight high-β section of the electron storage ring. The utilized X-ray radiation energies correspond to the undulator emission of the 3rd or 5th harmonics. The X-ray beam from the undulator's odd-harmonics has an angular divergence of approximately 40×15 μRad (FWHM, horizontal $\times$ vertical), a spectral bandwidth $\Delta E/E \sim 10^{-2}$, and an integrated power within this divergence in the order of 200 W.

The X-ray beam from the undulators is pre-monochromatized to $\Delta E/E \sim 2 \cdot 10^{-4}$ using a silicon, $Si(1,1,1)$, channel-cut crystal kept in vacuum and cooled by liquid nitrogen. The main role of the pre-monochromator is to reduce the heat load impinging on the main monochromator. This is mandatory in order to keep the thermal deformation of the silicon crystal below the limits for which the energy resolution is deteriorated.

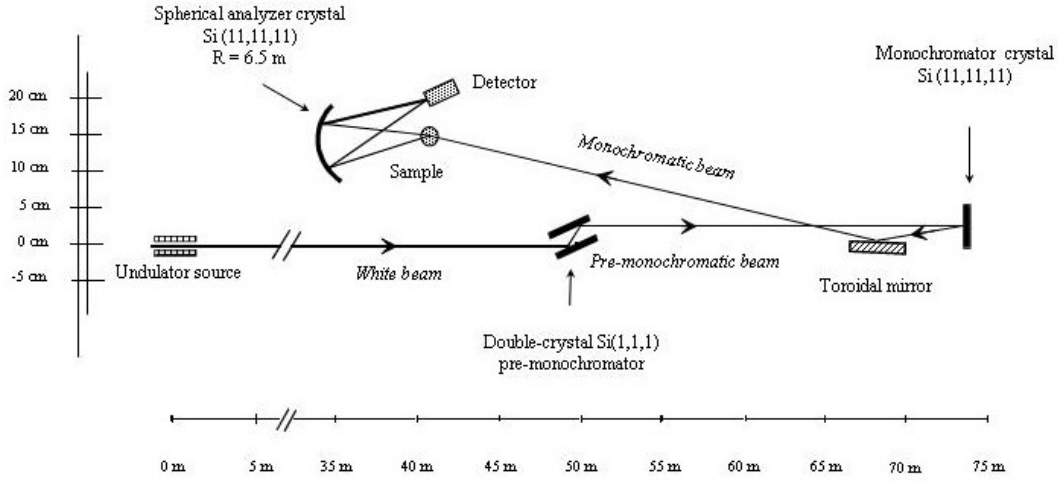

Figure 3.4: *Layout of the IXS beamline ID-28 at the European Synchrotron Radiation Facility.*

The X-ray photons from the pre-monochromator impinge onto the high energy resolution backscattering monochromator, consisting of an asymmetrically cut silicon crystal oriented along the [111] direction, operating at a Bragg angle of 89.98^o. This extreme backscattering geometry insures the minimization of geometrical contributions to the total energy resolution. The spectral angular acceptance, the so-called Darwin width, is larger than the X-ray beam divergence, and, therefore, all the photons within the desired energy bandwidth are transmitted. High order Bragg reflections and perfect crystals are required in order to obtain the necessary energy resolution of $\Delta E/E \sim 10^{-7} \div 10^{-8}$; these reflections are the silicon (h, h, h), with $h = 7, 8, 9, 11, 12, 13$ [59].

The monochromatic beam is focused in the horizontal and vertical plane by a platinum coated toroidal mirror, located at 25 m from the sample. This scheme provides a focus at the sample position of $250 \times 80\ \mu m^2$ FWHM. More performing optics are available at ID28 to focus the beam down to $30 \times 40\ \mu m^2$.

The scattered radiation is subsequently analyzed in energy. Although the problems connected to the energy resolution are conceptually the same for the monochromator and for the analyzer, the required angular acceptance is very different. The monochromator can be realized using a flat perfect crystal. For the analyzer crystal the optimal angular acceptance is dictated by the desired momentum resolution. Considering values of ΔQ in the range of $0.1 \div 0.5\ nm^{-1}$, the corresponding angular acceptance of the analyzer crystal must be ~ 10 mrad or higher, a value much larger than the Darwin width. The only way to obtain such a large angular acceptance is the use of a focusing system, which, nevertheless, has to preserve the single crystal perfection necessary to obtain the desired energy resolution. This constraint automatically excludes the possibility to consider elastically bent crystals. A solution consists of laying a large number of undistorted perfect flat crystals on a spherical surface, with the aim to use a 1:1 pseudo-Rowland circle geometry with aberrations kept such that the desired energy resolution is not degraded. These analyzers consist of 12000 perfect silicon single

crystals of surface size $0.6 \times 0.6\ mm^2$ and a thickness of 3 mm, glued on a spherical substrate of a radius equal to the length of the spectrometer arm [60, 61].

The spectrometer furthermore consists of an entrance pinhole, motorized slits in front of the analyzer crystal to set the desired momentum resolution, and a detector with its corresponding pinhole. The detectors are Peltier cooled silicon diodes of 1.5 mm thickness with an active area of $2 \times 12\ mm^2$, inclined at 20° in order to enhance the X-ray absorption. They have a very low dark count ($\sim$ 1 count in 30 minutes). On ID-28 there are five independent analyzer systems with a fixed angular offset among themselves of $\sim 1.5^o$, mounted on a 7 m long arm that can rotate around a vertical axis passing through the scattering sample from 0° to 55°. This allows the recording of 5 IXS spectra at the same time, with a nearly constant Q-offset, corresponding to a momentum transfer range between 1 and 100 nm^{-1} in the $Si(11, 11, 11)$ configuration.

Differently from traditional triple axis spectrometers, and as a consequence of the extreme backscattering geometry, the energy difference between analyzer and monochromator cannot be varied modifying the Bragg angle of one of the two crystals. The energy scans are therefore performed by changing the relative temperature, ΔT, of the monochromator. This induces a relative variation of the lattice parameters, $\Delta d/d = \alpha(T)\Delta T$, and therefore a relative variation of the diffracted energy, $\Delta E/E = -\Delta d/d$, is induced as well. Considering for the thermal expansion coefficient, α, a value of $\sim 2.58 \cdot 10^{-6} K^{-1}$ at room temperature, the required energy resolution of $10^{-7} \sim 10^{-8}$ implies an accuracy in temperature control of the monochromator crystal in the mK-range. This task is achieved by a carefully designed temperature bath, controlled by an active feedback system [59], which assures a temperature control with a precision of 0.2 mK in the temperature region around 295 K. In order to convert the temperature scale into the energy scale, the most recent result for $\alpha(T)$ has been considered [62]:

$$\alpha(T) = \alpha_0 + \beta\Delta T \tag{3.21}$$

where $\alpha_0 = 2.581 \pm 0.002 \cdot 10^{-6}\ K^{-1}$, $\beta = 0.016 \pm 0.004 \cdot 10^{-6}\ K^{-2}$, $\Delta T = T - T_0$, where $T_0 = 22.5\ ^oC$. From eq.3.21 one can precisely calculate the temperature variations of lattice constants:

$$\Delta d/d_0 = \int_{T_0}^{T} \alpha_0 + \beta(T' - T_0)dT' = (\alpha_0 - \beta T_0)\Delta T + \frac{1}{2}\beta(T^2 - T_0^2) \tag{3.22}$$

Finally, the variation of the diffracted energy, $\Delta E/E = -\Delta d/d$, is easily found.

Figure 3.5 shows the instrumental response function of one of the five analyzers, corresponding to an energy resolution of 1.6 meV, when operating at the $Si(11, 11, 11)$ reflection . It has been recorded by measuring the scattering from a disordered sample (Plexiglas) at a temperature of 10 K and at a Q-transfer corresponding to the first maximum of its static structure factor (10 nm^{-1}). In this way the elastic contribution to the scattering is maximized. Table 3.2 summarizes the main characteristics of the spectrometer.

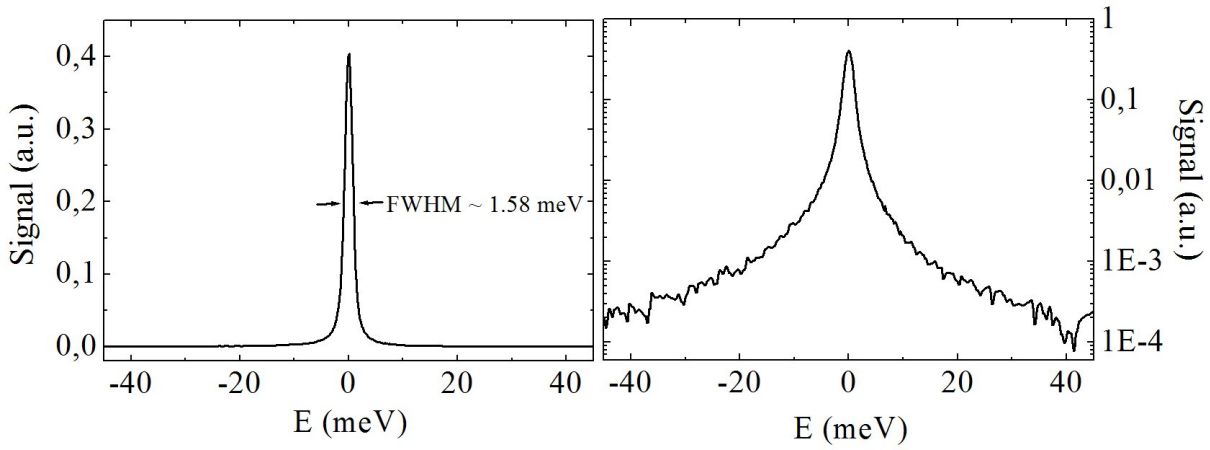

Figure 3.5: *Measured instrumental resolution function, corresponding to the* $Si(11, 11, 11)$ *configuration of the spectrometer, plotted both in linear (left panel) and logarithmic (right panel) scale*

h	Energy $[keV]$	ΔE $[meV]$	Q_{max} $[nm^{-1}]$	Q_{min} $[nm^{-1}]$	ΔQ $[nm^{-1}]$	Flux [photons/s/200mA]
7	13.840	7.6 ± 0.2	64	1	1.89	$1.5 \cdot 10^{11}$
8	15.817	5.5 ± 0.2	74	1	2.16	$9.0 \cdot 10^{10}$
9	17.794	3.0 ± 0.2	83	1	2.43	$2.7 \cdot 10^{10}$
11	21.747	1.5 ± 0.1	101	1	3.00	$6.6 \cdot 10^{9}$
12	23.725	1.3 ± 0.1	111	1	3.24	$5.9 \cdot 10^{9}$
13	25.704	1.0 ± 0.1	120	1	3.50	$1.5 \cdot 10^{9}$

Table 3.2: *Main characteristics of the ID-28 spectrometer, for the different* $Si(h, h, h)$ *reflections. Energy indicates the incident photon energy,* ΔE *is the total energy resolution,* Q_{min} *and* Q_{max} *indicate the minimum and maximum momentum transfers and* ΔQ *indicates the Q-spacing between adjacent analyzers. The photon flux values are measured at the sample position.*

3.5 Experimental apparatus

In this section the large volume pressure cells (LVC) utilized in the present thesis are described. The choice of these cells was motivated by two main reasons:

- LVC's are very versatile since, even if they cannot reach very high pressures, they can work at low and high temperature. LVC's are well suited for the present study since the critical temperature of the investigated samples is very different, while the critical pressure is always quite low.
- LVC's allow the optimization of the sample volume (or more precisely the sample length) in order to maximize the IXS signal[1].

It has to be noticed that the effective sample length is in any case limited by the depth of field of the spectrometer. This is given by $d/sin(2\theta)$, where d is the size of the detector pinhole ($\sim 2\ mm$ in this case). As a consequence, even if a longer cell is employed, for $\theta > 6$ degree the effective sample length does not exceed $\sim 10\ mm$. The employed cells are depicted in fig.3.6.

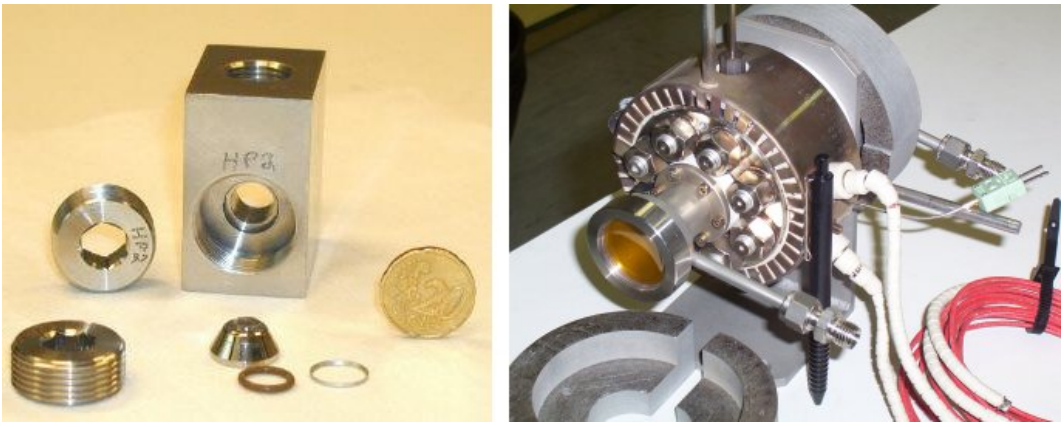

Figure 3.6: *Cunsolo cell (left panel) and the HP cell used for the study of supercritical water and ammonia (right panel).*

3.5.1 The Cunsolo cell

This LVC cell, also referred to as "Cunsolo cell", was used both in the low temperature cryogenic set-up (study of neon and nitrogen) and, with slight modifications, at high temperature (study of liquid water). The technical drawing of this cell is reported in fig.3.7. Its main characteristics are the long sample length (10 mm) and the angular acceptance of 30 degrees, which allows reaching exchanged momenta up to 50 nm^{-1} in the $Si(11, 11, 11)$ configuration. The cell can be connected to the external HP apparatus through a standard Nova Swiss HP connection [63].

[1]The ideal sample length for the investigated samples is $\sim 10 \div 30\ mm$.

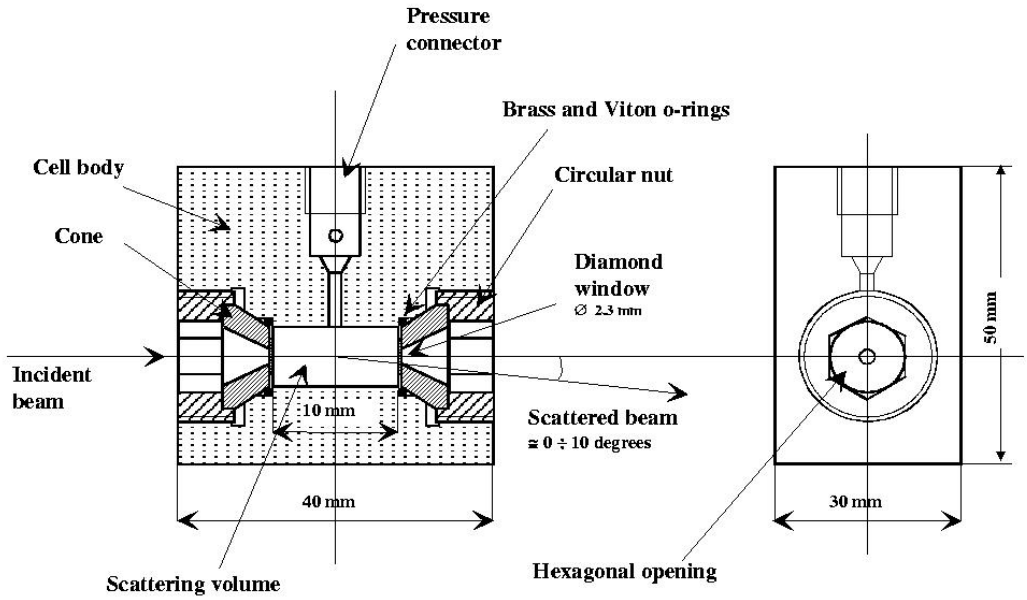

Figure 3.7: *Schematic drawing of the Cunsolo cell.*

The HP sealing of this cell is reported in fig.3.8. The two diamond windows, through which pass both the incident and the scattered beam, are single crystal diamond disks of 6 mm diameter and 1mm thickness. Besides their resistance to mechanical solicitations, a decisive advantage in using diamond windows is their negligible contribution to the scattered intensity. Diamonds are glued on the flat internal face of the two conical supports. The choice of the appropriate glue and the gluing procedure itself must be done with care. For the low temperature studies an epoxy resin (Epotech 301 [64]) was used as glue. Both the window and the glued surface have been previously mirror-polished, $< 5\ \mu m$ roughness (rms), with diamond powder. The diameter of the hole (2.3 mm) at the flat surface of the support, which allows the beam to pass through the chamber, was chosen as the best compromise between the angular opening and the unsupported area of the windows. The supports are screwed and tightened against the cell body by special circular nuts. Two brass or copper ring gaskets with triangular section are pushed, by the pressure medium itself, as an anvil into the inner space between the conical surface of the supports and the inner wall of the internal chamber. The HP tightness is accomplished by this double metal to metal contact (conical supports and internal chamber). The two gaskets were coated with indium in order to improve the tightness. A couple of viton O-rings were used together to seal the cell at low pressure. In fact, while at high pressures the compression medium itself pushed the metallic gasket ensuring the tightness, the O-rings are used as a spring, which pushes the gaskets from the back, allowing the tightness also at low pressure.

The utilized HP generator was a Nova-Swiss (550.0400-2) hand pump, whose maximum output pressure is 7 $Kbar$ [63]. This hand pump was located outside the experimental hutch and connected to the HP cell trough a long capillary. In this way the pressure could be changed without entering the experimental hutch. Moreover,

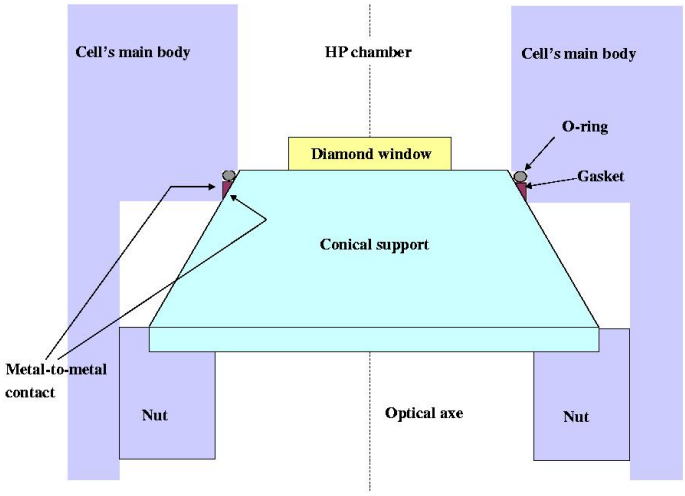

Figure 3.8: *Schematic draw of HP sealing.*

pressure valves to eventually decouple the HP generator from the HP cell were used. The pressure was controlled by two pressure gauges with a precision of ± 20 bar at 3 $Kbar$ [63]. Prior to use, the whole system was carefully cleaned by compressed air flushing. The HP line was then closed and evacuated by a vacuum pump. Finally, the sample was loaded into the HP apparatus. The whole system was located in a vacuum chamber. Two windows, made out of 50 μm thickness mylar foils, allowed the passage of incident and scattered X-ray beams. Finally, all the assembly was mounted on the goniometry of the sample stage of the ID-28 spectrometer, in order to precisely position the cell in the beam.

3.5.2 Low temperature assembly for neon and nitrogen

For the study of Neon and Nitrogen, whose critical temperatures are well below room temperature, the pressure cell was mounted in thermal contact with a cold finger of an AL125 close-cycle helium cryostat [65]. This system allows exploring a wide region of the $P - T$ plane: from ~ 20 K up to room temperature, and from a few bar up to $\sim$ 5 $Kbar$.

Thin indium foils were used for all thermal interfaces in order to maximize the thermal contact. The temperature of the cell was changed by using a heating resistor placed between the pressure cell and the cryostat cold finger. The temperature is monitored by two silicon diodes mounted on the cell, with a precision of $\pm$ 0.5 K. The pressure cell and the cryostat cold finger are kept under high vacuum ($\sim 10^{-8}$ $mbar$). The weight of the assembly, schematically reported in fig.3.9, was roughly 25 Kg.

3.5.3 High temperature assembly for water

The previously described experimental set-up is not suited for high temperatures. In particular all the tested glues deteriorate at temperatures higher than 500 K leading

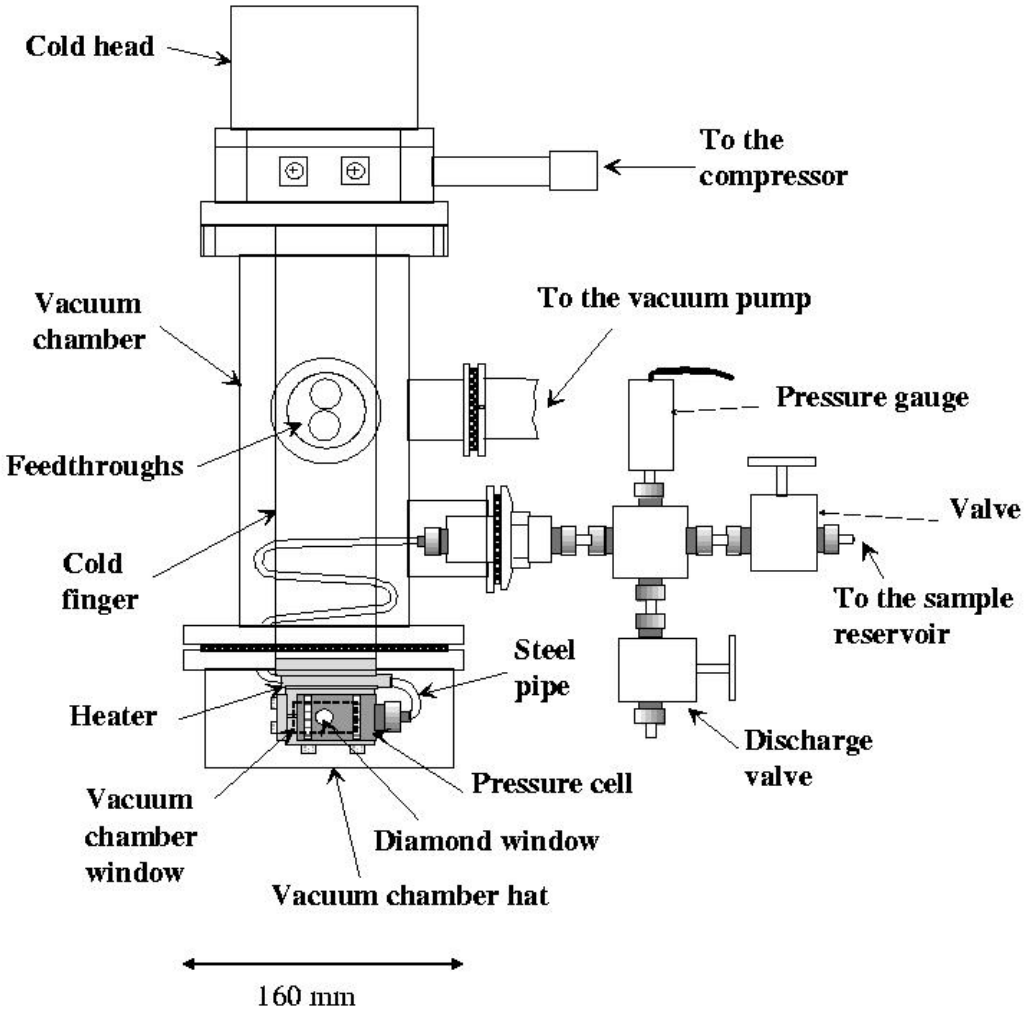

Figure 3.9: *Low temperature HP apparatus employed in the study of Neon and Nitrogen.*

to a leak of the HP sealing after some hours. Moreover, neither indium coated gaskets nor viton O-rings can be used because of their low melting point.

In order to circumvent these difficulties, the glue was replaced by a dry contact between diamonds and conical supports, after a very careful polishing of the contact surfaces. The sealing was ensured by the higher pressure at the edge of the cone's holes with respect to the pressure exserted on the supported part of the diamond windows. This produces a pressure gradient between the central (unsupported area) and the side (supported area) part of the diamond window. Three screws were used to hold the diamonds in the correct place before applying pressure. Furthermore, the indium coated gaskets and viton O-rings were replaced by equivalent elements entirely made out of copper. These improvements permitted to increase the maximum achievable temperature up to $\sim 700\ K$.

The cell is heated up by means of a resistive heating wire inserted between two steel plates, kept in thermal contact with the external surfaces of the cell. The whole set-up is maintained in vacuum ($\sim 10^{-2}\ mbar$) in order to avoid both temperature gradients and air scattering. The temperature is measured by a type-K thermocouple in thermal contact with the main body of the cell. The pressure and temperature stability were better than 10 bar and 1 K.

3.5.4 Set-up for ammonia and supercritical water

In the case of supercritical water, a strong oxidation of gaskets, cone surfaces and main body of the cell was observed. This phenomenon is most likely due to the extremely high oxidation ability of supercritical water. In order to study water in its supercritical phase, a custom-made commercial HP cell (Ref.: 1670.0000, N° 1192) was employed [66]. This cell has been especially designed to resist oxidation and corrosion. Its HP sealing consists of a Bridgman metal-to-metal contact, involving a gold wire of 0.125 mm thickness. The sample length was 10 mm, while the maximum accessible angle was 20° (corresponding to a maximum momentum transfer of 35 nm^{-1}). The cell's working temperatures and pressures are: $270 \div 800\ K$ and $0 \div 1.2\ Kbar$. This cell does not need a vacuum chamber because two vacuum paths ($\sim 10^{-2}\ mbar$) are placed in front and behind the entrance and exit optical windows. The cell can be connected to an external HP apparatus by standard Top-Industry connectors [66]. Outside the main body of the cell there are both a resistive heater and a cooling system based on a compressed air circulation. The temperature can be measured by a thermocouple placed near the sample in the main body of the HP cell. The whole set-up is embedded in an insulating envelope.

This cell was as well used in the study of liquid and supercritical ammonia. Since ammonia is a highly corrosive, flammable and toxic material, a phase separator was needed in order to decouple the pressure cell and the external HP apparatus. This phase separator is a custom-made commercial equipment (Ref.: 1720.000, N° 1210) [66]. It consists of two rigidly coupled pistons which can slide inside a cylinder. The area of one piston (HP side) is smaller than the other (LP side), the ratio between these areas (~ 3) provides an enhancement of the pressure in the HP side, with respect to the LP one, by the same factor.

The HP side of the phase separator is specially designed to be compatible with ammonia, and, moreover, it can be cooled down to 220 K by a closed alcohol circulation.

The loading of ammonia in the cell was performed as follows: after air flushing and evacuation of the whole HP line (cell, HP side of phase separator, valves and fittings), the cell was isolated from the phase separator by a valve. The HP side of the phase separator was then cooled down to 220 K, and the gaseous ammonia was loaded inside. At 220 K ammonia liquifies at very low pressures, consequently the HP side of the phase separator was completely filled with liquid ammonia. Finally, after removing the ammonia bottle, the valve between the cell and the phase separator was opened and the liquid ammonia filled the whole HP line. At this stage the pressure in the HP side could be changed by controlling the pressure on the LP side. This was done by simply connecting a N_2 bottle with a pressure regulator directly to the input of the LP side.

The general performances of the described set-ups are reported in table 3.3.

	Cunsolo Cell low-T set-up	Cunsolo Cell high-T set-up	Commercial cell (Top-Industry)
Θ_M (degree)	30	30	20
P_m (bar)	1	50	0
P_M (bar)	5000	3000	1200
T_m (K)	10	290	270
T_M (K)	300	700	800

Table 3.3: *Main characteristics of the utilized experimental apparatuses: angular acceptance, Θ_M, minimum/maximum pressure, $P_{m/M}$, and minimum/maximum temperature, $T_{m/M}$.*

Résumé du chapitre 4

Ce chapitre est consacré à la description des expériences effectuées. Dans la première section la planification des expériences est discutée, l'accent est donné au choix des échantillons et des états thermodynamiques. En outre, le traitement de données et la stratégie d'analyse des données, en particulier concernant la procédure de "fit", sont présentés. Les résultats expérimentaux obtenus par l'analyse de facteur de structure dynamique et statique sont discutés. Ces résultats concernent les relations de dispersion des modes acoustiques longitudinaux, ainsi que les processus de relaxation utilisés pour décrire la dynamique du système.

Chapter 4

Experimental results

In this chapter the performed experiments, the data analysis strategy and the obtained results are discussed. The main characteristic of the present study is its systematic nature. As a consequence, the choice of the samples, the thermodynamic path and the data analysis strategy were oriented in this direction.

4.1 Choice of the samples and thermodynamic path

A first consideration concerns the temperature difference between the triple and the critical point. In fact, the liquid phase roughly ranges between these two points, and, if they are separated by only a few K, a reliable study as a function of temperature becomes impracticable. Furthermore, the critical point has to be located in a range accessible to the employed sample environment. Some examples of critical parameters for different substances are shown in table 4.1; the studied ones are indicated in bold.

	ρ_c (Kg/m^3)	P_c (bar)	T_c (K)	T_t (K)	Z	ρ_l $(mole/m^3)$
H_2	30	13.15	33.2	13.8	2	38000
He	70	2.27	5.2	2.18	2	36500
Ne	**480**	**26.8**	**44.5**	**24.6**	**10**	**62000**
Ar	540	48.6	151	83.8	18	35500
$\mathbf{N_2}$	**313**	**34**	**126.2**	**63.2**	**14**	**31000**
CO_2	468	73.8	304	216.6	22	27000
$\mathbf{NH_3}$	**225**	**113.3**	**405**	**195.6**	**10**	**43000**
$\mathbf{H_2O}$	**322**	**221**	**647**	**273.16**	**10**	**55500**
Rb	345	160	2090	319	37	17500
Hg	5700	1520	1750	234	80	68000

Table 4.1: *Critical densities* (ρ_c)*, pressures* (P_c) *and temperatures* (T_c) *of various substances. The respective triple point temperature* (T_t)*, atomic number* (Z) *and "typical" molar densities of the liquid phase* (ρ_l)*, are also reported.*

Another consideration for the choice of the samples is the availability of their Equation of State (EoS). The EoS is essential for the following analysis, since it provides the values of the thermal diffusivity and the specific heat ratio, which are kept as fixed values in the model function. Moreover, the EoS allows the comparison of the sound velocity and viscosity, obtained from the analysis of the IXS spectra, with their thermodynamic counterparts. Finally, samples with simple molecular structures and high scientific and interdisciplinary relevance were preferred. In view of the above considerations neon (Ne), nitrogen (N_2), ammonia (NH_3) and water (H_2O) were chosen.

These systems have similar molecular dimensions and masses; conversely, their intermolecular interactions are very different. Neon can be considered as the prototype of a simple and weakly interacting monatomic liquid. The nitrogen molecules are as well weakly interacting, but the molecular structure (diatomic) is more complex than the one of neon. Water is the classic example of an H-bonded liquid. Ammonia is as well an H-bonded liquid, but it does not show the well known thermodynamic anomalies of water [67].

In order to investigate both the liquid and the supercritical phase, the temperature must be varied above and below the critical one. Experimentally, this can be achieved in several ways. The most common ones are the following:

- At constant density: pressure is increased on heating the sample, in order to keep the density constant.
- Along the coexistence line: the liquid sample is confined in a closed vessel in equilibrium with its vapor. If the initial amount of material in the vessel is correct, on heating, the sample moves along the coexistence line up to the critical point.
- At constant pressure: the density is decreased such that the pressure is kept constant on heating.

Owing to technical constraints the first option is not allowed with the employed HP apparatus. The second option presents another problem: the thermodynamic states along the coexistence line, close to the critical point, have an extremely low sound velocity. As a consequence, the characteristic energies of inelastic excitations are very small and impossible to resolve with the available instrument. Furthermore, the divergence of thermodynamic parameters close to the critical point makes IXS spectra impossible to analyze[1]. In conclusion, the third option was chosen. In this way, one can study both the density and temperature dependence of IXS spectra.

In order to perform a more significant comparison between the various investigated systems, the natural choice is to employ the law of corresponding states, enounced in chapter 1. In other words, the thermodynamic states of different samples should overlap in the (T/T_c,ρ/ρ_c)-plane. Unfortunately, in several cases, the pressures needed to obtain the same ρ/ρ_c, at the same T/T_c, for different samples were too high (or too

[1]For instance the specific heat ratio, γ, diverges and therefore the intensity of Brillouin peaks -which is $\propto \gamma^{-1}$- tends to zero.

low) for the experimental apparatus. Therefore the explored thermodynamic states are only partially overlapped in the (T/T_c,ρ/ρ_c)-plane (see fig.4.1).

The investigated thermodynamic states, together with the values of some relevant thermodynamic quantities are reported in tables 4.1 to 4.4. In the case of neon, the last two thermodynamic points have been chosen because they are corresponding states of the other investigated systems.

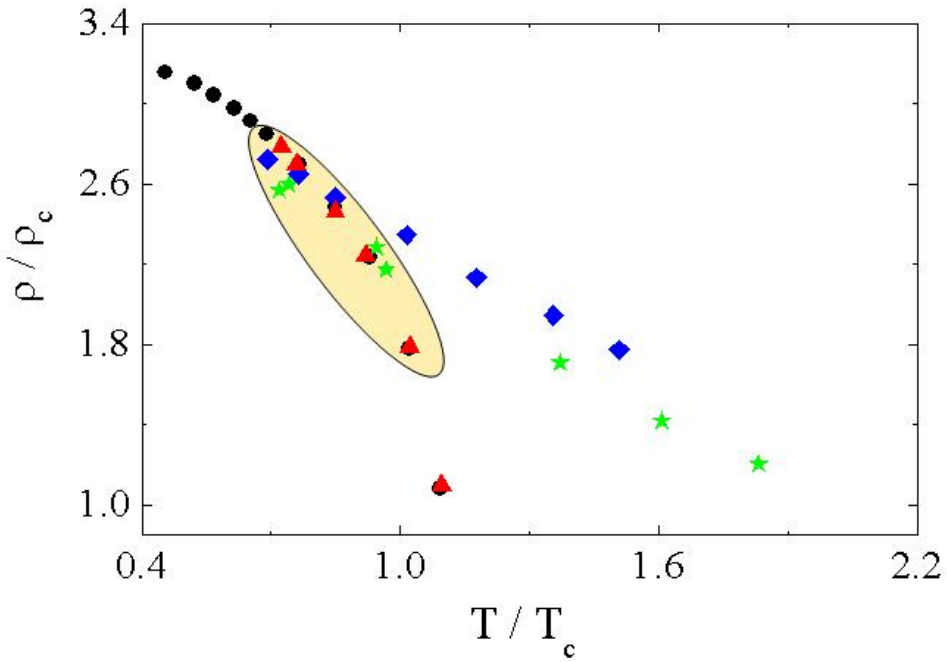

Figure 4.1: *Investigated thermodynamic states in reduced units of temperature and density: Water (black circles), Ammonia (red triangles), Nitrogen (blue diamonds) and Neon (green stars). The shaded area highlights the common corresponding state.*

P (bar)	T (K)	ρ (Kg/m^3)	c_s (m/s)	γ	D_T (cm^2/s)	ν_s (cm^2/s)
200 (7.46)	32 (0.72)	1232 (2.57)	688.8	1.96	7.74×10^4	9.5×10^4
200 (7.46)	42 (0.94)	1097 (2.29)	571.2	2.22	6.04×10^4	6.2×10^4
200 (7.46)	61 (1.37)	819.4 (1.71)	421.6	2.67	4.4×10^4	4.27×10^4
200 (7.46)	71.5 (1.61)	681.7 (1.42)	378.3	2.62	4.5×10^4	4×10^4
200 (7.46)	81.5 (1.83)	578.6 (1.21)	359.9	2.47	5×10^4	4.16×10^4
230 (8.58)	103 (2.31)	483.1 (1.01)	375	2.17	5.6×10^4	4.8×10^4
280 (10.4)	38 (0.85)	1192 (2.49)	671	1.98	8.1×10^4	9.8×10^4
150 (5.6)	43 (0.97)	1043 (2.17)	514.1	2.41	5.3×10^4	5.6×10^4

Table 4.2: *Relevant properties of the investigated thermodynamic states of neon: pressure, temperature and density (the corresponding values in reduced units are reported in brackets), adiabatic sound velocity, c_s, specific heat ratio, γ, thermal diffusivity, D_T, and kinematic shear viscosity, ν_s.*

P (bar)	T (K)	ρ (Kg/m^3)	c_s (m/s)	γ	D_T (cm^2/s)	ν_s (cm^2/s)
400 (11.8)	87 (0.72)	852.4 (2.7)	1043	1.62	10.9×10^4	23.2×10^4
400 (11.8)	96 (0.94)	827.9 (2.6)	1000	1.67	10.5×10^4	19.2×10^4
400 (11.8)	107 (1.37)	792.7 (2.5)	934	1.72	9.9×10^4	15.6×10^4
400 (11.8)	128 (1.61)	734.2 (2.3)	843	1.78	9.2×10^4	12.1×10^4
400 (11.8)	148 (1.83)	667.3 (2.1)	740.5	1.86	8.3×10^4	10×10^4
400 (11.8)	171 (2.31)	609.9 (1.9)	677.2	1.88	8×10^4	8.8×10^4
400 (11.8)	190 (0.74)	555.3 (1.8)	623.8	1.89	7.8×10^4	8.2×10^4

Table 4.3: *Relevant properties of the investigated thermodynamic states of nitrogen.*

P (bar)	T (K)	ρ (Kg/m^3)	c_s (m/s)	γ	D_T (cm^2/s)	ν_s cm^2/s
220 (1.94)	293 (0.72)	627.3 (2.79)	1508	1.63	18.7×10^4	24.7×10^4
220 (1.94)	308 (0.76)	601.3 (2.67)	1414	1.67	17.6×10^4	22.4×10^4
220 (1.94)	344 (0.85)	554.7 (2.47)	1178	1.79	15×10^4	17.8×10^4
220 (1.94)	373 (0.92)	504.6 (2.24)	977	1.96	12.7×10^4	15.3×10^4
210 (1.85)	414 (1.02)	401.9 (1.79)	646.3	2.59	8.7×10^4	12.8×10^4
200 (1.77)	444 (1.09)	246.5 (1.1)	417.6	4.1	5.5×10^4	12.5×10^4

Table 4.4: *Relevant properties of the investigated thermodynamic states of ammonia.*

P (bar)	T (K)	ρ (Kg/m^3)	c_s (m/s)	γ	D_T (cm^2/s)	ν_s cm^2/s
400 (1.81)	293 (0.45)	1016 (3.15)	1548	1.01	14.9×10^4	98×10^4
400 (1.81)	337 (0.52)	998 (3.1)	1625	1.06	16.5×10^4	45×10^4
400 (1.81)	367 (0.57)	980 (3.04)	1628	1.1	17.2×10^4	31.8×10^4
400 (1.81)	398 (0.62)	958 (2.98)	1602	1.15	17.7×10^4	24.3×10^4
400 (1.81)	423 (0.65)	938 (2.91)	1565	1.2	18×10^4	20.5×10^4
400 (1.81)	447 (0.69)	917 (2.85)	1519	1.25	18.1×10^4	18×10^4
400 (1.81)	494 (0.76)	869 (2.7)	1400	1.36	17.9×10^4	15×10^4
400 (1.81)	549 (0.84)	800 (2.49)	1220	1.53	16.9×10^4	13.1×10^4
400 (1.81)	598 (0.93)	719 (2.23)	1013	1.77	14.9×10^4	12.1×10^4
400 (1.81)	660 (1.02)	573 (1.79)	707	2.55	10.5×10^4	11.7×10^4
400 (1.81)	706 (1.09)	348 (1.08)	495	4.32	6.32×10^4	12.8×10^4

Table 4.5: *Relevant properties of the investigated thermodynamic states of water.*

4.2 Data analysis

Experimental artifacts able to affect the IXS spectra mainly come from the windows of the vacuum chamber in which the cell is located. In order to avoid scattering from these windows, the following precautions have been taken (see fig.4.2):

i) The entrance window has been positioned as far as possible from the scattering center (i.e. from the sample), outside the depth of field of the spectrometer.

ii) Close to the exit window, an absorbing material (beam stop) was placed, in order to block the scattering from this window.

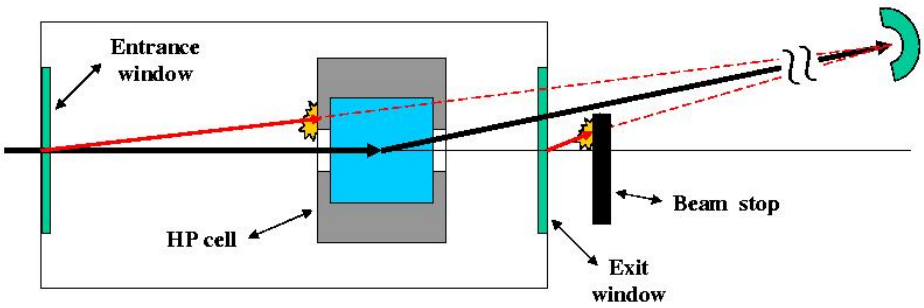

Figure 4.2: *Schematic illustration of the sample environment and the suppression of parasitic scattering.*

In order to quantify the scattering from the HP cell windows, empty cell measurements were performed. Some of them are reported in fig.4.3. This contribution is negligible compared to the signal from the sample (figs.4.4, 4.5, 4.6 and 4.7). Furthermore it has to be noticed that the intensity reported in fig.4.3 is overestimated, since

these spectra are not corrected for the absorption of the sample.

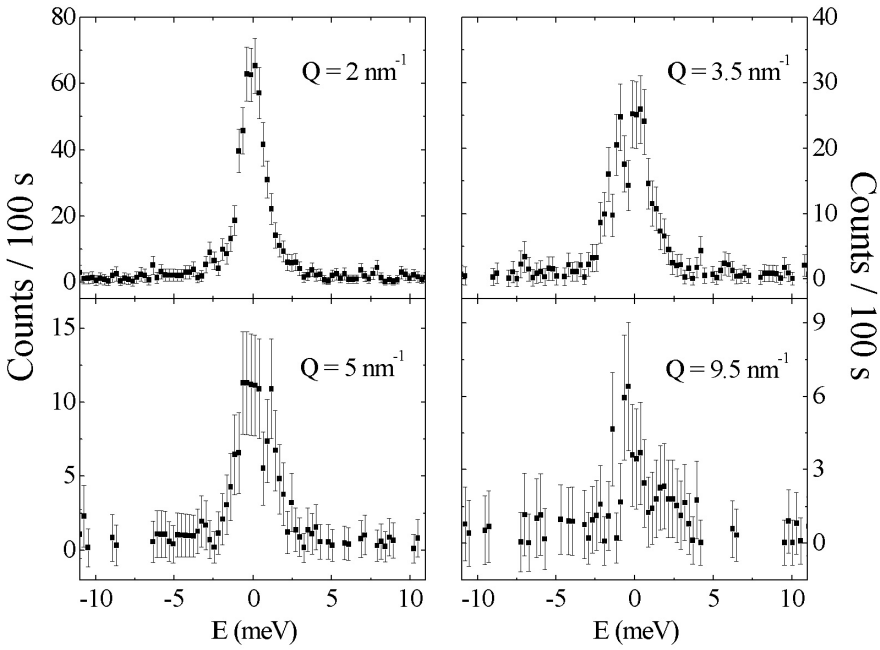

Figure 4.3: *Empty cell spectra at the Q-values indicated in the panels.*

4.2.1 Data treatment

The raw data, $I(Q,\omega)$, are related to the $S(Q,\omega)$ through the relation:

$$I(Q,\omega) = A[n(\omega,T)S(Q,\omega) \otimes R(\omega)] + B \tag{4.1}$$

where $R(\omega)$ is the experimental resolution function. The symbol $\otimes$ stands for numerical convolution, A is an overall intensity factor and B is a background term which takes into account both the electronic background of the detectors and the environmental one. Finally, $n(\omega,T)$ is the adimensional detailed balance factor:

$$n(\omega,T) = \frac{\hbar\omega/k_BT}{1-e^{-(\hbar\omega/k_BT)}} \tag{4.2}$$

The data analysis consists of a fitting procedure based on a standard minimization of the χ^2, which is defined as follows:

$$\chi^2 = \sum_{i=1}^{N} \frac{(I(Q,\omega_i)-y_i)^2}{\sigma_i^2} \tag{4.3}$$

where N is the number of data points in the IXS spectra, y_i are the measured counts corresponding to the channel having energy transfer $\hbar\Delta\omega_i$ centered around $\hbar\omega_i$, and σ_i

is the corresponding standard deviation. A Poisson statistics was assumed, and then $\sigma_i = \sqrt{y_i}$. The minimization was performed by the software MINUIT [68], employing two routines: a SIMPLEX minimization, and, if the correlation among the parameters was not too high, a successive refined search of the χ^2 minima using a gradient method (MIGRAD). The errors were calculated through the calculation of the Hessian and covariance matrixes (HESSE).

4.2.2 Model function

The theoretical model for the $S(Q,\omega)$ was derived in the framework of the memory function formalism, as discussed in chapter 2. In this framework the $S(Q,\omega)$ can be written as:

$$S(Q,\omega) = \frac{S(Q)}{\pi} \frac{(c_T(Q)Q)^2 m'_L(Q,\omega)}{[\omega^2 - (c_T(Q)Q)^2 - \omega m''_L(Q,\omega)]^2 + \omega^2 [m'_L(Q,\omega)]^2} \tag{4.4}$$

where $c_T(Q)$ is the Q-dependent isothermal sound velocity, which can be expressed in terms of the static structure factor, $S(Q)$, through the equation:

$$c_T(Q) = \sqrt{K_B T / M S(Q)} \tag{4.5}$$

and finally, $m'_L(Q,\omega)$ and $m''_L(Q,\omega)$ are, respectively, the real and imaginary part of the time Fourier transform of the memory function, $m(Q,t)$. The chosen expression for the memory function is (see section 2.4.5):

$$m_L(Q,t) = \Delta_T^2(Q) e^{-t/\tau_T(Q)} + \Delta_\alpha^2(Q) e^{-t/\tau_\alpha(Q)} + 2\Gamma_\mu(Q)\delta(t) \tag{4.6}$$

where $\tau_T(Q) = (\gamma(Q) D_T(Q) Q^2)^{-1}$, $\Delta_T^2(Q) = (\gamma(Q) - 1)(c_T(Q)Q)^2$ and $\Delta_\alpha^2(Q) = (c_\infty^2(Q) - \gamma(Q) c_T^2(Q)) Q^2$. $D_T(Q)$, $\gamma(Q)$, $\tau_\alpha(Q)$, $\Gamma_\mu(Q)$ and $c_\infty(Q)$ are the finite-Q generalizations of the thermal diffusivity, the specific heat ratio, the structural relaxation time, the intensity of the instantaneous relaxation and the infinite-frequency sound velocity, respectively. The Fourier transform of eq.4.6 yields:

$$m'_L(Q,\omega) = \Delta_T^2(Q) \frac{\tau_T(Q)}{1 + (\omega \tau_T(Q))^2} + \Delta_\alpha^2(Q) \frac{\tau_\alpha(Q)}{1 + (\omega \tau_\alpha(Q))^2} + \Gamma_\mu(Q) \tag{4.7}$$

$$\omega m''_L(Q,\omega) = \Delta_T^2(Q) \frac{(\omega \tau_T(Q))^2}{1 + (\omega \tau_T(Q))^2} + \Delta_\alpha^2(Q) \frac{(\omega \tau_\alpha(Q))^2}{1 + (\omega \tau_\alpha(Q))^2} \tag{4.8}$$

We conclude this section with two remarks. The first concerns the recent finding that a stretched exponential decay better describes the structural relaxation [69, 70]. In view of the fact that the quality of our data is not sufficient to distinguish which kind of time decay is more adapted to describe the structural relaxation, a simple exponential decay (that presents less free parameters) was preferred. The second remark concerns the presence of a second inelastic excitation in the $S(Q,\omega)$. This feature was noticed in liquid water in the $THz\text{-}nm^{-1}$ dynamical range, and its nature is still debated [41, 71, 72, 73, 74]. The intensity of this excitation is very small in the IXS spectra, and becomes negligible at high temperatures. For a few test cases, the inclusion of

this weak second excitation did not significantly alter the behavior of the other fitting parameters. The eventual presence of a second excitation was therefore ignored.

4.2.3 Fitting procedure

In order to reduce the correlation between the fitting parameters in eqs. 4.1, 4.4 and 4.6, some of them were kept fixed:

- the background, B, was fixed to the measured value. It was checked that small deviations around this value do not influence the other parameters.
- the temperature, T, was fixed to the measured value.
- the specific heat ratio, $\gamma(Q)$, and the thermal relaxation time, $\tau_T(Q)$, were fixed to the values obtained from the EoS. Their Q-dependence was neglected.

Neglecting the Q-dependence of $\gamma(Q)$ and $\tau_T(Q)$ could influence the results concerning the other parameters. However, this assumption was motivated by the lack of experimental or theoretical results for all the investigated systems in the explored thermodynamic range.

The parameters that have been kept free to vary in the fitting routines are therefore:

- the overall intensity factor, A.
- the Q-dependent generalization of the isothermal sound frequency, $\Omega_T(Q) = c_T(Q)Q$.
- the infinite-frequency sound frequency, $\Omega_\infty(Q) = c_\infty(Q)Q$, which, together with $\Omega_T(Q)$, determines the amplitude of the structural relaxation: $\Delta^2_\alpha(Q)$.
- the timescale of the structural relaxation, $\tau_\alpha(Q)$.
- the intensity of the instantaneous relaxation, $\Gamma_\mu(Q)$.

For $\tau_\alpha(Q)\Omega_L(Q) \ll 1$, the fits return values of $\Delta^2_\alpha(Q)$ and/or $\tau_\alpha(Q)$ consistent with zero. This means that the fully relaxed limit of the structural relaxation is reached (viscous regime), and the exponential decay related to the structural relaxation can be reasonably approximated by a $\delta(t)$-function. In these cases the exponential term in eq.4.6 was removed from the fitting routine, and the multiplicative factor of the $\delta(t)$ was redefined as follows:

$$2\Gamma_\mu(Q) + \tau_\alpha(Q)\Delta^2_\alpha(Q) \rightarrow 2\Gamma_L(Q) \tag{4.9}$$

where $\Gamma_L(Q)$ includes both the instantaneous and the structural contribution. As a consequence the number of free parameters decreases from 5 to 3, since $\Gamma_\mu(Q)$, $\Delta^2_\alpha(Q)$ and $\tau_\alpha(Q)$ are replaced by $\Gamma_L(Q)$.

Inspecting figs.4.4, 4.5, 4.6 and 4.7, one can notice the excellent agreement between the model function (red lines) and the experimental spectra (full circles) for all the

investigated systems in the whole explored range of pressure, temperature and Q. These representative IXS spectra show inelastic shoulders that produce a broadening of the lineshape with respect to the resolution function (blue lines). This broadening increases with Q, as can be seen from the spectra at fixed temperature[2]. In the bottom panels of these figures the temperature evolution of the IXS spectra at fixed Q is reported. The logarithmic scale emphasizes the excellent agreement between the fits and the experimental data, even in the high frequency spectral tails. It can be clearly seen that the spectra become more symmetric, intense and narrow with increasing temperature. These features are due to the detailed balance, the higher value of the $S(Q)$ at high temperatures and the lower sound velocity of supercritical samples, respectively. In the case of Neon, the resolution functions corresponding to the spectra at $Q = 8$, 12 and 13 nm^{-1} present a "bump" around 8 meV. This also reflects in the shape of the measured $S(Q, \omega)$; nevertheless the convolution process can very well take into account this feature (see the high-T spectra of fig.4.4).

4.2.4 Longitudinal current spectra

The other fundamental information that can be derived from the analysis of IXS spectra is the value of $\Omega_L(Q)$, the characteristic frequency of longitudinal modes. This quantity corresponds to the maximum of the longitudinal current spectrum, $J_l(Q, \omega)$. This spectrum cannot be directly measured, however, it can be derived from the $S(Q, \omega)$, using the following relation:

$$J_l(Q, \omega) = \frac{\omega^2}{Q^2} S(Q, \omega) \tag{4.10}$$

This equation is a direct consequence of the principle of mass conservation for a non relativistic fluid; it is strictly valid, since particles are not created and/or annihilated. Unfortunately, a direct calculation of $J_l(Q, \omega)$ from the raw data is impossible because of the Lorentian shape of the instrumental energy resolution function. Therefore $J_l(Q, \omega)$ was calculated numerically, using the model function described above and the parameters obtained from the fit. The maxima of these spectra were found to be weakly dependent on the numerical value of the fitting parameters, provided that the high frequency tails of the $S(Q, \omega)$ are well described. Representative longitudinal current spectra (corresponding to the $S(Q, \omega)$ reported in figs.4.4 - 4.7) are depicted in figs.4.8, 4.9, 4.10 and 4.11.

[2]Only the central part of these spectra has been shown in order to better underline the Q-evolution of the lineshape.

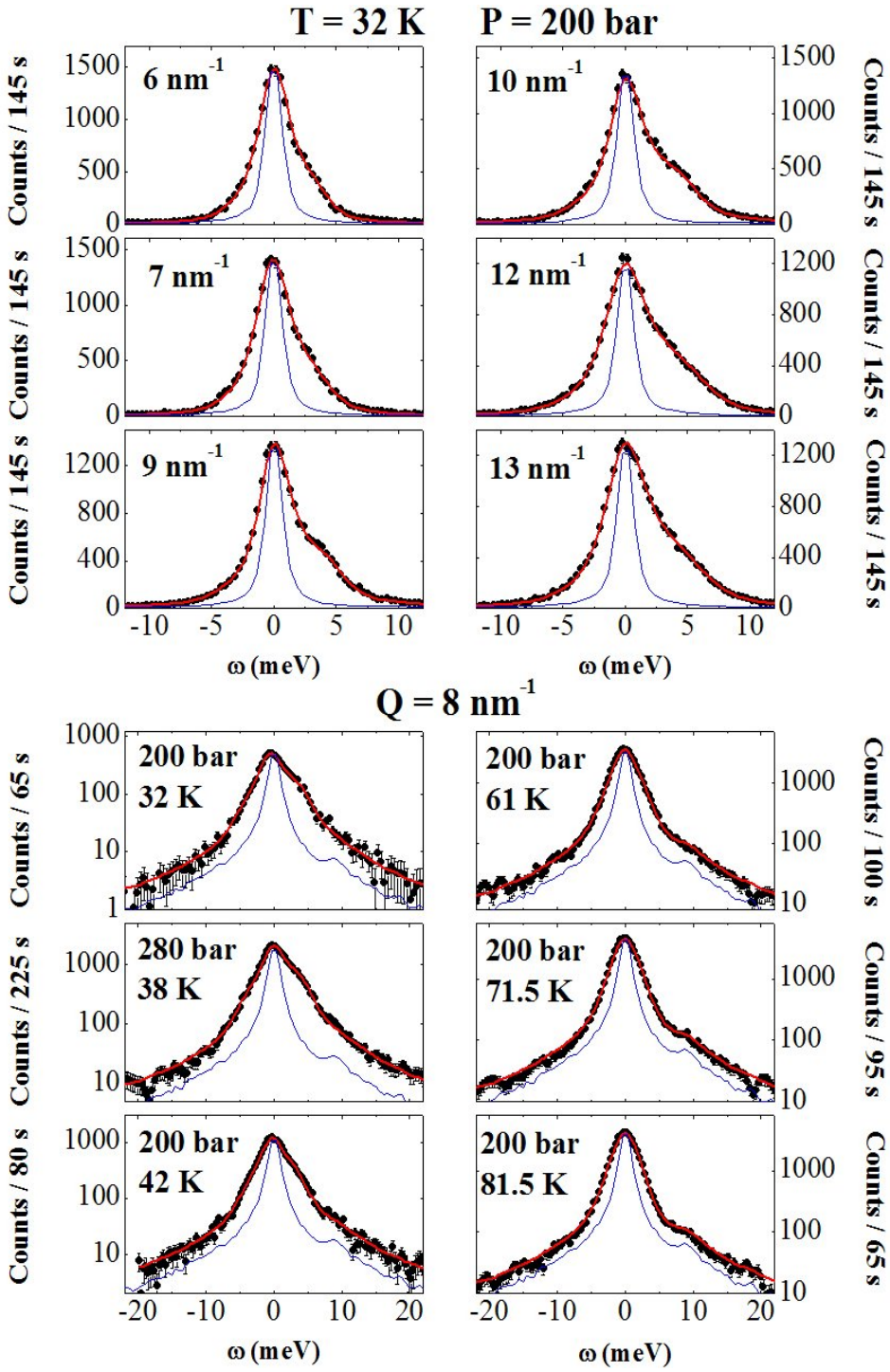

Figure 4.4: *Representative IXS spectra of neon (full circles) with their error bars at the indicated T, P, Q values. The corresponding best fit and the instrumental resolution function are represented by red and blue lines, respectively. Top panel: IXS spectra at $T = 32$ K and $P = 200$ bar as a function of Q, on a linear scale. Bottom panel: IXS spectra at $Q = 8$ nm^{-1} at the indicated P-T values, on a logarithmic scale.*

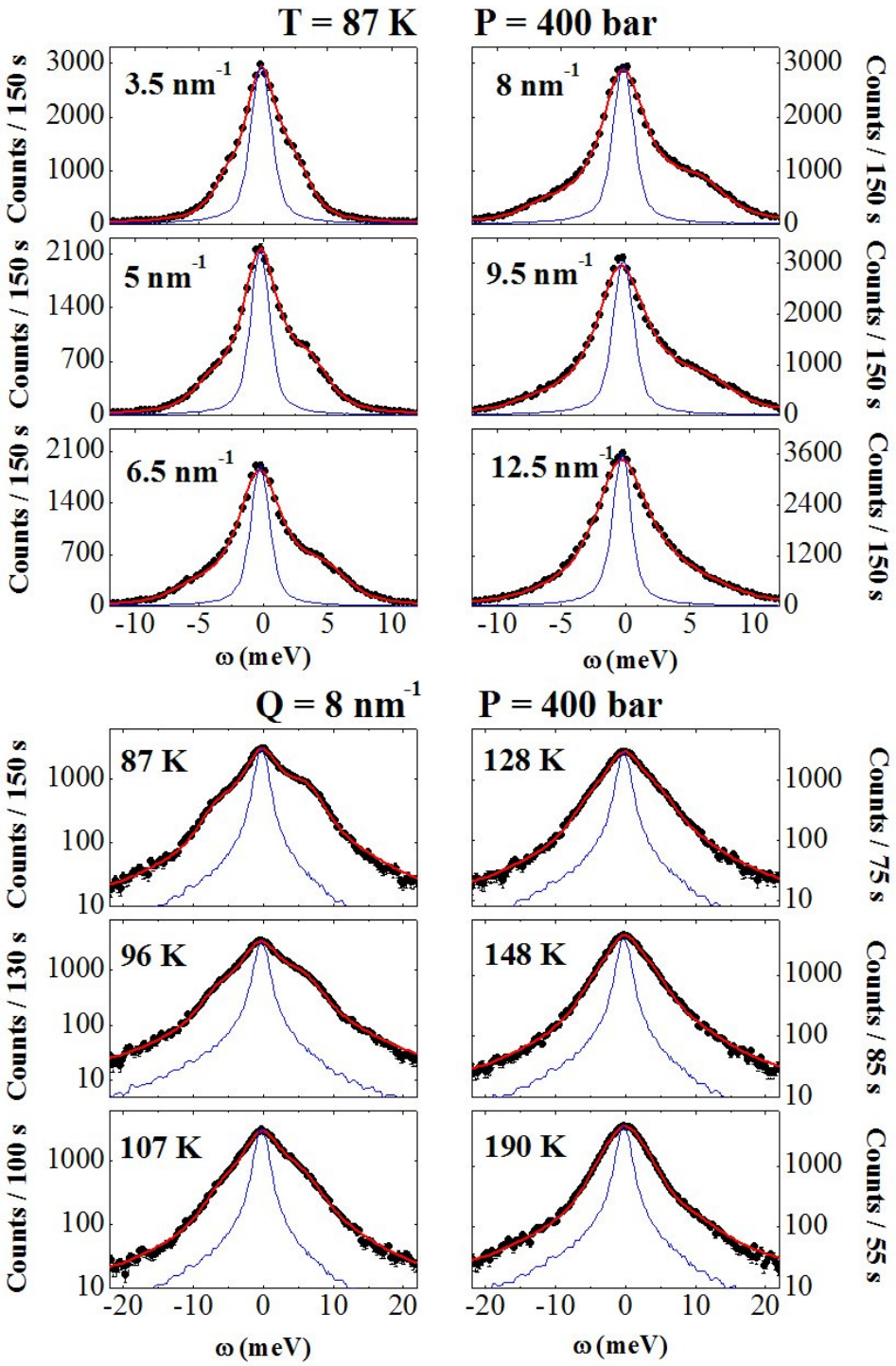

Figure 4.5: *Representative IXS spectra of nitrogen (full circles) with their error bars at the indicated T, P, Q values. The corresponding best fits and the instrumental resolution function are represented, respectively, by red and blue lines. Top panel: IXS spectra at $T = 87$ K and $P = 400$ bar as a function of Q, on a linear scale. Bottom panel: IXS spectra at $Q = 8$ nm^{-1} and $P = 400$ bar at the indicated temperatures, on a logarithmic scale.*

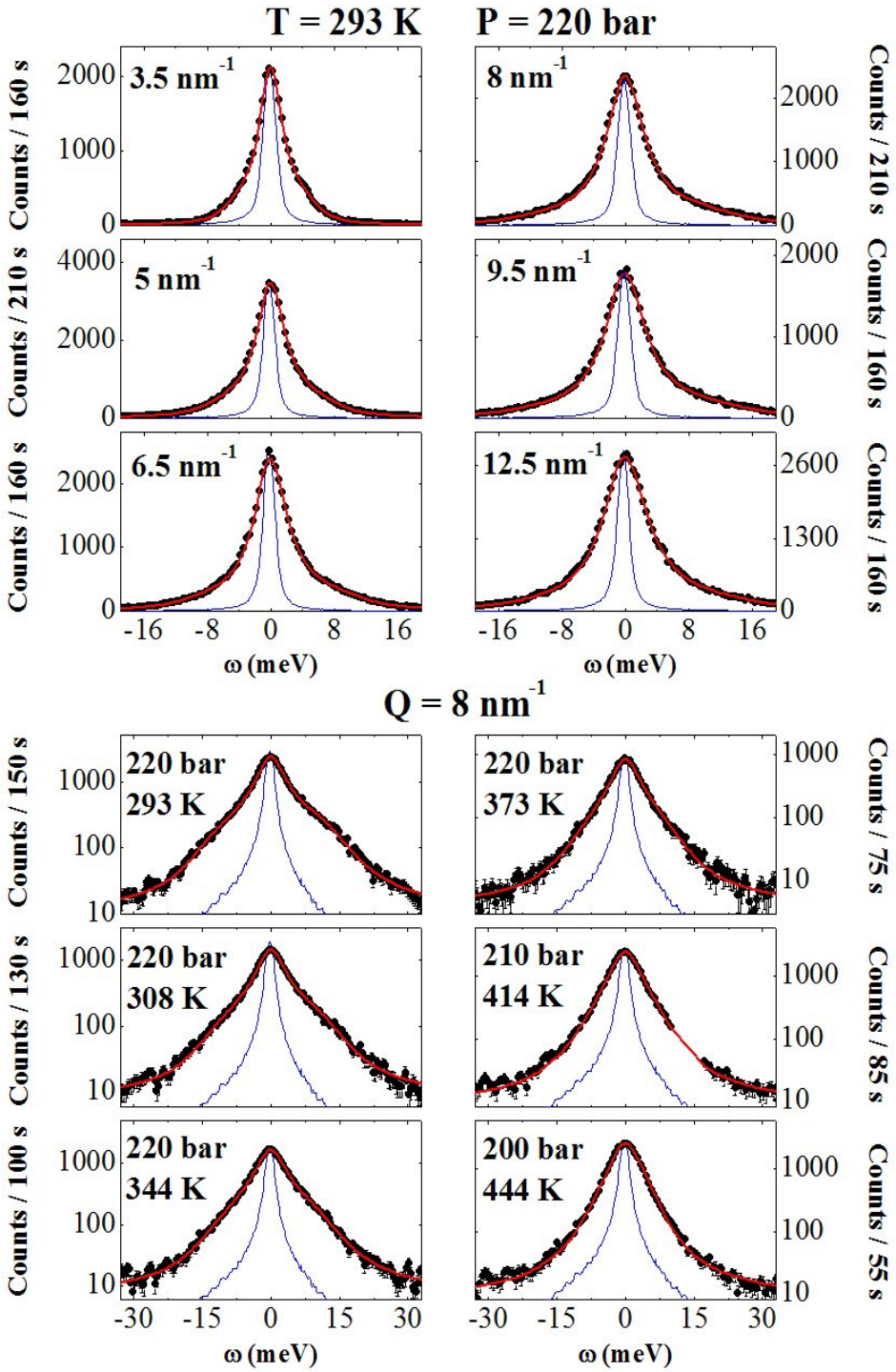

Figure 4.6: *Representative IXS spectra of ammonia (full circles) with their error bars at the indicated T, P, Q values. The corresponding best fits and the instrumental resolution function are represented, respectively, by red and blue lines. Top panel: IXS spectra at $T = 293\ K$ and $P = 220\ bar$ as a function of Q, on a linear scale. Bottom panel: IXS spectra at $Q = 8\ nm^{-1}$ at the indicated P-T values, on a logarithmic scale.*

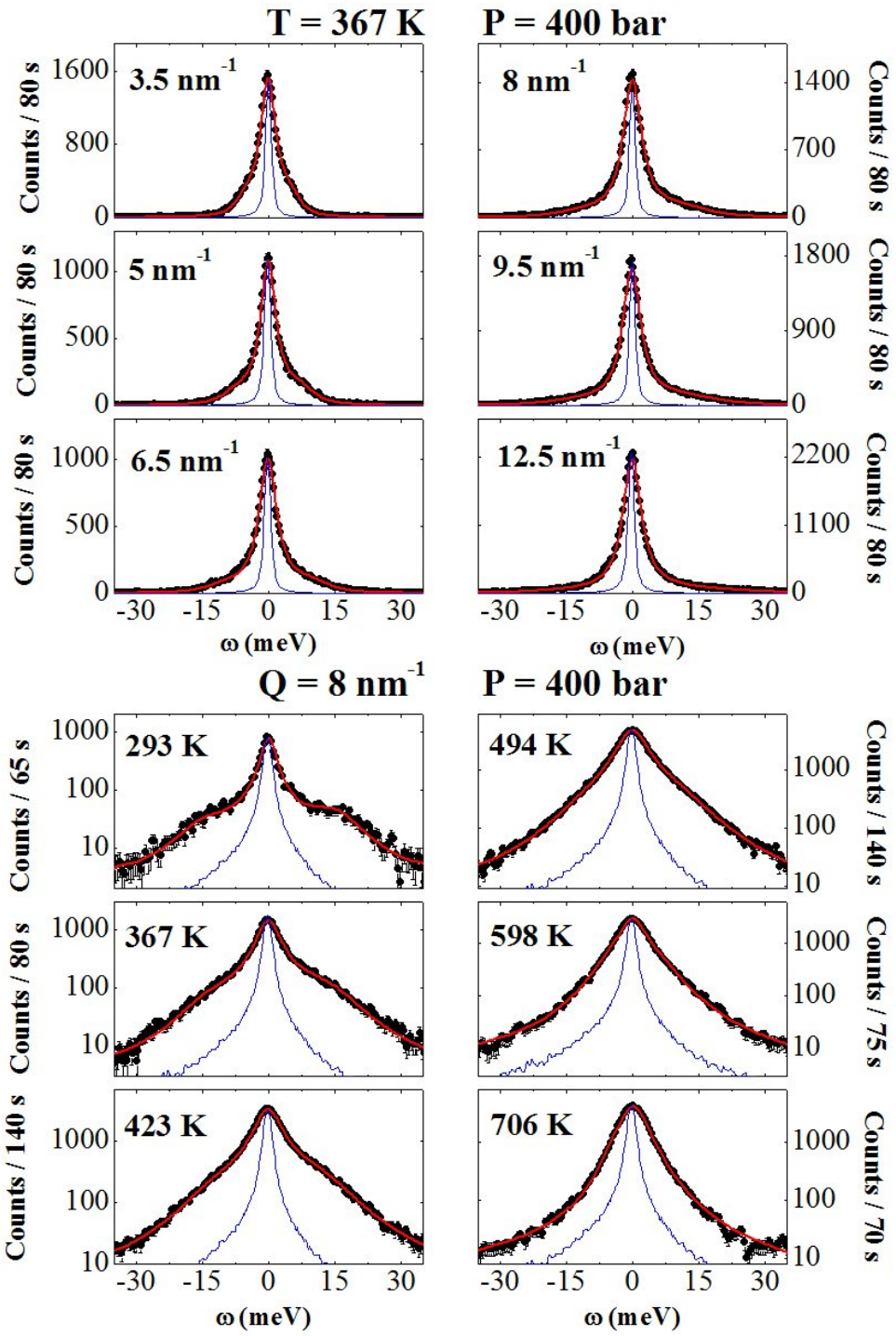

Figure 4.7: *Representative IXS spectra of water (full circles) with their error bars at the indicated T, P, Q values. The corresponding best fits and the instrumental resolution function are represented, respectively, by red and blue lines. Top panel: IXS spectra at $T = 367$ K and $P = 400$ bar as a function of Q, on a linear scale. Bottom panel: IXS spectra at $Q = 8$ nm^{-1} and $P = 400$ bar at the indicated temperatures, on a logarithmic scale.*

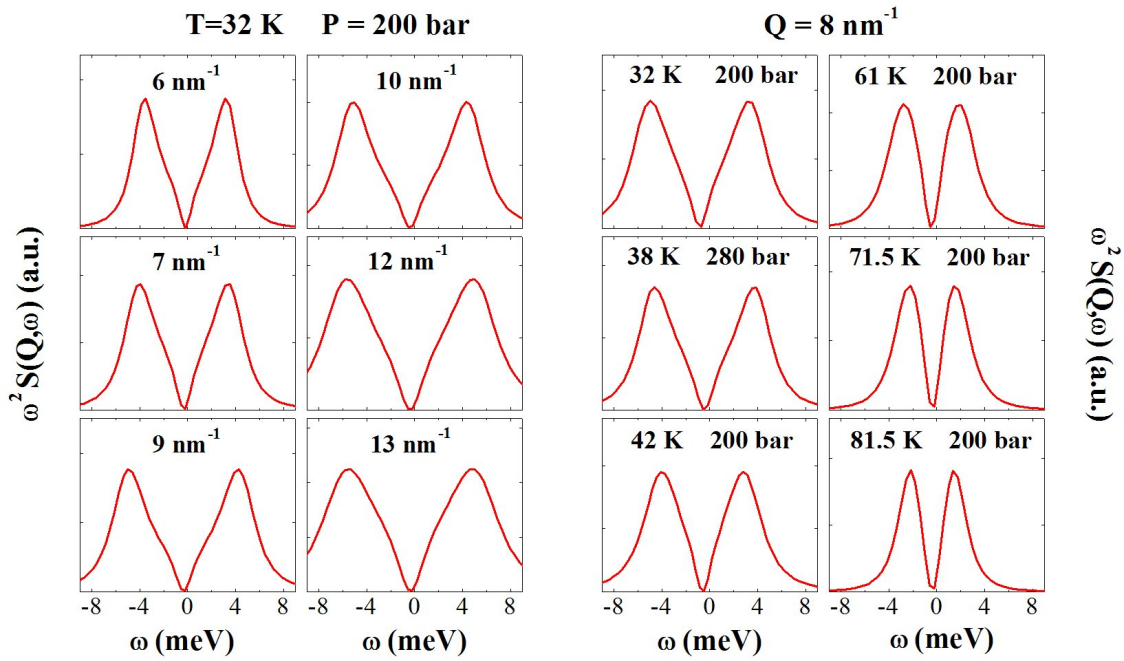

Figure 4.8: *Longitudinal current spectra corresponding to the IXS spectra of fig.4.4.*

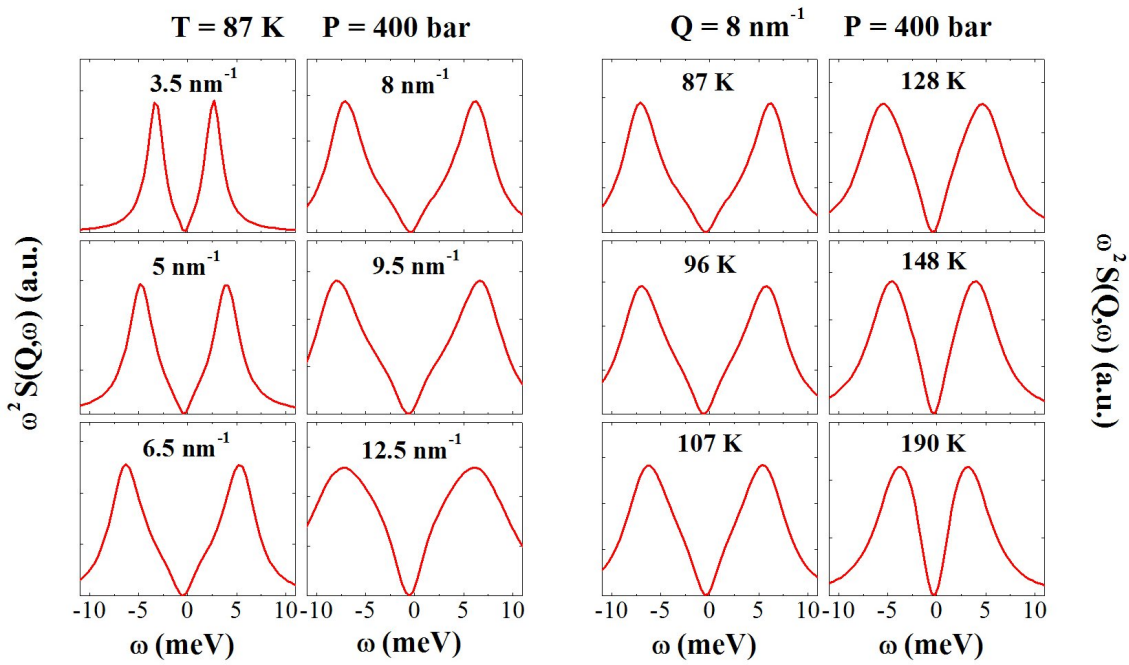

Figure 4.9: *Longitudinal current spectra corresponding to the IXS spectra of fig.4.5.*

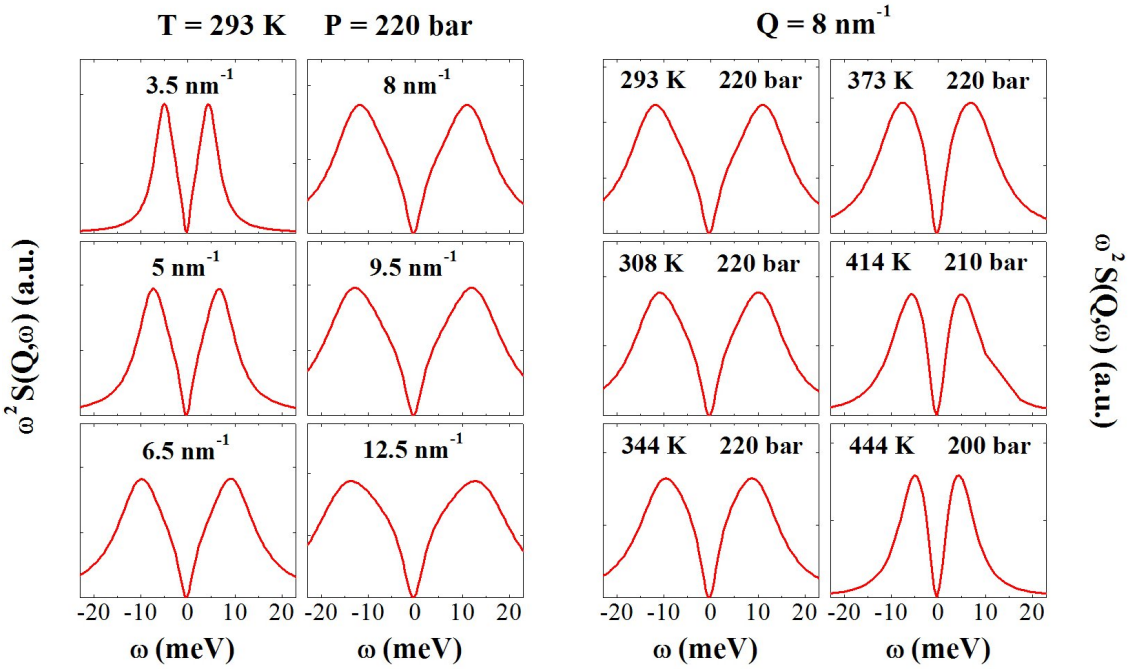

Figure 4.10: *Longitudinal current spectra corresponding to the IXS spectra of fig.4.6.*

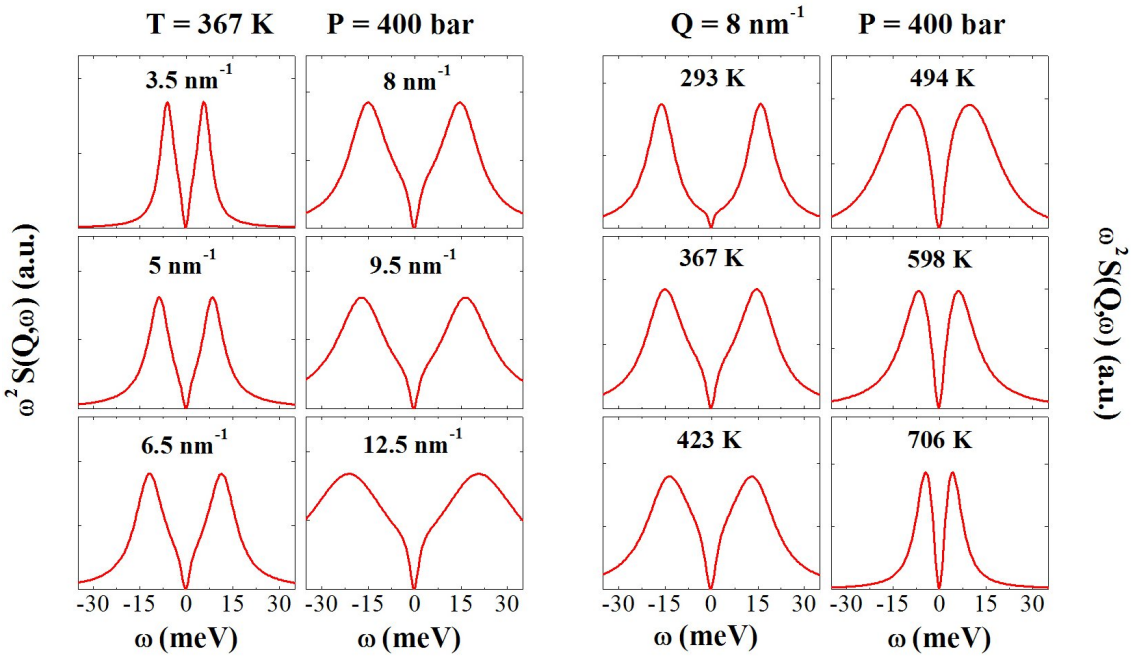

Figure 4.11: *Longitudinal current spectra corresponding to the IXS spectra of Fig.4.7.*

4.2.5 Viscosity

Once the fitting parameters are obtained, the Q-dependent values of the longitudinal viscosity, $\eta_L(Q)$, can be calculated, since they are proportional to the time integral of the "viscous" part of the memory function (see eq.2.87):

$$\eta_L(Q) = \frac{\rho}{Q^2}[\Delta_\alpha^2(Q)\tau_\alpha(Q) + \Gamma_\mu(Q)] \tag{4.11}$$

4.2.6 Comparison with structural data

For all the investigated thermodynamic states of each sample, the energy integrated scattering intensity was collected as well. From these measurements it is possible to obtain the value of $S(Q)$, once the measured signal is corrected for the molecular form factor [75], the polarization factor, the effective scattering volume and the detector background. This corrected signal was then scaled by an arbitrary factor in order to match the known $Q = 0$ limit of the $S(Q)$ (compressibility limit), which can be calculated from the EoS. From this, the values of $c_T(Q)$ can be calculated using eq.4.5.

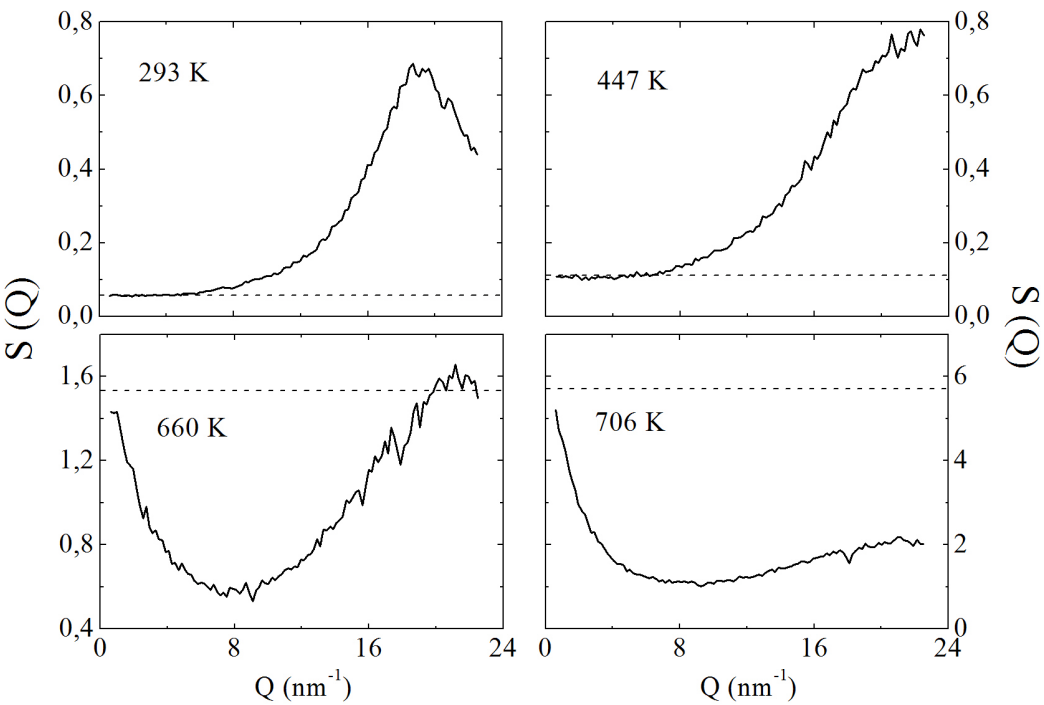

Figure 4.12: *Examples of low-Q critical scattering in water. The dashed horizontal lines indicate the values of* $S(Q = 0)$.

The comparison between $c_T(Q)$ calculated from the $S(Q)$ (full lines in figs.4.13, 4.14, 4.15 and 4.16) and the best fit results (black squares) is a check of consistency of the overall fitting procedure. Inspecting these figures it can be noticed that the

quantitative agreement between the two procedures is very good, except in the case of neon. Here, the fits systematically underestimate the structural data by about 10 %.

Furthermore, in the supercritical state, the insurgence of critical fluctuations reflects in a strong increase of the $S(Q)$ at low Q. In this case the scaling to the known $Q = 0$ limit presents severe difficulties, as can be seen in fig.4.12 by inspecting the data at 660 and 706 K. In the cases of water at 706 K and ammonia at 444 K the normalization to the compressibility limit was performed by adjusting the values of $1/\sqrt{S(Q)}$ to the ones of $\Omega_T(Q)$ obtained from the fits.

4.3 Experimental results

In this section the results of the data analysis of the four samples are reported. The obtained results can be logically divided into four classes: the ones concerning the sound dispersion relations (section 4.3.1), the structural relaxation (section 4.3.2), the instantaneous relaxation (section 4.3.3) and the viscosity (section 4.3.4).

4.3.1 Dispersion relations

Figs.4.13, 4.14, 4.15 and 4.16 report the various dispersion relations for some selected thermodynamic states. In particular, the dispersion of longitudinal modes, $\Omega_L(Q)$ *vs.* Q (blue diamonds), as obtained from the longitudinal current spectra, are compared with:

i) The isothermal dispersion, $c_T(Q)Q$, either obtained from the fit (black squares), or independently calculated from the measured $S(Q)$ (full lines).

ii) The adiabatic dispersions, $\gamma^{1/2}c_T(Q)Q$ (red circles).

iii) The infinite dispersions, $\Omega_\infty(Q)$ (green triangles), as obtained from the fit.

iv) The inverse of the structural relaxation time, $\tau_\alpha^{-1}(Q)$ (dashed lines), obtained by interpolating the experimental data (see section 4.3.2 further below).

In all these figures it is evident that $\Omega_L(Q)$ departs from the expected adiabatic dispersion at the lower temperatures, and bends up to join the infinite one (positive sound dispersion). The crossover between the two regimes of sound propagation corresponds to the crossover condition $\tau_\alpha(Q)\Omega_L(Q) \sim 1$ (vertical arrows in the figures). In some cases the crossover condition is met again at higher Q, due to both the decrease of $\Omega_L(Q)$ in the proximity of the FSDP and the decrease of $\tau_\alpha(Q)$. This leads to a "back-transition" of the longitudinal dispersion from the infinite to the adiabatic one. In all cases $\tau_\alpha^{-1}(Q)$ shifts to higher frequencies with increasing temperature, and, at the same time, the sound velocity (and therefore $\Omega_L(Q)$) becomes smaller. As a consequence the fully relaxed condition, $\Omega_L(Q)\tau_\alpha(Q) \ll 1$, is satisfied over the whole Q-range (i.e. the elastic regime is never reached). For temperatures higher than the critical one $\Omega_L(Q)$ and $\Omega_s(Q)$ merge together, at least in the low and intermediate Q-range.

Finally, it can be observed that the longitudinal dispersion lies systematically below the adiabatic one, at the higher Q-T values. This is particularly evident in the case

of Nitrogen and Ammonia, where $\Omega_L(Q)$ departs from the adiabatic value and bends downwards to join the isothermal dispersion.

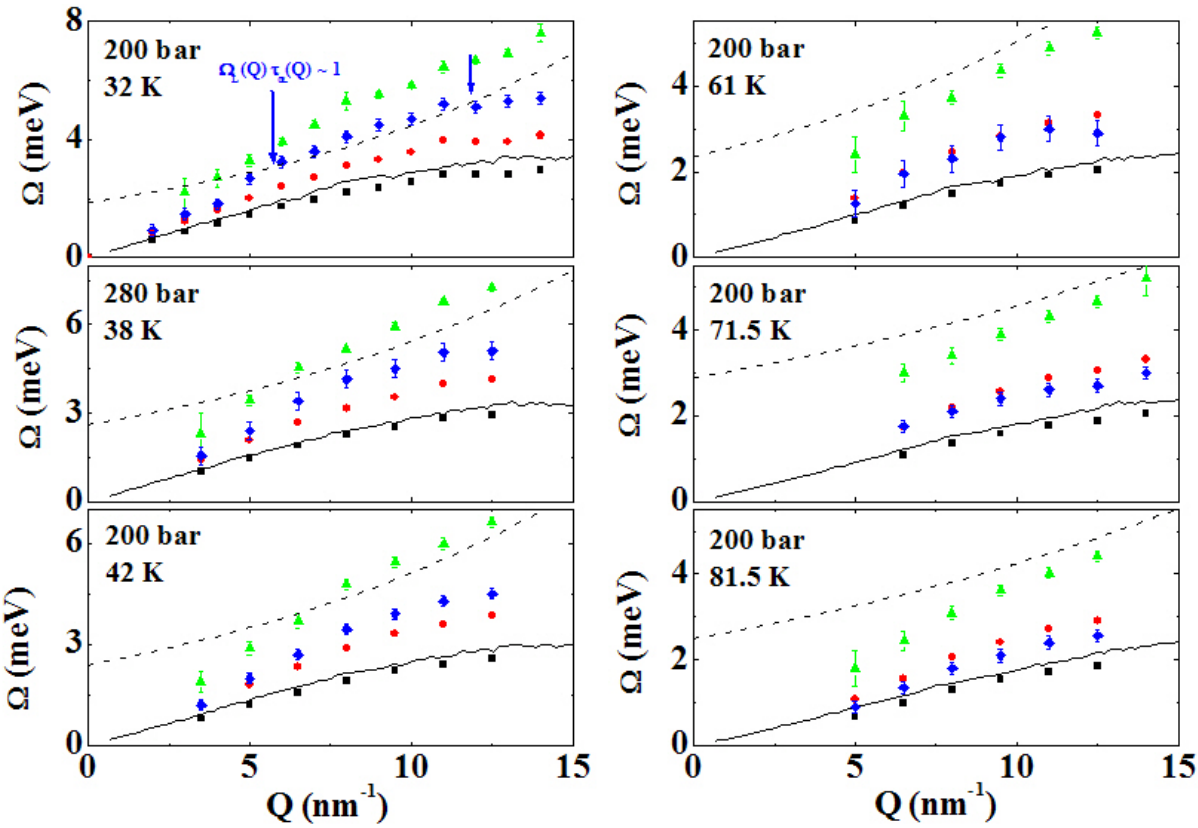

Figure 4.13: neon: *comparison between isothermal (black squares), adiabatic (red circles), infinite (green triangles) and longitudinal dispersion (blue diamonds) at the thermodynamic states indicated in the figure. The isothermal dispersion derived from the experimental $S(Q)$ (solid line) is reported as well. The dashed line indicates the values of $1/\tau_\alpha(Q)$, as obtained from a linear interpolation (see fig.4.19). The vertical arrows indicate the crossover condition: $1/\tau_\alpha(Q) \sim \Omega_L(Q)$.*

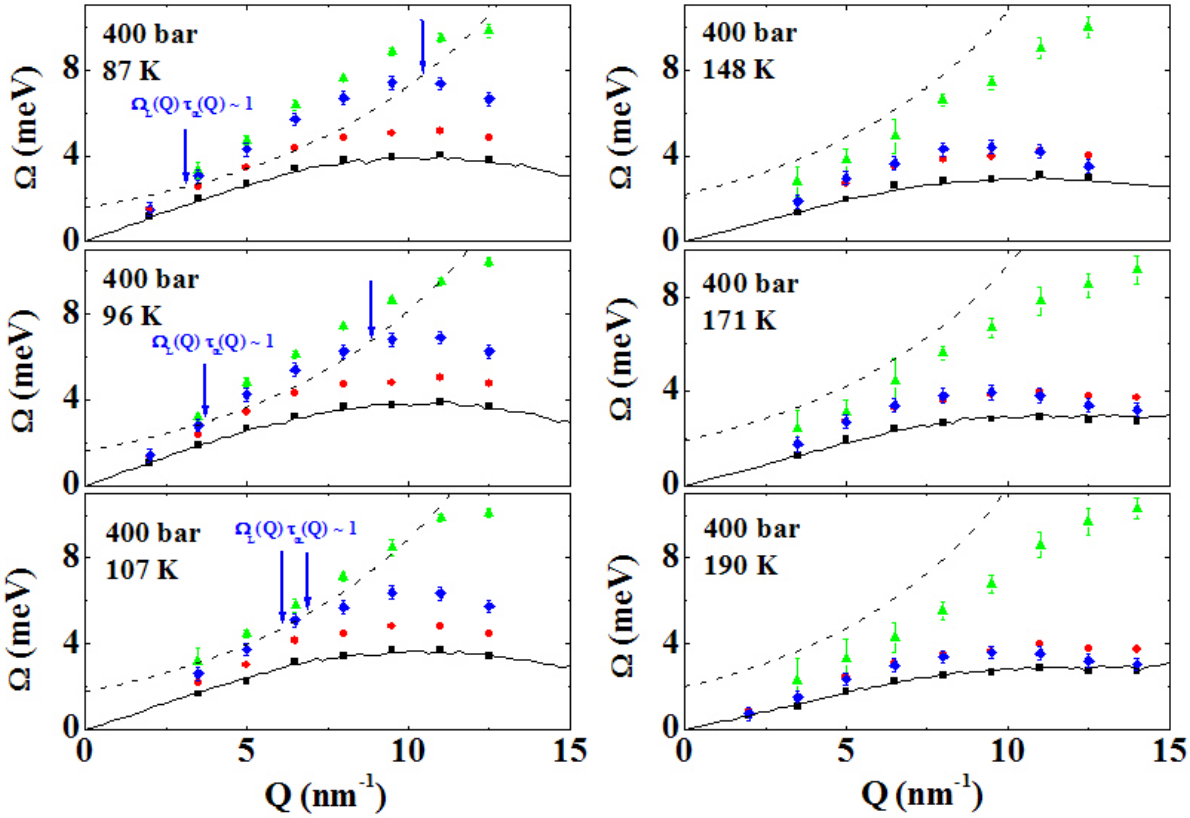

Figure 4.14: *As in fig.4.13 for nitrogen.*

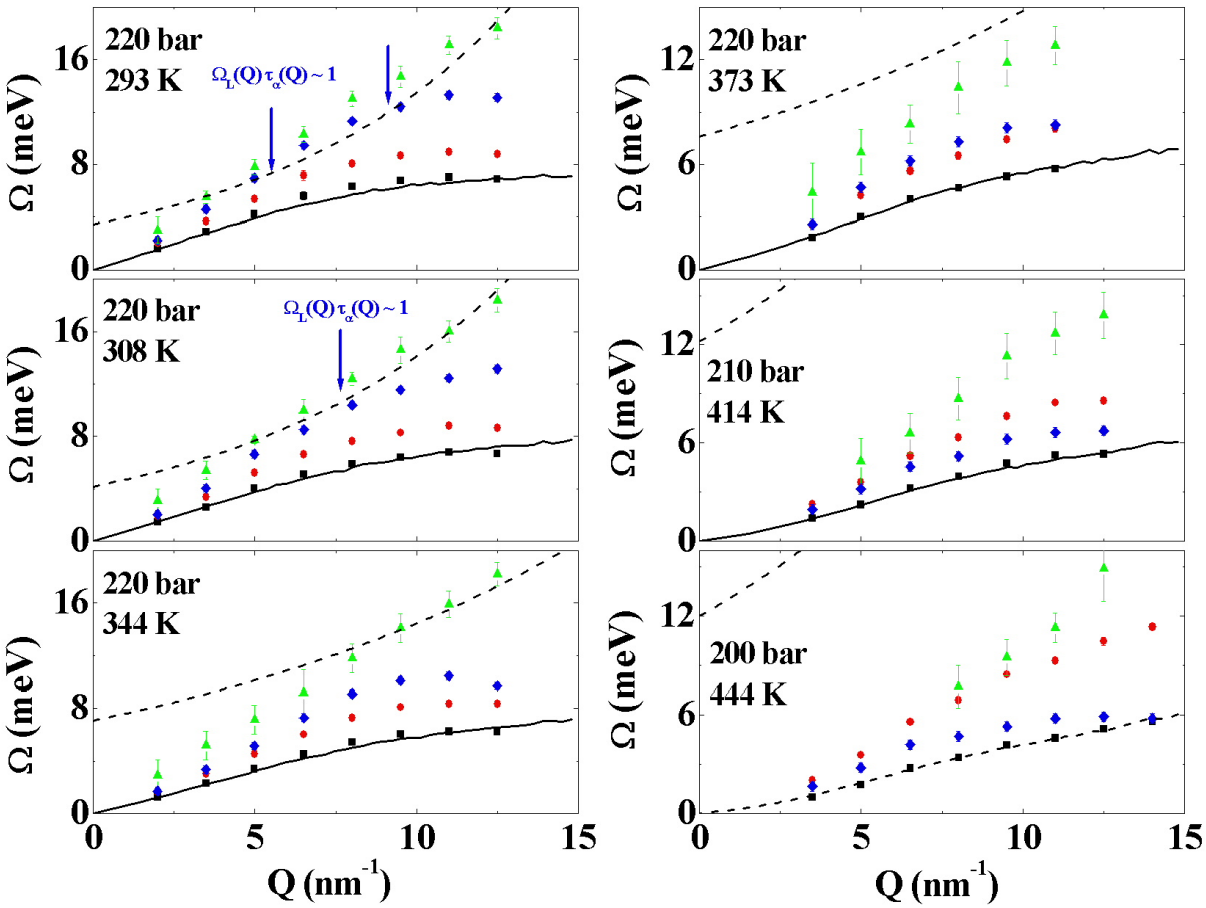

Figure 4.15: *As in fig.4.13 for ammonia.*

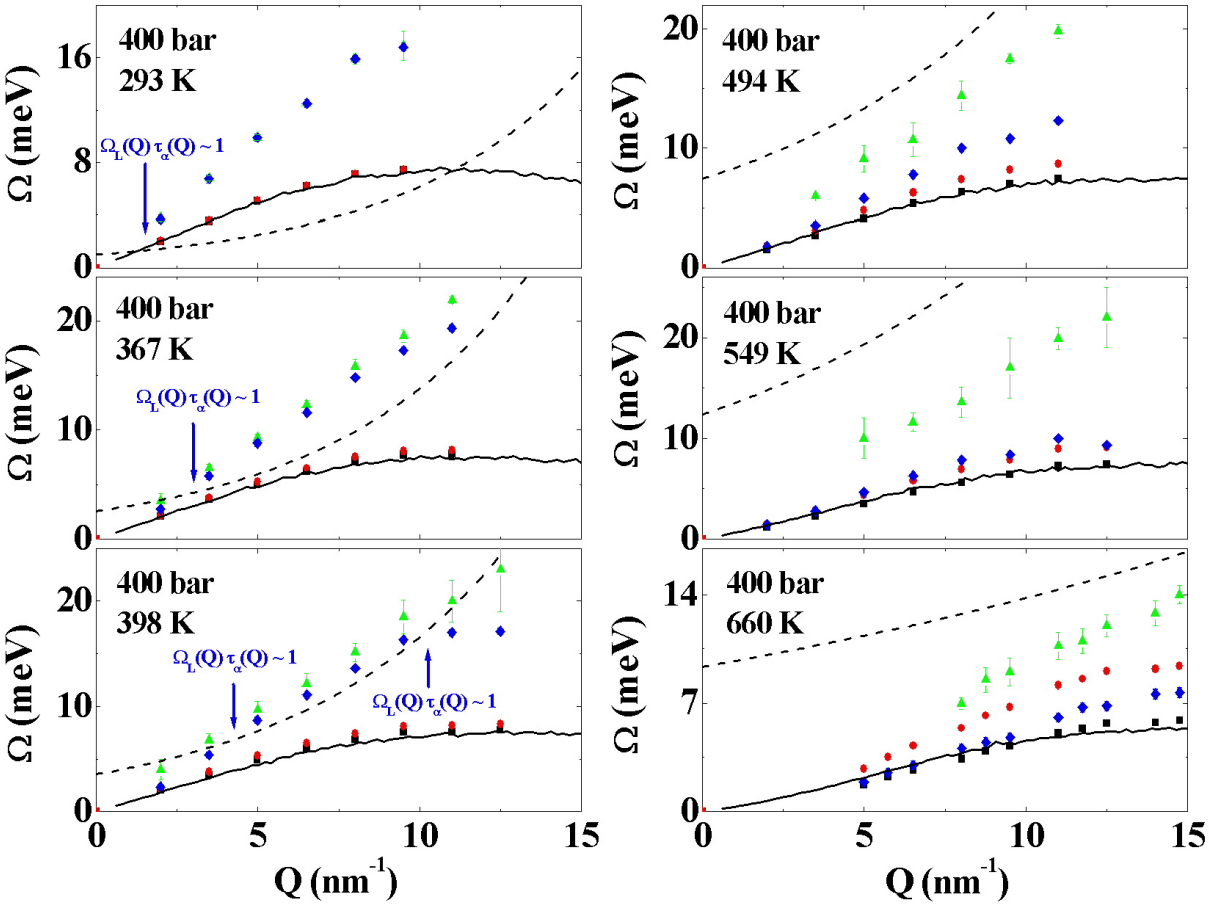

Figure 4.16: *As in fig.4.13 for water.*

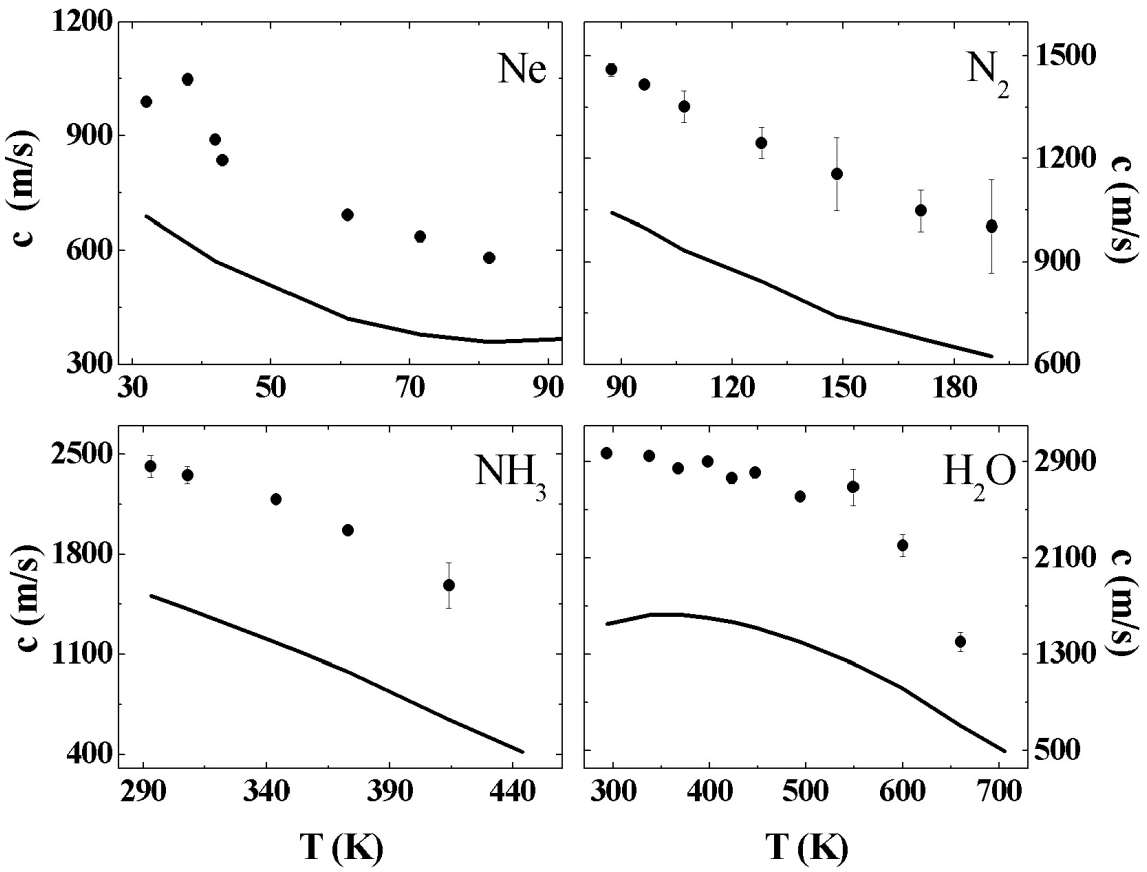

Figure 4.17: *Temperature dependence of the infinite-frequency sound velocity (dots) compared with the respective value of c_s (line).*

Inspecting figs.4.13 - 4.16, it can be noticed that the infinite-frequency sound dispersion, $\Omega_\infty(Q)$ *vs.* Q, always shows an almost linear behavior in the lower ($< 6.5 \div 8$ nm^{-1}) Q-range. Therefore, interpolating these dispersions with a linear function:

$$\Omega_\infty(Q) = c_\infty Q \tag{4.12}$$

one obtains the values of the infinite frequency sound velocity, c_∞. These values can be considered as a macroscopic ($Q = 0$) property of the system, since they are no longer affected by Q-dependencies. The results of these linear interpolations are reported in fig.4.17 as a function of the temperature. In the case of water at 706 K and ammonia at 444 K, data for $\Omega_\infty(Q)$ at $Q < 8$ nm^{-1} were impossible to extract from the spectra. Therefore, c_∞ were not extracted in these cases. The lines in this picture represent the temperature dependence of the adiabatic sound velocity, c_s, along the explored isobaric path[3]. The data of c_s have been derived from the respective EoS.

[3]We recall that, in the case on Neon, the c_∞ data at $T = 38$ and 43 K correspond to another pressure.

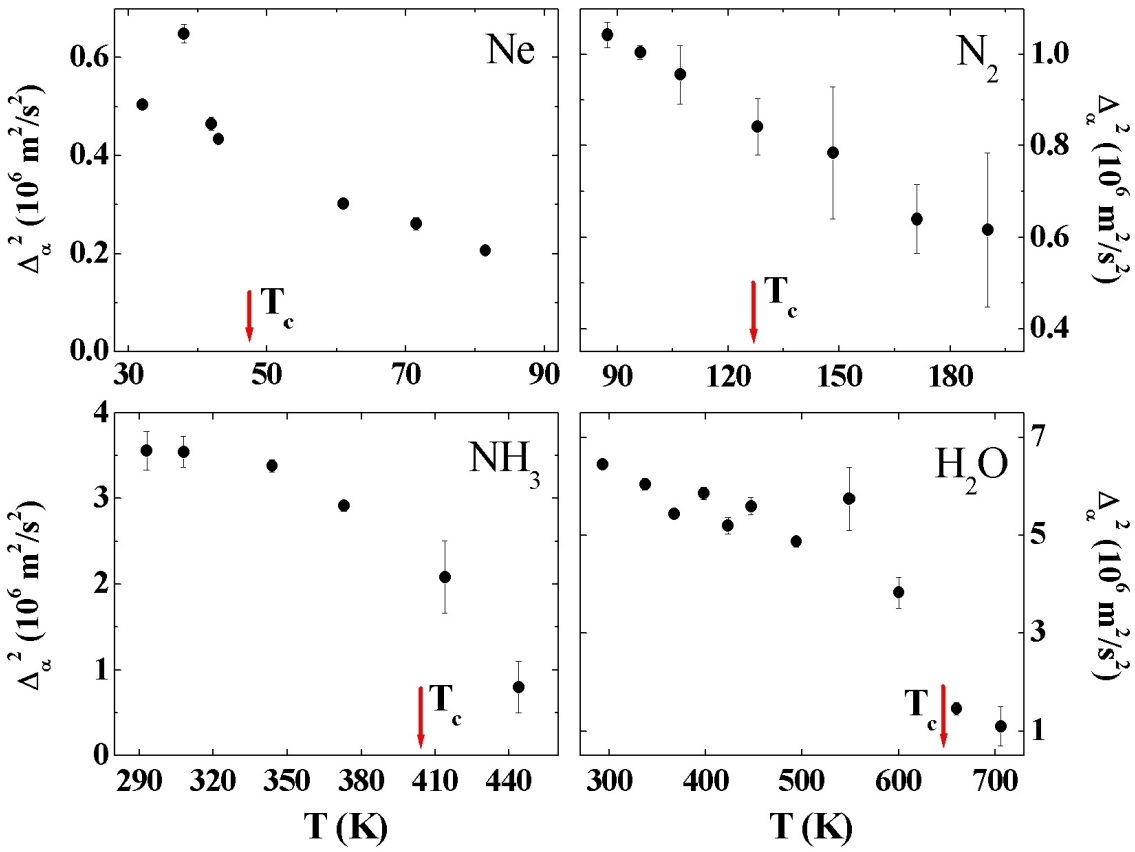

Figure 4.18: *Values of Δ_α^2 as a function of temperature. The red vertical arrows indicate the respective critical temperature.*

4.3.2 Structural relaxation

The structural relaxation strength can be related to the adiabatic and infinite-frequency sound velocities through the finite-Q generalization of eq.2.84:

$$\Delta_\alpha^2(Q) = [c_\infty^2(Q) - c_s^2(Q)]Q^2 \tag{4.13}$$

Once the $Q = 0$ value of c_∞ and c_s is known, it is possible to calculate the macroscopic ($Q = 0$) limit of the structural relaxation strength:

$$\Delta_\alpha^2 = lim_{Q\to 0}[\Delta_\alpha^2(Q)/Q^2] = [c_\infty^2 - c_s^2] \tag{4.14}$$

Using the values of the sound velocities reported in fig.4.17, it is possible to calculate Δ_α^2. The temperature dependence of this parameter is reported in fig.4.18. Owing to the lack of values for c_∞, in the case of water at 706 K and ammonia at 444 K, Δ_α^2 was calculated as the average of $\Delta_\alpha^2(Q)/Q^2$. For all samples Δ_α^2 decreases with temperature and it does not seem to be affected by the transition from the liquid to the supercritical phase.

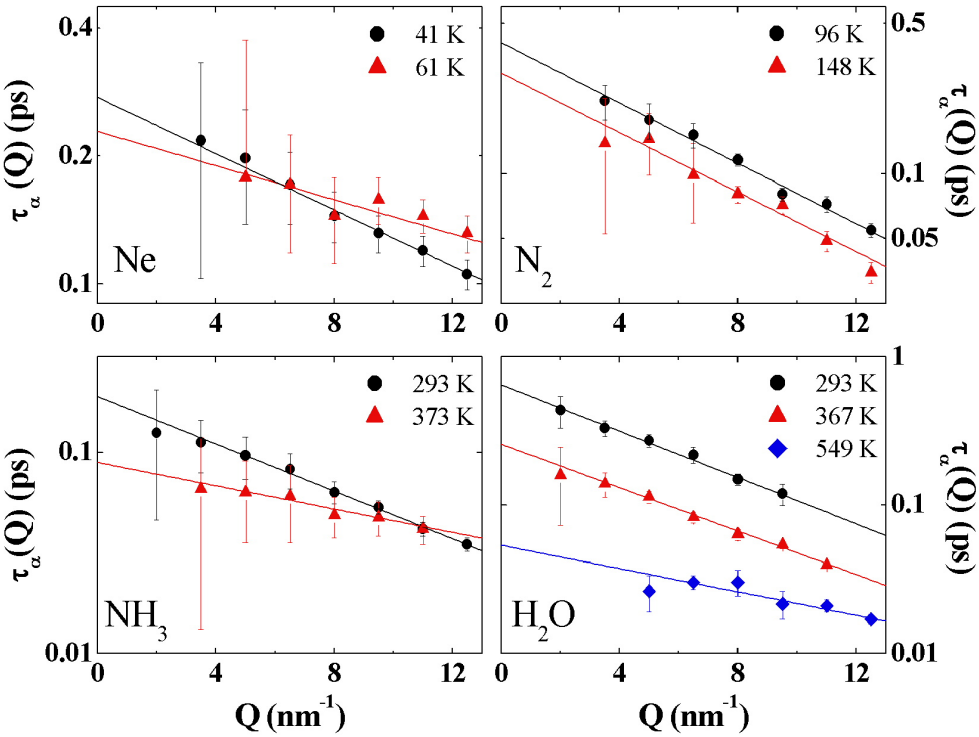

Figure 4.19: *Q-dependence of the structural relaxation times for the indicated thermodynamic states. The lines through the data are linear interpolations.*

The Q-dependence of $\tau_\alpha(Q)$ is reported in fig.4.19 for some selected thermodynamic states. As already observed in other experiments [19, 37, 38, 41, 76, 77, 78], $\tau_\alpha(Q)$ decreases with increasing Q. Furthermore, an exponential decay of $\tau_\alpha(Q)$ *vs.* Q has been found to describe very well the experimental data. The Q-dependence of this parameter, in the reported Q-range, can therefore be empirically described by the following equation:

$$\tau_\alpha(Q) = \tau_\alpha e^{-AQ} \tag{4.15}$$

Interpolating $\tau_\alpha(Q)$ with the formula expressed in eq.4.15, the values of the relaxation time at $Q = 0$ (τ_α) and of the "logarithmic slope" (A) can be therefore obtained. In the case of ammonia at 444 K, only four values of $\tau_\alpha(Q)$, in the Q-range $8 \div 12.5$ nm^{-1}, were obtained; moreover, their relative errors were very large. Consequently, the parameter A in eq.4.15 has been considered as fixed to a value (0.09) estimated from the trend of A at the lower temperatures (see insets of fig.4.20), in order to reduce the uncertain in the value of τ_α. This assumption strongly affects the absolute value of τ_α, as can be observed in fig.4.20, where, for ammonia at 444 K, the value of τ_α obtained by imposing $A = 0.05$ is reported as well.

Fig.4.20 reports the values of τ_α as a function of temperature. It can be noticed that τ_α first decreases with increasing temperature, and then remains almost flat for temperatures higher than the critical one (indicated by red vertical arrows).

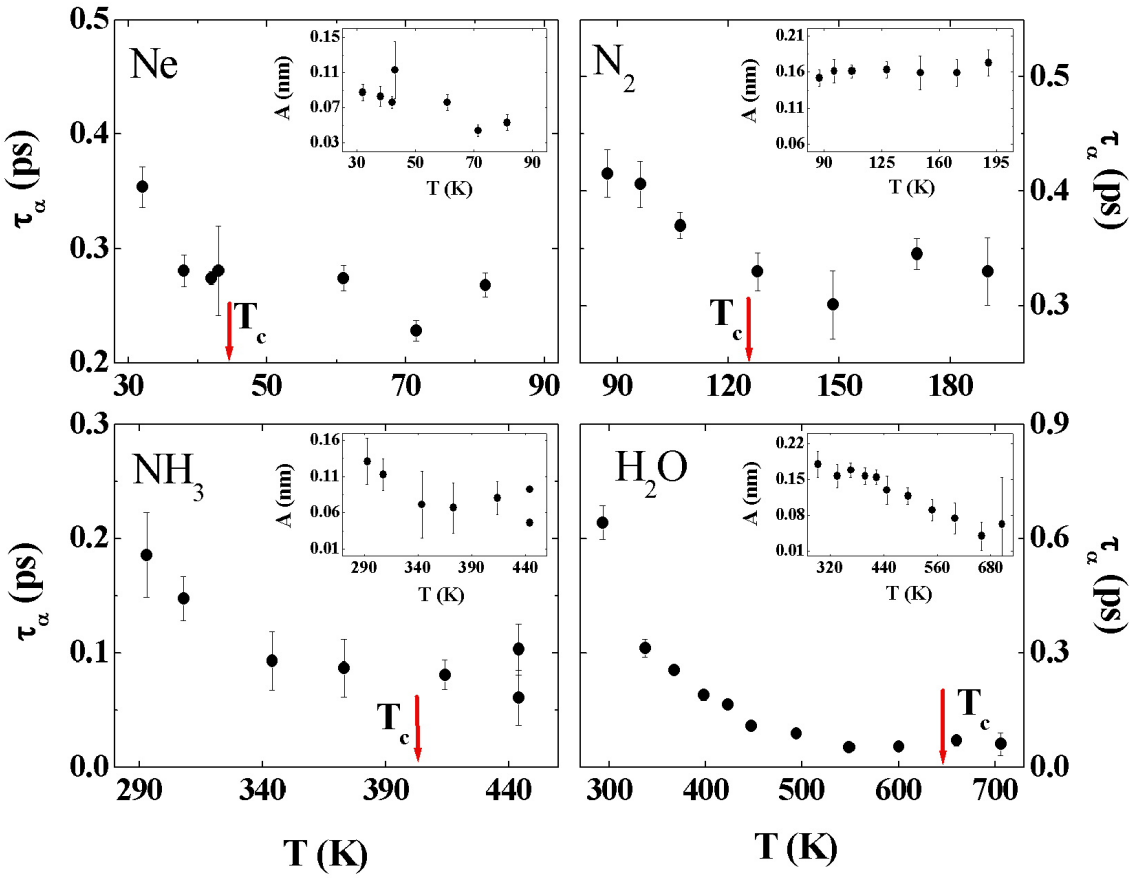

Figure 4.20: *Temperature dependence of τ_α, the vertical arrows indicate the critical temperature. The respective values of the parameter A are reported in the insets. The two data points at the highest temperature of ammonia correspond to $A = 0.09$ (upper one) and $A = 0.05$ (lower one). See text for further details.*

4.3.3 Instantaneous relaxation

Another parameter which is provided by the analysis of the IXS spectra is $\Gamma_\mu(Q)$, the integrated intensity of the instantaneous relaxation. These values have been found to be imprecisely determined, since the associated error bars are quite large. Moreover, in the case of Neon, this instantaneous term in the memory function gives a negligible contribution to the spectra, and the resulting values of $\Gamma_\mu(Q)$ are always consistent with zero[4].

The values of $\Gamma_\mu(Q)$ are reported in the left panels of figs.4.21, 4.22 and 4.23, for some selected temperatures. The parabolas in these pictures are guides to the eye and suggest that the Q-dependence of $\Gamma_\mu(Q)$ is consistent with a Q^2 behavior at low-Q. For larger Q values, this parameter departs from the quadratic behavior and becomes increasingly smaller. At the higher Q values it gives a negligible contribution to the spectra.

The temperature dependence of $\Gamma_\mu(Q)$ is reported in the right panels of figs.4.21, 4.22 and 4.23 for different Q-values. $\Gamma_\mu(Q)$ tends to become smaller at high temperature, but this decease is not particularly pronounced.

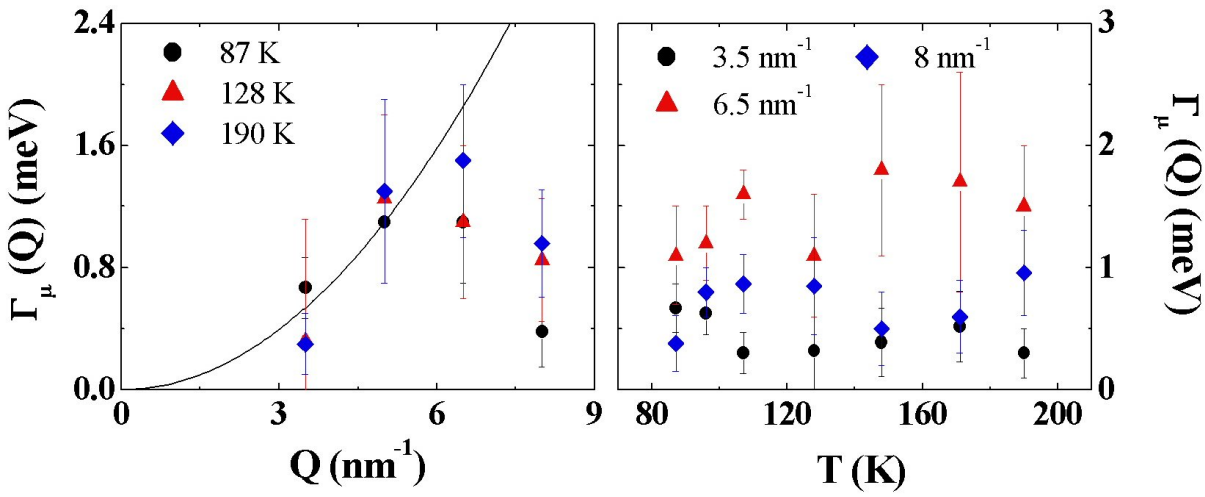

Figure 4.21: Nitrogen: *values of* $\Gamma_\mu(Q)$ *vs.* Q *at the temperatures indicated in the figure (left panel). The parabola is a guide for the eye. Values of* $\Gamma_\mu(Q)$ *vs. temperature at the* Q*-values indicated in the figure (right panel).*

[4]Also for some high-Q data of the other samples, especially for Nitrogen, values of $\Gamma_\mu(Q)$ consistent with zero have been found. They are not reported in the following pictures.

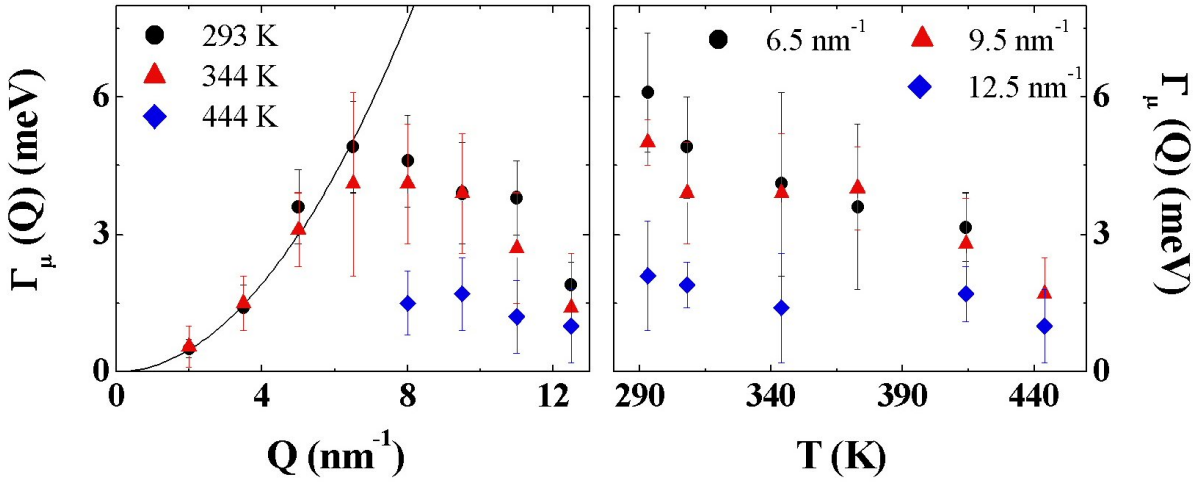

Figure 4.22: Ammonia: *as in fig.4.21.*

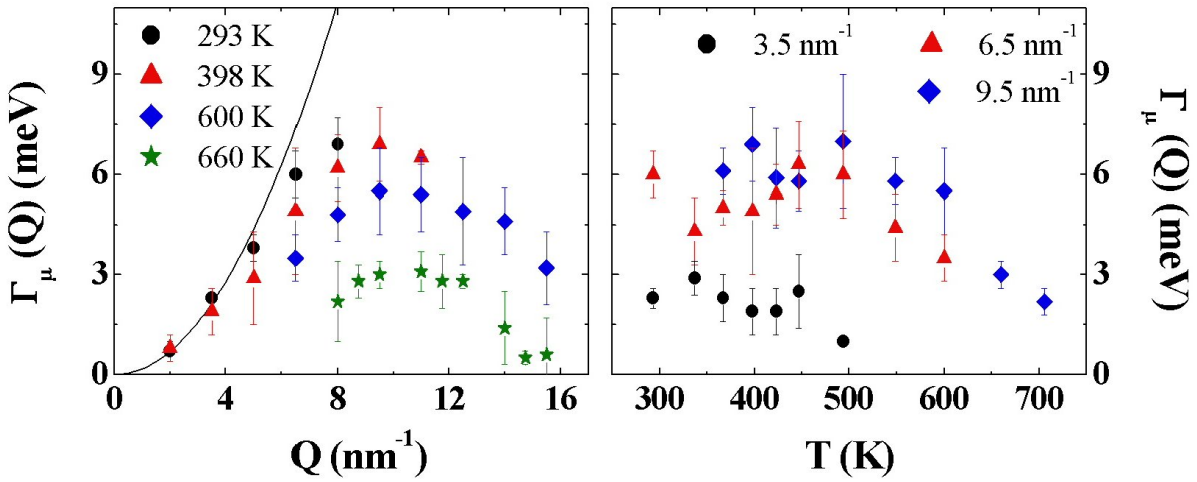

Figure 4.23: Water: *as in fig.4.21.*

4.3.4 Viscosity

The value of $\eta_L(Q)$ can be derived from the fit results, using eq.4.11. Fig.4.24 reports $\eta_L(Q)$ for some selected temperatures. The lines through the data are the interpolations performed with an exponential decay function:

$$\eta_L(Q) = \eta_L e^{-BQ} \tag{4.16}$$

The values of η_L obtained from these interpolations are reported in fig.4.25 as a function of temperature. They are compared to the respective values of the shear viscosity, η_S, obtained from the EoS. The insets report the ratio between these two viscosities. This ratio remains almost constant over the whole explored thermodynamic range, and it is higher for H-bonded liquids. This behavior for η_L/η_S has been already observed in simple liquids [23, 37, 79, 80, 81]. This finding can be therefore considered as a further consistency test of the performed data analysis. The numerical values of these ratios -i.e. 2.34 ± 0.16 (Neon), 2.64 ± 0.12 (Nitrogen), 3.9 ± 0.2 (Ammonia) and 4.3 ± 0.2 (Water)- are in rather good agreement with previous experimental data [37, 82, 83, 84, 85].

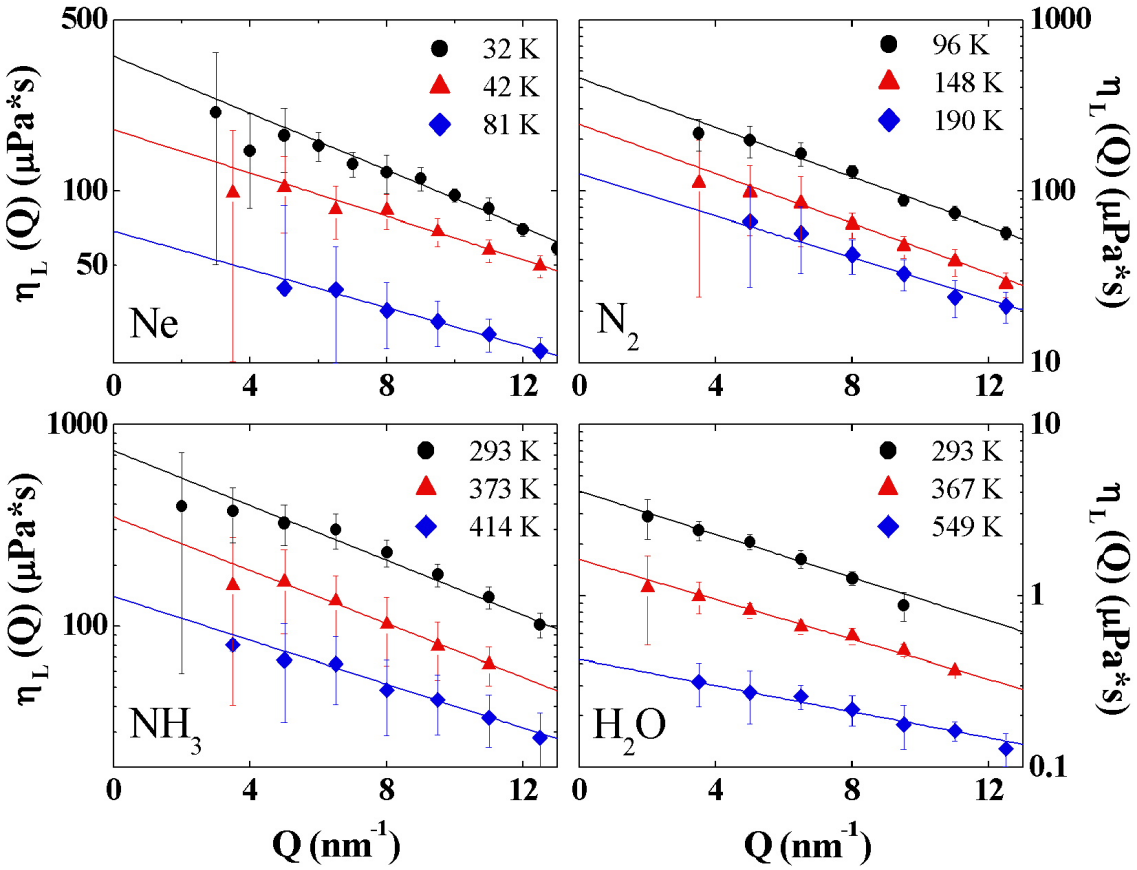

Figure 4.24: *Q-dependence of the longitudinal viscosity, $\eta_L(Q)$, for some selected temperatures. The lines through the points are linear interpolations.*

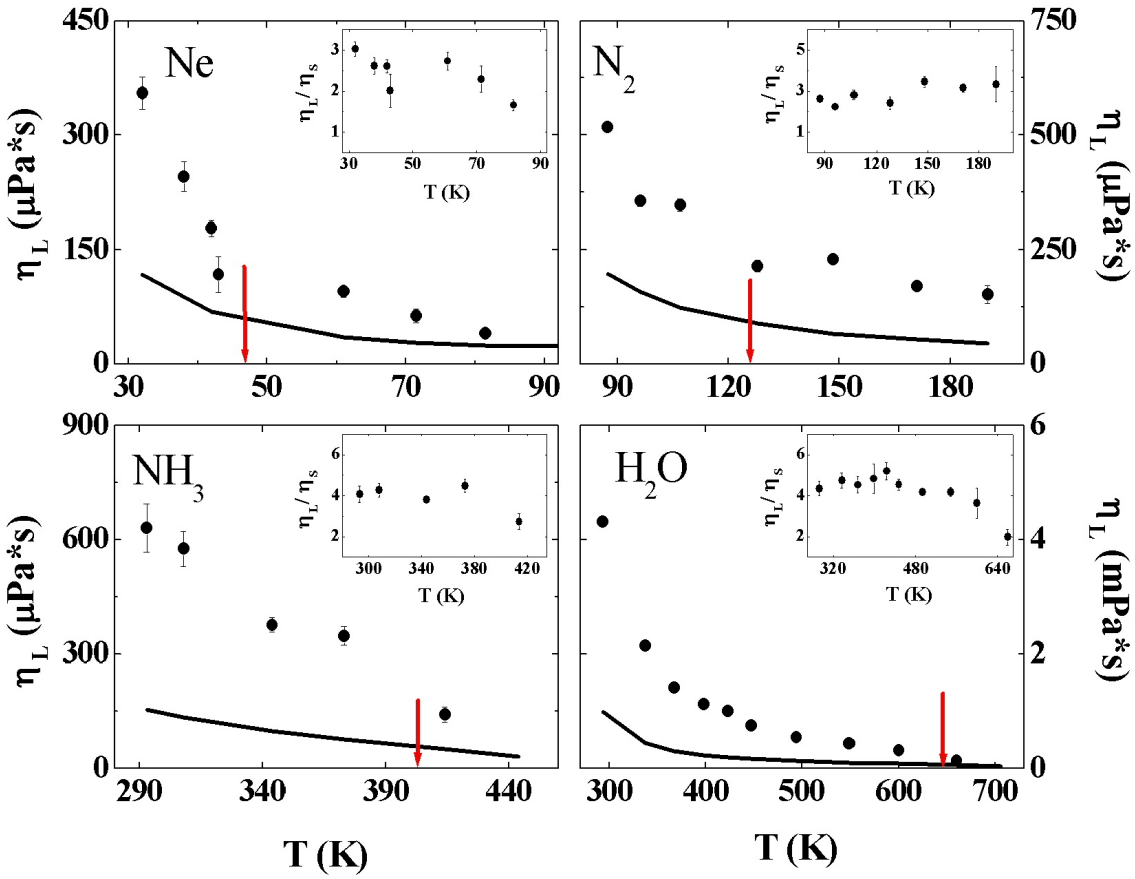

Figure 4.25: $Q = 0$ *extrapolated values of the longitudinal viscosity,* η_L *(circles), and thermodynamic values of the shear viscosity,* η_s *(lines), as a function of temperature. The ratio of the two viscosities is reported in the inset. The vertical arrows indicate the critical temperature.*

4.4 Conclusions

Inspecting the dispersion relations of the various systems, some common phenomenologies can be observed, namely:

i) The infinite frequency dispersion shows an almost linear behavior up to rather high Q-values. Furthermore, it becomes softer on approaching the first sharp diffraction peak. Nevertheless, the Q-dependence of this dispersion is less pronounced than the Q-dependencies of the isothermal and adiabatic dispersions.

ii) The adiabatic and infinite-frequency dispersions do not coincide in any case. This leads to a non-vanishing contribution from the structural relaxation.

iii) The isothermal dispersion calculated from the $S(Q)$ and the one obtained from the fit are in good agreement.

iv) The phenomenon of positive sound dispersion is observed in all the samples, but it disappears close to and above the critical temperature.

v) A new dispersive effect, which brings the longitudinal dispersion below the adiabatic one, was observed in the supercritical phase.

Some other common phenomenologies can be evinced comparing the results concerning the structural and instantaneous relaxation processes:

i) The Q dependence of $\tau_\alpha(Q)$ can be very well described by an exponential decay.

ii) In the liquid phase the value of τ_α decreases with increasing temperature.

iii) In the supercritical phase the value of τ_α is almost temperature-independent.

iv) In the liquid and supercritical phase the value of Δ_α^2 decreases with increasing temperature, and, moreover, it does not change its behavior on crossing the critical temperature.

v) The values of $\Gamma_\mu(Q)$ are twice as big in Water and Ammonia than in Nitrogen. In Neon the contribution of $\Gamma_\mu(Q)$ is negligible.

A more exhaustive quantitative analysis of these results will be given in the next chapter.

Résumé du chapitre 5

Le dernier chapitre résume les résultats expérimentaux dans une vision commune, avec le but de fournir une description générale de la dynamique à haute fréquence de fluides, tant dans la phase liquide que dans la phase supercritique. Une corrélation systématique entre le comportement dispersive de modes longitudinaux et les processus de relaxation a été observée en particulier. De plus, on a observé que les paramètres caractéristiques des processus de relaxation dépendent spécifiquement des quantités thermodynamiques, comme la densité et la température. Enfin, les coefficients qui quantifient ces dépendances ont été corrélés aux propriétés spécifiques du système étudié.

Chapter 5

The high-frequency dynamics of liquids and supercritical fluids

In this chapter the previously presented experimental results are cast into a common frame, with the aim to provide a general picture of the high-frequency dynamics of a fluid across the transition between the liquid and the supercritical phase.

5.1 Sound dispersion

In this section the dispersive behavior of longitudinal acoustic modes in different samples is compared. The relationship between this behavior and the relaxation processes of the memory function are discussed.

5.1.1 Positive sound dispersion

Positive sound dispersion has been already observed in many experimental and theoretical works, and was interpreted as a manifestation of the structural relaxation process [19, 37, 38, 39, 40, 41]. In order to highlight the relationship between structural relaxation and positive sound dispersion, it is advisable to define the reduced longitudinal modulus:

$$M(Q) = [\Omega_L^2(Q) - \Omega_s^2(Q)]/[\Omega_\infty^2(Q) - \Omega_s^2(Q)] \tag{5.1}$$

The function $M(Q)$ is particularly suited for a comparative investigation, since it does not depend on the specific values of the limiting sound velocities. $M(Q)$ always ranges between zero and one; in particular it vanishes when $\Omega_L(Q) = \Omega_s(Q)$, while it assumes the value of one when $\Omega_L(Q) = \Omega_\infty(Q)$. Moreover, within the hypothesis that positive dispersion is induced by structural relaxation, $M(Q) = 0.5$ when $\Omega_L(Q)\tau_\alpha(Q) = 1$.

$M(Q)$ is reported as a function of $\Omega_L(Q)\tau_\alpha(Q)$ in fig.5.1. The data at higher temperatures[1] are not reported because the dispersion relation, in these cases, is dom-

[1]Namely: Neon at 71.5 and 81.5 K, Nitrogen at 171 and 191 K, Ammonia at 414 and 444 K and Water at 660 and 706 K

inated by the negative sound dispersion. On the other hand, the eventual competing effect of the negative sound dispersion, associated with the thermal relaxation, can be ignored for the temperatures reported in fig.5.1, since the strength of the thermal relaxation, $\Delta_T^2(Q) = (\gamma - 1)c_T^2(Q)$, is roughly one order of magnitude lower than the strength of the structural one, $\Delta_\alpha^2(Q) = c_\infty^2(Q) - c_s^2(Q)$, especially at high Q-values. This estimation can be done considering that it was experimentally observed that $c_\infty \sim 2c_s$. Therefore, even for relatively high values of γ ($\sim 2 \div 4$), one can estimate that $\Delta_T^2/[\Delta_T^2 + \Delta_\alpha^2] \sim 0.15$. Moreover, at high Q-values $\Delta_T^2(Q)$ decreases as $S(Q)^{-1}$, because it is proportional to $c_T^2(Q)$. On the other hand, $\Delta_\alpha^2(Q)$ increases with Q, since the decrease of $c_\infty(Q)$ is less pronounced than the one of $c_s(Q)$ (see figs.4.13 - 4.16). In view of these considerations it can be concluded that the structural relaxation process leads to the stronger dispersive effect. Therefore, as long as the structural relaxation time is inside the probed frequency window, the thermal relaxation can be regarded as a secondary effect that does not substantially affect the dispersion of sound modes, but only leads to small distortions (roughly a few %) with respect to the ideal behavior.

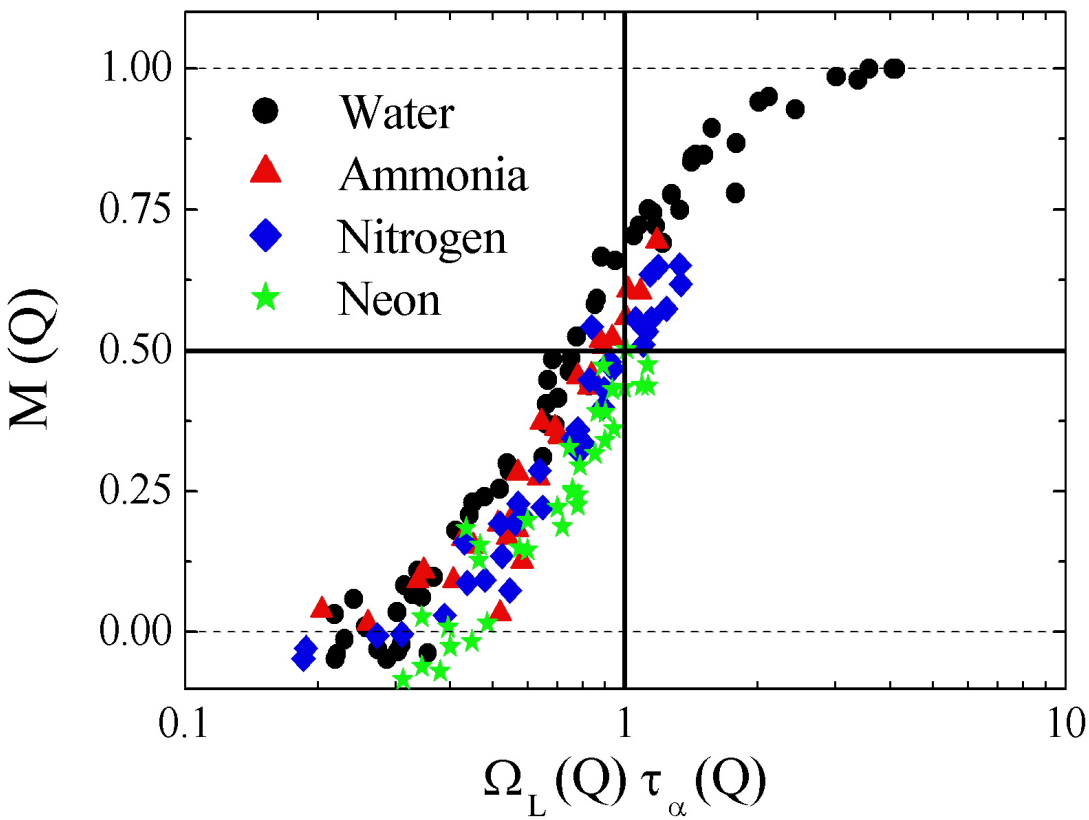

Figure 5.1: *Reduced longitudinal moduli, $M(Q)$, as a function of $\Omega_L(Q)\tau_\alpha(Q)$. Most of the data corresponds to the liquid phase of the respective sample.*

Inspecting fig.5.1, it can be clearly appreciated that $M(Q)$ tends to zero/one when $\Omega_L(Q)$ is shorter/longer than $\tau_\alpha^{-1}(Q)$. Furthermore, all the data are around $M(Q) = 0.5$

when $\Omega_L(Q)\tau_\alpha(Q) = 1$. This result demonstrates a clear correlation between positive sound dispersion and structural relaxation.

5.1.2 "Negative" sound dispersion

In all investigated samples a bending down of the longitudinal dispersion with respect to the expected adiabatic value was observed in the supercritical phase (see figs.4.13 - 4.16). To the best of our knowledge, the phenomenon of negative sound dispersion in liquids has never been observed before, despite being predicted by hydrodynamic theories. There are many reasons for that: i) The crossover occurs typically at large Q, often around the position of the first sharp diffraction peak (FSDP) of the $S(Q)$. Here, the finite-Q generalization of the isothermal sound speed $c_T(Q)$ -which is proportional to $S(Q)^{-1/2}$- becomes too small to be reliably extracted from the measured $S(Q,\omega)$ spectra. ii) In liquids the structural relaxation, which leads to the competing effect of positive dispersion, is always inside or close to the (Q,ω)-range where negative dispersion is expected. As a consequence, this stronger dispersive effect completely masks the eventual presence of a negative dispersion.

One interpretation of this dispersive feature can be found in an adiabatic to isothermal transition of sound propagation induced by the thermal diffusion process [25]. This process can be associated with a thermal relaxation, whose characteristic timescale and strength are, respectively, $\tau_T(Q) = 1/\gamma D_T Q^2$ and $(\gamma - 1)c_T^2(Q)$ [20, 21, 22, 23, 24, 25]. Contrary to other relaxation processes, its fully unrelaxed limit is always reached at low-Q, owing to the Q^{-2} dependence of $\tau_T(Q)$. As a consequence, the higher sound velocity (i.e. c_s) characterizes the low-(Q,ω) region of the dispersion relation. On the other hand, on increasing Q, $\tau_T(Q)$ decreases much faster than the period of longitudinal modes; the fully unrelaxed limit is therefore reached above a certain Q. In this limit the sound velocity is lower and corresponds to the isothermal one, c_T.

In order to better investigate the nature of this negative sound dispersion a parameter, like $M(Q)$, that is independent of the specific values of the limiting sound velocities, is needed. One possible choice is:

$$M_T(Q) = [\Omega_L'^2(Q) - \Omega_T^2(Q)]/[\Omega_s^2(Q) - \Omega_T^2(Q)] \tag{5.2}$$

where $\Omega_L'(Q)$ is the value of the longitudinal sound frequency without the contribution arising from the structural relaxation:

$$\Omega_L'(Q)^2 = \Omega_L^2(Q) - [\Omega_\infty^2(Q) - \Omega_s^2(Q)]\frac{(\Omega_L(Q)\tau_\alpha(Q))^2}{1 + (\Omega_L(Q)\tau_\alpha(Q))^2} \tag{5.3}$$

The function $M_T(Q)$ has the same properties as $M(Q)$, namely: $M_T(Q) = 0$ or 1 if $\Omega_L'(Q) = \Omega_T(Q)$ or $\Omega_s(Q)$. Moreover, in analogy to the function $M(Q)$, it should be equal to 0.5 when $\Omega_L'(Q)\tau_T(Q) = 1$.

The necessity to explicitly subtract the dispersive effect of the structural relaxation arises from the fact that, as pointed out in the previous section, the structural relaxation is the dominant dispersive effect. Moreover, its strength increases at high Q-values, where the negative sound dispersion is observed. In the supercritical phase,

$\tau_\alpha(Q)$ moves outside (but not too far) the probed frequency window, and consequently the dispersive effect of the structural relaxation is strongly reduced. This effect is nevertheless comparable to the one associated with thermal relaxation. Finally, as shown in figs.4.18 and 4.20, the structural relaxation strength and timescale strongly depend on the system and the thermodynamic state. The competing effect of positive sound dispersion has therefore different weights for the four investigated systems. This is reflected in relevant systematic discrepancies, that occlude the direct comparison among different samples in different thermodynamic states.

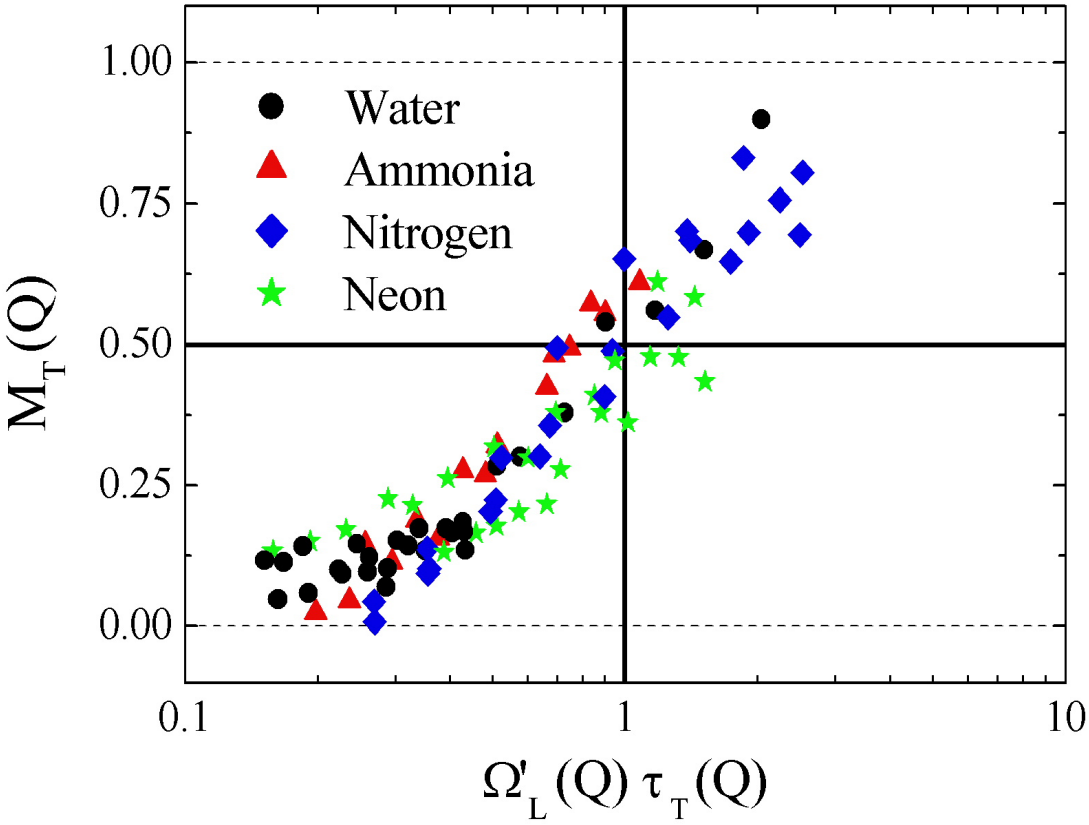

Figure 5.2: *$M_T(Q)$, as a function of $\Omega'_L(Q)\tau_T(Q)$. The data correspond to the supercritical phase of the respective samples.*

The function $M_T(Q)$ is plotted as a function of $\Omega'_L(Q)\tau_T(Q)$ in fig.5.2, where one can observe a clear transition with increasing values of $\Omega'_L(Q)\tau_T(Q)$. A clear correlation between the negative sound dispersion and $\tau_T(Q)$ is therefore observed. This evidence strongly supports the interpretation of the negative sound dispersion as an adiabatic to isothermal transition of sound propagation associated to the thermal diffusion process.

5.2 Structural relaxation

In the presented framework, the structural relaxation process has been described as an exponential time decay of the memory function. Consequently, this process is characterized by only two parameters: $\tau_\alpha(Q)$ and $\Delta^2_\alpha(Q)$. The latter represents the strength of the relaxation, and coincides with the $t = 0$ value of the respective term in the memory function, while the former is the characteristic timescale of the relaxation. Both of them can be obtained from the lineshape analysis of IXS spectra. Moreover, by means of interpolations with empiric functions, it is possible to extract the relative $Q = 0$ values of these parameters: τ_α and Δ^2_α (see section 4.3.2).

5.2.1 Strength of structural relaxation

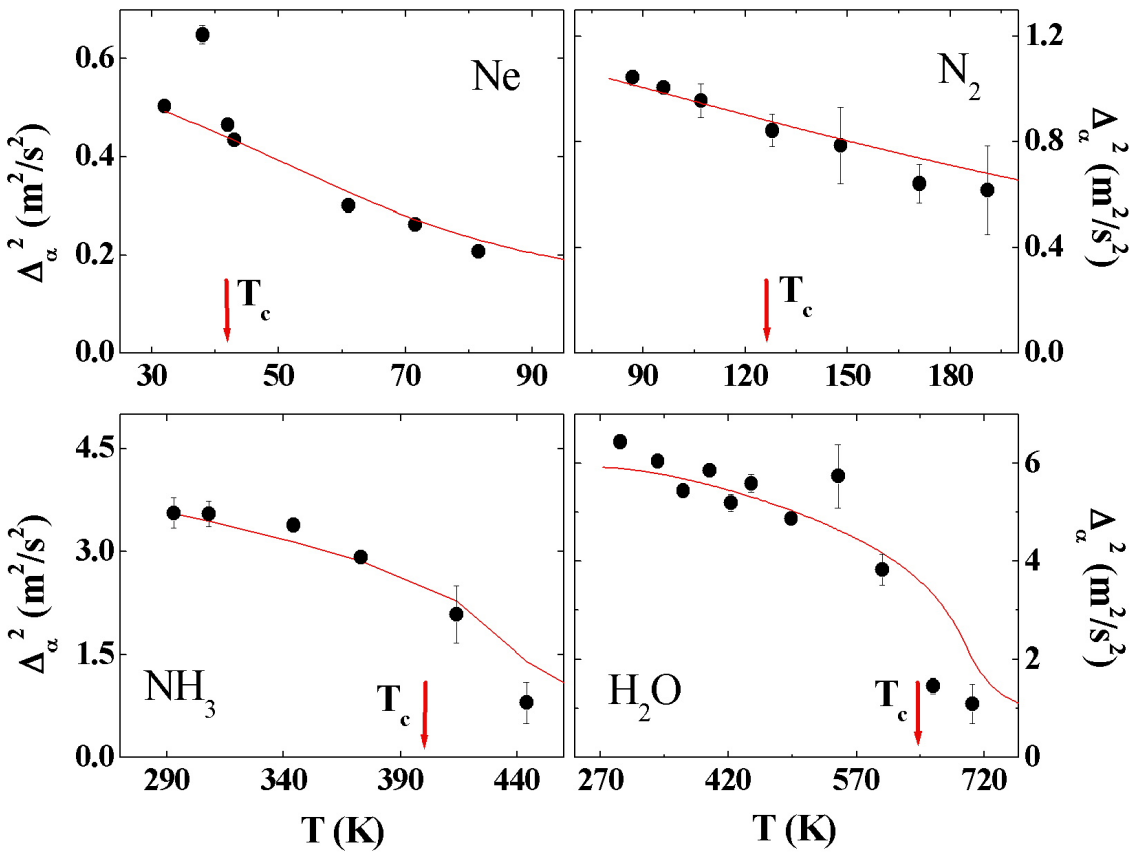

Figure 5.3: *Structural relaxation strength at $Q = 0$ as a function of temperature. The red lines are functions linearly proportional to the density along the corresponding isobaric path.*

Fig.5.3 displays the behavior of Δ^2_α as a function of temperature (full circles). The red lines are functions which are linearly proportional to the density along the respective

isobaric path[2]. A correlation between the temperature dependence of Δ_α^2 and that of the density can therefore be assessed and, consequently, one can also exclude an explicit temperature dependence of Δ_α^2. This result is not completely unexpected, since it has been shown in chapter 2 that $\Delta_\alpha^2(Q)/Q^2$ can be expressed as:

$$\Delta_\alpha^2(Q)/Q^2 = \frac{\omega^4(Q)}{\omega^2(Q)} - \frac{\gamma\omega^2(Q)}{\omega^0(Q)} \tag{5.4}$$

where $\omega^n(Q)$ are the spectral momenta of $S(Q,\omega)$. The second term on the right hand side of eq.5.4 corresponds to the (squared) adiabatic sound velocity, while the first one is equal to $3c_T^2 + \Gamma_L$ (see table 2.1). In a first approximation, all these quantities can be assumed proportional to the density. Consequently, the fact that $\Delta_\alpha^2 \propto \rho$ can be considered as a further experimental check of consistency.

The proportionality constant between the density and the strength of the structural relaxation can be estimated by averaging the values of $\Delta_\alpha^2/\rho = C$. In table 5.1 the obtained values of C are listed and compared to the respective values of the van der Waals parameter a. A qualitative correlation between the two parameters can be observed: the higher the value of C the higher that of a.

	C $(Pa * m^6/mole^2)$	a $(Pa * m^6/mole^2)$	C/a
Ne	0.158 ± 0.003	0.021	7.52 ± 0.14
$\mathbf{N_2}$	0.95 ± 0.02	0.136	6.99 ± 0.15
$\mathbf{NH_3}$	1.71 ± 0.02	0.423	4.04 ± 0.05
$\mathbf{H_2O}$	1.90 ± 0.03	0.551	3.45 ± 0.05

Table 5.1: *Comparison between the van der Waals parameter a and the constant C: the experimentally determined proportionality coefficient between* Δ_α^2 *and* ρ.

The van der Waals parameter a is related to intermolecular attractive interactions, and quantifies the ability of the system to develop an "internal pressure" which enables it to remain within a well defined volume (see chapter 1). A correlation between C and a therefore suggests a correlation between the physical processes responsible for the "internal pressure" (i.e. the attractive intermolecular interactions) and those responsible for structural relaxation. In the next section, the quantitative analysis of the temperature dependence of τ_α further supports this interpretation.

5.2.2 Timescale of structural relaxation

The temperature dependence of τ_α is reported in Arrhenius plots in fig.5.4. In the liquid phase the temperature dependence of τ_α can be very well described (lines in fig.5.4) with an activation behavior:

$$\tau_\alpha = \tau_0 e^{E_a/k_B T} \tag{5.5}$$

[2]In the case of Neon the data corresponding to 150 and 280 bar have been scaled to the respective density at 200 bar: i.e. $\Delta_\alpha^2 = \Delta_\alpha^2 * \rho(T, 200\ bar)/\rho(T, 150 \text{ or } 280\ bar)$

where E_a is the activation energy of the relaxation process. Using eq.5.5 to describe the experimental data corresponding to the liquid phase, the values of E_a and τ_0 can be derived (see table 5.2).

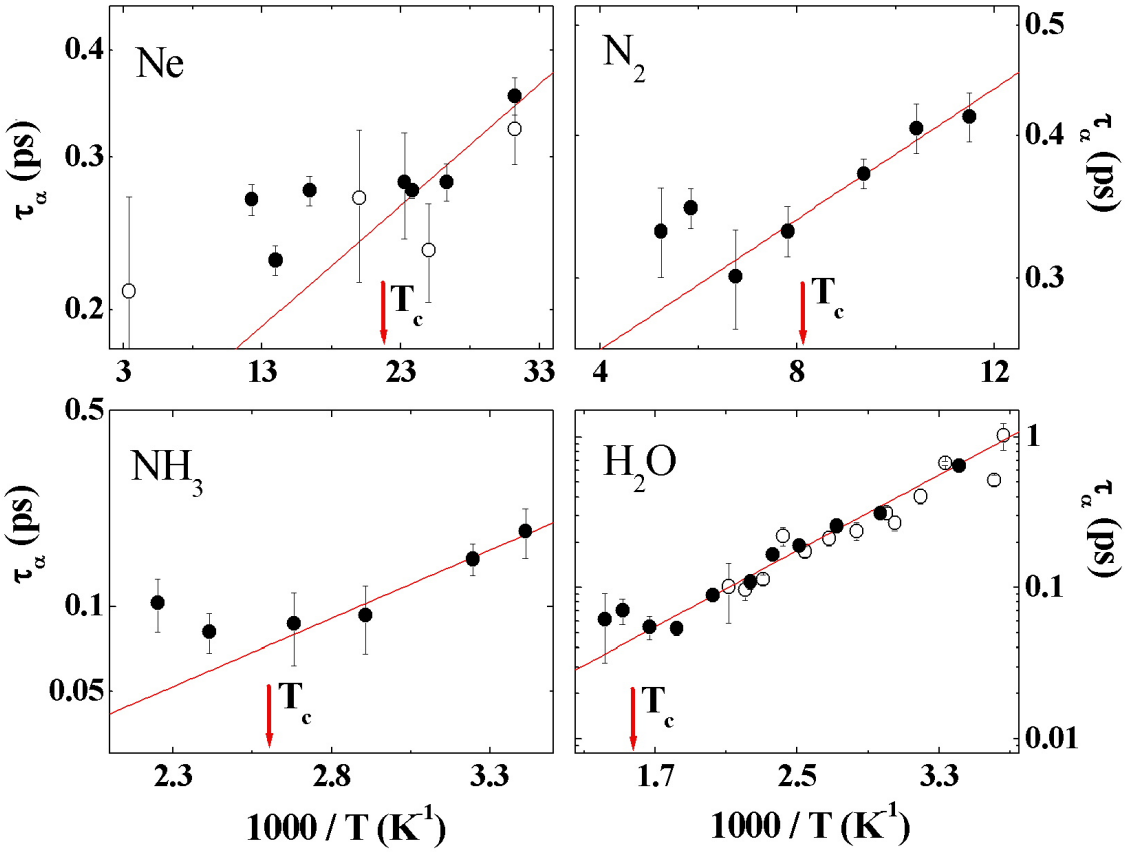

Figure 5.4: *Arrhenius plots of τ_α. The red lines are the best fit results of eq.5.5. The open symbols in the case of neon and water are the results of previous IXS experiments (water: ref.[37]; neon: ref.[38]).*

The obtained activation energies are of the same order as the intermolecular bonding energies. In fact the energy of H-bonds in water, that presents two H-bonds/molecule, is 23 $KJ/mole$ [67]. Considering that ammonia has one H-bond/molecule and that nitrogen is less electronegative than oxygen, one can expect for ammonia an activation energy slightly less than half that one of water ($\sim$ 10 $KJ/mole$). Finally, the van der Waals bonds usually have energies between 0.1 and a few $KJ/mole$, and, moreover, one can suppose that these characteristic energies roughly scale with the critical temperature. One can therefore expect for nitrogen an activation energy a factor 2.5 higher with respect to that of neon. All these estimations are in rather good agreement with the obtained results, listed in table 5.2. This finding fingerprints a correlation between the structural relaxation process and the attractive interactions responsible for intermolecular bonds. In the case of water and neon our data are also compared with the results of previous IXS experiments [37, 38], that were performed at constant density.

Despite the different thermodynamic conditions, the data are in excellent agreement. This evidence strongly suggests that the parameter τ_α does not explicitly depend on density and pressure, at least in the probed portion of the liquid phase. In the case of neon we also report for comparison the data corresponding to the thermodynamic state (32 K and 200 bar) investigated in both experiments.

	E_a $(KJ/mole)$	τ_0 $(10^{-15}\ s)$
Ne	0.27 ± 0.12	130 ± 20
$\mathbf{N_2}$	0.55 ± 0.16	200 ± 20
$\mathbf{NH_3}$	9.3 ± 1.3	4.0 ± 0.8
$\mathbf{H_2O}$	12.0 ± 0.8	4.7 ± 0.3

Table 5.2: *Values of E_a and τ_0 for the investigated samples.*

In the supercritical phase the activation behavior observed in the liquid phase is lost. Here τ_α becomes almost independent of temperature within the accuracy of the presented data.

Concerning structural relaxation, it can be concluded that the relaxation strength is proportional to the density, and it does not explicitly depend on temperature. Moreover, the values of the proportionality constant can be correlated with the van der Waals parameter a, that quantifies the strength of attractive interactions. On the other hand, the comparison between the data of the present work and the ones of previous IXS experiments suggests that, in the liquid phase, the structural relaxation time does not explicitly depend on density and pressure. Moreover, as long as the system is in the liquid phase, the temperature dependence of the relaxation time is characterized by an activation behavior. The associated activation energies have been found to be roughly proportional to the energy of the respective intermolecular bonds.

These observations suggest a close relationship between the structural relaxation process and the intermolecular interactions responsible for the rearrangements of the local structure that, in the liquid phase, can be associated with the continuous making and breaking of intermolecular bonds (attractive interactions). In the supercritical phase, the observed activation behavior of the relaxation time is lost. This can be interpreted as a change in the microscopic mechanisms responsible for the relaxation process. In the next section, some arguments in favor of intermolecular collisions as the main microscopic mechanism ruling the microscopic dynamics in the supercritical phase are provided.

5.2.3 Compliance relaxation time

From the values of the parameters τ_α, c_s and c_∞ the compliance relaxation time, $\tau_C = \tau_\alpha c_\infty^2/c_s^2$, can be calculated. The difference between τ_α and τ_C is well known. τ_α is the characteristic relaxation time of the memory function, corresponding to the characteristic time with which the longitudinal viscosity relaxes. Within the hypothesis of an exponential decay of the memory function, τ_α can be also assumed as the characteristic relaxation time for the longitudinal modulus (M_L). On the other hand,

τ_C represents the relaxation time for the longitudinal compliance: M_L^{-1} [86]. τ_C is also the characteristic timescale associated with the relaxation region located below the Brillouin peak frequency of the $S(Q,\omega)$, i.e. the broad central peak in fig.2.8.

Furthermore, in order to quantitatively compare data sets of different systems, a scaling parameter which allows to account for the different thermodynamic conditions and the different molecules under consideration is needed. One suitable choice is represented by $<\tau>$: the mean free time between intermolecular collisions. In fact, this characteristic time depends on molecular dimensions, masses and shape, as well as on the interaction potential and thermodynamic state of the system. Without involving sophisticated calculations, one can obtain a reasonable value of $<\tau>$ by considering a hard sphere gas obeying the Maxwell-Boltzmann statistics. The first step for this calculation is to assess the average relative velocity of the molecules[3], $<v_{rel}>=\sqrt{2}<v>$, rather than the average velocity of a given molecule[4], $<v>=\sqrt{8k_BT/\pi M}$, where M is the molecular mass. With the molecular diameter, d, the effective cross-section for collision can be regarded as a circle of diameter $2d$. Within a time interval, t, this circle therefore covers an effective volume: $V=\pi\sqrt{2}d^2<v>t$. The average number of collisions is then equal to the number of molecules present in that volume: $N_V=nV$, where n is the number density. Finally, the mean free path, $<\lambda>$, can be assumed as the distance travelled by the molecule, $L=<v>t$, divided by the number of collisions:

$$<\lambda>=\frac{L}{N_V}=\frac{1}{\pi\sqrt{2}d^2n} \tag{5.6}$$

Finally, since the mean free path and the average velocity is known, $<\tau>$ can be easily calculated:

$$<\tau>=\frac{<\lambda>}{<v>}=\frac{1}{n}\sqrt{\frac{M}{16\pi d^4k_BT}} \tag{5.7}$$

$<\tau>$ can be considered as the characteristic time scale for intermolecular interactions in the ideal case of a system made out of particles without an attractive interaction potential. The comparison between this "free-particle" time scale and the experimental values of τ_C is proposed in fig.5.5, where the dimensionless quantity, $\tau_C/<\tau>$[5], is reported as a function of T_c/T. Inspecting this figure one can observe that: i) Close to and above T_c, the absolute value of $\tau_C/<\tau>$ is similar for all four systems. ii) Over the whole temperature range, the data of ammonia and water coincide, as well as those of neon and nitrogen. iii) The temperature dependence of hydrogen bonded (HB) systems can be phenomenologically described by an exponential law: $\tau_C/<\tau>=A_\tau e^{B_\tau T_c/T}$, whose values for A_τ and B_τ are, respectively, 0.49 ± 0.03

[3] $<v_{rel}>$ can be calculated from the identity $v_{rel}=\sqrt{\vec{v}_{rel}\cdot\vec{v}_{rel}}$, where $\vec{v}_{rel}=\vec{v}_2-\vec{v}_1$ is the vectorial difference between the velocities of two colliding particles. Considering that the orientations of $\vec{v}_{1,2}$ are random and uncorrelated, while $<v_1>=<v_2>=<v>$, one easily obtains $<v_{rel}>=\sqrt{2}<v>$.

[4] In calculating $<v>$ a Maxwell-Boltzmann distribution function has been considered.

[5] In the case of nitrogen a value of 3.2 nm for d has been used in the calculation of $<\tau>$. This is probably underestimated, nevertheless it does not influence the temperature and density dependence of $<\tau>$.

and 2.07 ± 0.09 (full line in fig.5.5). iv) Also in the case of neon and nitrogen the temperature dependence of $\tau_C / < \tau >$ can be sufficiently well described by an exponential law, with $A_\tau = 3.47 \pm 0.1$ and $B_\tau = 0.34 \pm 0.05$. However, within the accuracy of the present data, a constant function ($\tau_C / < \tau >= 5.1 \pm 0.5$) is also capable of describing the observed temperature dependence (dashed lines in fig.5.5).

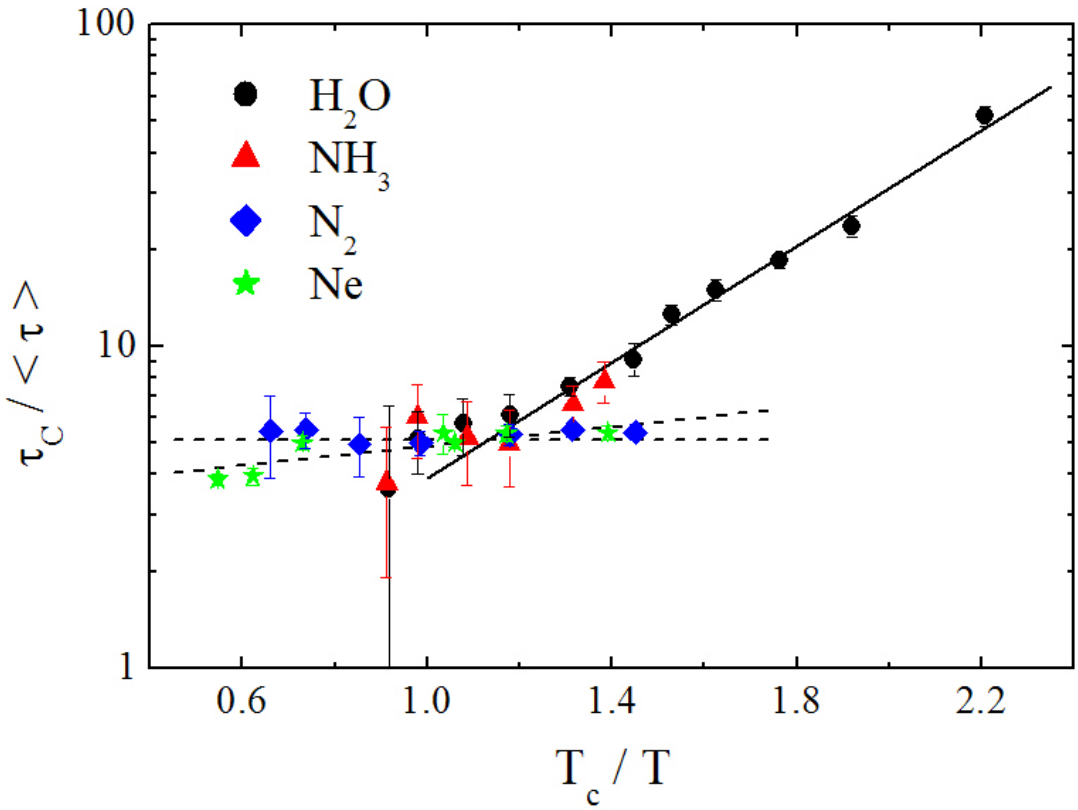

Figure 5.5: *$\tau_C / < \tau >$ as a function of T_c/T. The full line corresponds to best fit result with an exponential law, for the data of water and ammonia. The dashed lines are two possible temperature dependencies (exponential and constant) for the neon and nitrogen data. See text for further details.*

The conclusions one can draw from these observations are:

i) $< \tau >$ can be considered as a reasonable estimation for the relaxation time in the high temperature region of the liquid domain as well as in the supercritical phase. Lowering the temperature τ_C becomes much longer than $< \tau >$ in the case of HB systems. If one associates the values of τ_C (or τ_α) with the typical time scale of intermolecular interactions, the observed temperature dependence of $\tau_C / < \tau >$ can be interpreted in the following way[6]: a) At high temperature (i.e. above T_c) the relaxation time is proportional to $< \tau >$. This suggests that the microscopic dynamics of the system is dominated by intermolecular collisions in this temperature range. b)

[6]The temperature dependencies of τ_α and $\tau_C = (c_\infty / c_s)^2 \tau_\alpha$ are roughly the same since, in a first approximation, both c_s and c_∞ are proportional to the density.

Lowering the temperature, the thermal energy of the molecules is progressively reduced and the molecules can establish a larger number of intermolecular bonds with a longer lifetime, through their attractive interaction potential: i.e. the system is able to develop a more stable network of bonds. Below T_c, this network can provide cohesion among the particles (liquid phase). On the other hand, the larger the number and the lifetime of the bonds, the smaller the probability that two particles can freely collide. In this case the typical time for intermolecular interactions becomes longer, according to the number and the lifetime of these bonds. For sufficiently low temperatures the number and the lifetime of intermolecular bonds can become so large that the particles cannot move at all, and the system falls into a dynamically "frozen" state.

ii) Belove T_c, the data sets of HB and non-HB systems fall into two different curves. This quantitative difference can be ascribed to the different nature of the interaction potential. A stronger attractive interaction potential (like the one of ammonia and water with respect to that of nitrogen and neon) leads to intermolecular bonds with a longer lifetime. As a consequence, the temperature dependence of τ_C in HB systems is expected to be stronger than that of nitrogen and neon. In HB systems, this is reflected in a more pronounced slowing down of the dynamics, with respect to the "free-particle" limit given by $< \tau >$. This quantitative difference disappears above T_c, where the role of the attractive interaction potential on the dynamics is strongly reduced. At these temperatures, the average thermal energy of the molecules is sufficiently high to break intermolecular bonds. The system cannot therefore develop an efficient bond network able to provide the cohesion. From a macroscopic point of view, this is reflected in the fact that a supercritical fluid does not present a specific volume. Unfortunately, the data for HB systems do not extend to very low values of T_c/T. As a consequence, it is difficult to assess whereas $\tau_C/ < \tau >$ follows the same behavior for very low values of T_c/T in the case of HB and non-HB systems.

iii) The data of HB systems coincide once the temperature is scaled for the critical one. It is then possible to associate an activation energy, $\tilde{E}_a = B_\tau k_B T_c$, to the parameter B_τ. Since $\tilde{E}_a$ can be considered as a contribution to the total internal energy, it correctly scales as the critical parameters, in the spirit of the law of corresponding states (see chapter 1). Since the temperature dependence of $\tau_C/ < \tau >$ could be described with an exponential law, the same arguments should also hold for non-HB systems.

To summarize, the behavior of the compliance relaxation time with respect to that of the mean collision time suggests a change in the mechanism responsible for intermolecular interactions. More specifically, at temperatures lower than the critical one, the interactions between molecules are mainly due to bonding. This hypothesis is also supported by the quantitative analysis of the temperature dependence of τ_α shown in the previous section. The lifetime of these bonds decreases with increasing temperature up to become, close to T_c, faster than the average time between two molecular collisions[7]. Above T_c, the characteristic lifetime of the bonds becomes shorter than the average time needed for a given molecule to get close to another one and, eventually,

[7]This characteristic time is calculated for an ideal system, made out of molecules with the same mass, dimension and in the same thermodynamic condition as the real one, but without an attractive interaction potential.

establish an intermolecular bond. In this case the particles cannot develop the network of bonds that is characteristic of the liquid phase. From a microscopic point of view, this is reflected in the fact that the interactions among molecules mainly concern of intermolecular collisions. From the temperature dependence of $\tau_C/ < \tau >$ it is also possible to extract an activation energy, $\tilde{E}_a$, which, if the systems present the same kind of interaction potential, scales with the critical temperature of the system. In order to confirm these conclusions, the analysis should be extended to other systems in a larger range of T_c/T; in particular to lower values of T_c/T for HB systems.

5.3 Instantaneous relaxation

The "instantaneous" relaxation takes into account the dynamical phenomena whose characteristic time scales, τ_μ, are much shorter than the probed frequency window. Owing to its instantaneous nature, any information about the time dependence of the relaxation process are lost. However, it is possible to derive the "integrated" intensity of the process: $\Gamma_\mu(Q)$. Contrary to $\Delta^2_\alpha(Q)$, $\Gamma_\mu(Q)$ does not represent the $t = 0$ value of the respective part of the memory function, but its time-integrated area.

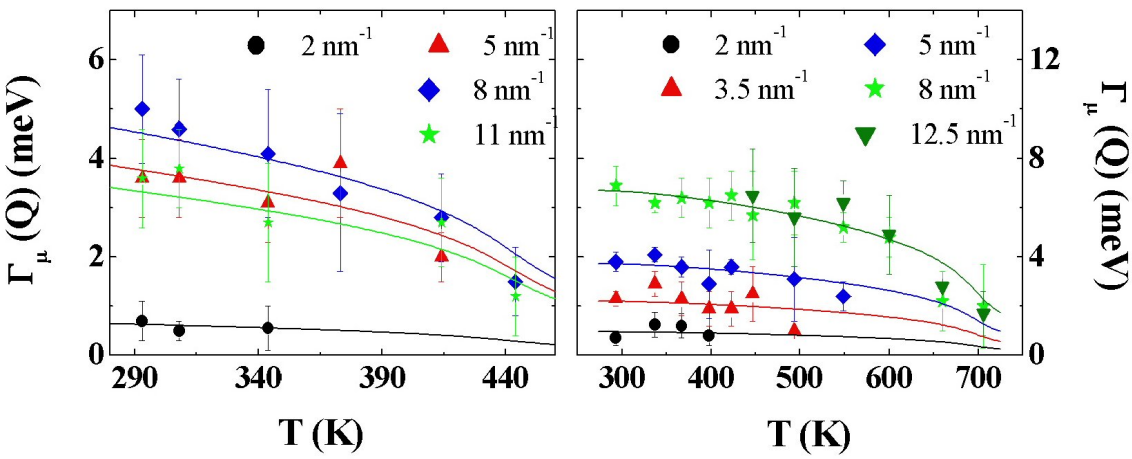

Figure 5.6: *Temperature dependence of* $\Gamma_\mu(Q)$ *in ammonia (left panel) and water (right panel), for some selected Q-values. The lines are functions linearly proportional to the density.*

Inspecting figs.4.21, 4.22 and 4.23, it can be noticed that Water and Ammonia have values of $\Gamma_\mu(Q)$ higher than Nitrogen, whereas negligible values have been obtained for Neon. This first crude observation suggests that this instantaneous relaxation of the memory function is associated with the intramolecular degrees of freedom. In fact Neon (monatomic system) does not possess this kind of degree of freedom. Within the hypothesis that, on shorter time scales, this relaxation process can be described by an exponential decay, its associated strength can be expressed as: $\Delta^2_\mu(Q) = \Gamma_\mu(Q)/\tau_\mu(Q)$. Considering that the characteristic timescales of internal motions, $\tau_\mu(Q)$, are typically unaffected by the thermodynamic conditions, it can be assumed that $\Delta^2_\mu(Q)$ presents

the same behavior as $\Gamma_\mu(Q)$ as a function of the thermodynamic parameters. The temperature dependence of $\Gamma_\mu(Q)$ is reported in fig.5.6 for Ammonia and Water[8]. The solid lines are functions linearly proportional to the density. This figure suggests a linear correlation between the temperature dependence of $\Gamma_\mu(Q)$ and that of density. Since it is expected[9] that $\Delta^2_\mu(Q) \propto \rho$, the fact that $\Gamma_\mu(Q) \propto \rho$ confirms the hypothesis that the characteristic timescale, $\tau_\mu(Q)$, associated to this instantaneous relaxation is almost independent to the thermodynamic parameters, as expected for internal motion in the considered range of temperature and pressure.

Within the hypothesis that $\Gamma_\mu(Q) \propto \rho$, this quantity can be factorized as follows: $\Gamma_\mu(Q) = g(Q)\rho$. Therefore, the function $g(Q)$ accounts for the Q-dependence of $\Gamma_\mu(Q)$. $g(Q)$ can be obtained by averaging all the values of $\Gamma_\mu(Q)/\rho$ for different temperatures at a given Q. The results of this procedure are reported in fig.5.7. It can be appreciated that the Q-dependence of $g(Q)$ agrees quite well with a Q^2 behavior at low Q-values.

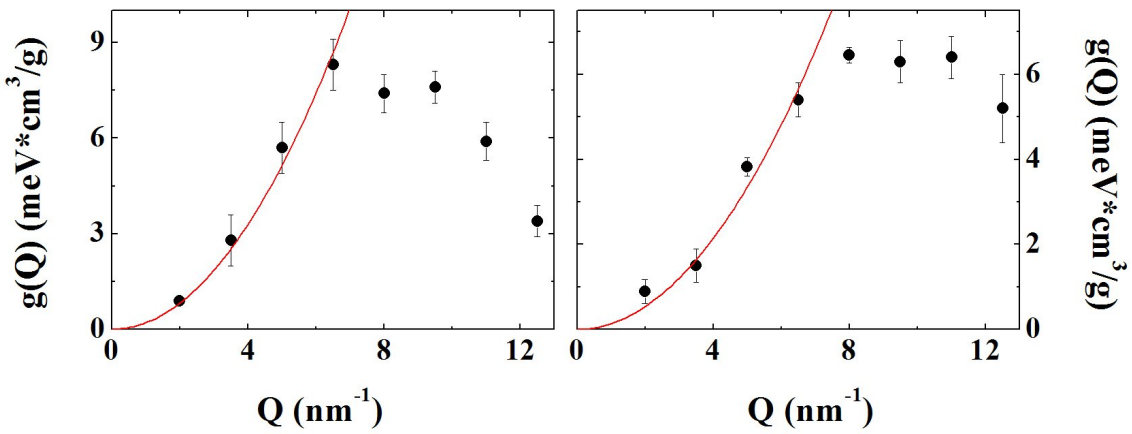

Figure 5.7: *Function $g(Q)$ for ammonia (left panel) and water (right panel). The parabolas are best fit results in the range $0 \div 6.5\ nm^{-1}$.*

[8]The data of Nitrogen are not discussed since they are extremely poorly determined (see fig.4.21), and consequently no $Q-T$ dependencies can be reliably extracted.

[9]In analogy to the considerations made in the previous section for Δ^2_α.

Conclusions

In conclusion, the high frequency dynamics of four prototype systems (Neon, Nitrogen, Ammonia and Water) have been systematic investigated in both the liquid and supercritical phase by means of Inelastic X-ray Scattering (IXS).

The data have been interpreted in the frame of generalized hydrodynamics; in particular, a model based on the memory function has been used.

The obtained results allow the establishment of a common scenario concerning the high-frequency collective dynamics in the liquid and supercritical phase, and the relationship between these dynamics and the most common relaxation processes. Our findings can be summarized as follows:

- The dispersive behavior of longitudinal modes is affected by two competing dispersive effects, namely the positive and negative sound dispersion. These effects can be associated with the structural and the thermal relaxation processes, respectively.

- The temperature and density dependence of the structural relaxation process is the same for all the investigated systems. Specifically: the structural relaxation strength is linearly proportional to the density, while the structural relaxation time -at least in the liquid phase- follows an activation behavior. The associated activation energy is similar to the energy of intermolecular bonds.

- The structural relaxation time systematic becomes shorter than the period of all the allowed longitudinal modes, once the system approaches the critical temperature. At the same time, the structural relaxation strength decreases, according to the decrease of the density. As a consequence of these two combined effects, the influence of the structural relaxation process on the dynamics becomes increasingly smaller. In the supercritical phase, structural relaxation no longer leads to the phenomenon of positive sound dispersion. One can therefore conclude that the phenomenology of positive sound dispersion is a peculiarity of only the liquid phase.

- In the supercritical phase the dispersive behavior of longitudinal modes is mainly ruled by thermal relaxation, owing to the strongly reduced influence of structural relaxation.

- In the supercritical phase the temperature dependence of the structural relaxation time stems from the activation behavior typical of the liquid phase. This

behavior can be interpreted as a change in the nature of the microscopic mechanism responsible for the rearrangements of the local structure: i.e. for structural relaxation. Owing to the fact that the many body dynamics based on intermolecular bonds is expected to be less effective in the supercritical phase, it can be supposed that the intermolecular interactions are mainly based on intermolecular collisions. Therefore, in the supercritical phase, a more suited relaxation time for the characterization of the microscopic rearrangements of the local structure is represented by the mean free time between two intermolecular collisions, rather than the activation behavior related to the bonding energy. This supposition is also supported by the observed behavior of the compliance relaxation time.

- The instantaneous relaxation can mainly be associated with an early stage time decay of the memory function induced by fast intramolecular dynamics such as intramolecular vibrations. This can be evinced from the fact that Neon, which is a monatomic liquid and does not possess this kind of dynamics, presents a negligible instantaneous contribution. Moreover, this contribution does not explicitly depend on temperature, since it has been found to be directly proportional to the density.

- Finally, the main result of this thesis work is represented by the generality of the scenario depicted above. In fact, these results can be considered as valid for a large class of simple systems, ranging from monatomic to molecular H-bonded liquids.

Conclusions

En conclusion, par la Diffusion Inélastique de Rayons-X (IXS), nous avons effectué une étude systématique de la dynamique aux hautes fréquences de quatre systèmes : le Néon, l'Azote, l'Ammoniaque et l'Eau, dans les phases liquide et supercritique. Ces systèmes ont été choisis parce qu'ils peuvent être considérés comme caractéristiques de classes de fluides, en ayant des intéractions intermoléculaires différentes.

Les données expérimentales ont été interprétées dans le cadre de l'hydrodynamique généralisée, en particulier un modèle basé sur la fonction de mmoire a été utilisé. La fonction mémoire proposée contient trois différents modes d'atténuation temporelle (c'est-à-dire les relaxations). Ces processus de relaxation sont : i) la diffusion thermique qui, par le flux de chaleur, tend à homogénéiser la température des zones comprimées et raréfiées. Ce mécanisme engendre le processus de relaxation thermique de la fonction mémoire. ii) Les dissipations visqueuses survenant sur un temps fini, par rapport à la fenêtre expérimentale employée. Ce mécanisme a été interprété comme un échange d'énergie entre l'excitation acoustique et les degrés de liberté intermoléculaires. Ces derniers décrivent les actions réciproques intermoléculaires qui, dans la phase liquide, ont une nature collective : le processus de relaxation associé à ces dynamiques est communément appelé relaxation structurelle. iii) Les dissipations visqueuses instantanées. Ce mécanisme peut représenter des phénomènes dynamiques survenant avec des temps caractéristiques beaucoup plus brefs que la fenêtre expérimentale utilisée (par ex., dans notre cas, les vibrations intramoléculaires rapides); ce mécanisme peut aussi représenter des échanges d'énergie causés par le désordre topologique. Le processus de relaxation relatif à ces mécanismes est usuellement appelé relaxation instantanée.

Les résultats obtenus permettent l'établissement d'un scénario commun concernant la dynamique collective à haute fréquence dans la phase liquide et supercritique, les relations entre cette dynamique et les processus de relaxation les plus communs, et aussi la dépendance des processus de relaxation aux variables thermodynamiques.

Nos conclusions peuvent être résumées comme suit :

- Le comportement dispersive des modes longitudinaux est affectée par deux effets concurrents, c'est-à-dire la dispersion positive et négative. La dispersion positive, lorsque Q augmente, fait augmenter la valeur de la vitesse du son, de la valeur adiabatique jusqu'à sa valeur à haute fréquence (c_∞). Au contraire, la dispersion négative, lorsque Q croît, fait diminuer la vitesse du son de la valeur adiabatique jusqu'à sa valeur isothermique. Ces effets dispersifs peuvent être associés, respectivement, aux processus de relaxation structurelle et thermique. Dans la phase liquide, l'effet dispersif principal est représenté par la dispersion positive, associée

à la relaxation structurelle. Cet effet devient plus faible dès que le système approche les conditions supercritiques. Dans la phase supercritique l'effet de la dispersion négative devient comparable à celle de la dispersion positive.

- La dépendance de la densité et de la température du processus de relaxation structurelle est la même pour tous les systèmes examinés. En particulier : la force de la relaxation structurelle est proportionnelle à la densité, tandis que les temps de relaxation structurelle, au moins dans la phase liquide, suivent une loi d'activation. L'énergie d'activation associée est semblable à l'énergie des liens intramoléculaires.

- Une fois que le système approche la température critique, le temps de relaxation structurelle devient systématiquement plus court que la période de tous les modes longitudinaux permis. En même temps la force de la relaxation structurelle diminue avec la densité. Comme conséquence de ces deux effets combinés, l'influence du processus de relaxation structurelle sur la dynamique devient de plus en plus petite. Dans la phase supercritique, elle ne cause plus le phénomène de la dispersion positive. On peut donc conclure que la phénoménologie de la dispersion positive est une particularité de la phase liquide uniquement.

- Du fait de l'influence fortement réduite de la relaxation structurelle, dans la phase supercritique le comportement dispersif des modes longitudinaux peut être gouverné par la relaxation thermique.

- Dans la phase supercritique la dépendance en température des temps de relaxation structurelle ne suit plus la loi d'activation typique de la phase liquide. Plus spécialement, sa dépendance en température devient plus faible. Ce comportement peut être interprété comme un changement dans la nature du mécanisme microscopique responsable des réarrangements de la structure locale : c'est-à-dire la relaxation structurelle. Du fait que l'on s'attend à ce que la dynamique à nombreux corps, basée sur les liens intermoléculaires, devienne moins efficace dans la phase supercritique, on peut penser que les intéractions intermoléculaires sont fondées surtout sur les collisions. Donc, un temps de relaxation plus convenable pour décrire ce processus est représenté par les temps moyens entre deux collisions intermoléculaires, plutôt que la conduite d'activation caractérisée par l'énergie des liens. Cette supposition est confortée par les valeurs obtenues du temps de relaxation de la compliance.

- La relaxation instantanée peut être principalement associée à une première atténuation temporelle de la fonction mémoire, induite par la dynamique intramoléculaire rapide, comme les vibrations intramoléculaires. Cela peut être montré du fait que le Néon, qui est un liquide monoatomique et donc peut avoir cette sorte de dynamique, présente une contribution instantanée négligeable. De plus, cette contribution ne dépend pas explicitement de la température, mais est proportionnelle à la densité.

- Enfin, le résultat principal de ce travail de thèse est représenté par la généralité du scénario expliqué ci-dessus. En fait, ces résultats peuvent être considérés comme valides pour une grande classe de systèmes simples, qui embrassent les systèmes monoatomiques jusqu'aux liquides moléculaires simples avec liaisons hydrogènes, dans toute la phase fluide thermodynamiquement stable.

Bibliography

[1] Aristoteles, "*Physica*" (367 B.C.).

[2] K.P. Johnstone and P.S. Shah, *Science* **303**, 482 (2004).

[3] J.M. DeSimone, *Science* **297**, 799 (2002).

[4] M.M. Kirchhoff, *Environ. Sci. Technol.*, **37**, 5349 (2003).

[5] B.J. Berne and R. Pecora, "*Dynamic Light Scattering*", John Wiley & Sons, New York (1976).

[6] R.N. Silver and P.E. Sokol, "*Momentum Distributions*", Plenum Press, New York (1989).

[7] J.P. Boon and S. Yip, "*Molecular Hydrodynamics*", McGraw-Hill International Book Company, New York (1980).

[8] U. Balucani and M. Zoppi, "*Dynamics of the liquid state*", Clarendon Press, Oxford (1994).

[9] P. Herenfest, Supplement No. 75b zu den Mitteilungen aus dem Kamerlingh Onnes-Institut, Leiden (1933).

[10] G.F. Mazenko, "*Equilibrium Statistical Mechanics*", John Wiley & Sons, New York (2000).

[11] R. Brout, "*Phase Transitions*", W.A. Benjamin Inc., New York (1965).

[12] R. Kubo, *Rep. on Progr. Phys.*, **29**, 255 (1966).

[13] L. Van Hove, *Phys. Rev.*, **95**, 249 (1954).

[14] F. Coester, *Phys. Rev.*, **84**, 1259 (1951).

[15] R. Bansal and K.N. Pathack, *Phys. Rev. A*, **9**, 2773 (1974).

[16] R. Bansal and K.N. Pathack, *Phys. Rev. A*, **11**, 724 (1975).

[17] R. Bansal and K.N. Pathack, *Phys. Rev. A*, **15**, 2519 (1977).

[18] R. Bansal and K.N. Pathack, *Phys. Rev. A*, **15**, 2531 (1977).

[19] T. Scopigno, G. Ruocco and F. Sette, *Rev. of Mod. Phys.*, **77**, 881 (2005).

[20] Rytov S.M., *Sov. Phys.:* JEPT, **31** (1970) 1163.

[21] J. Markham, R.T. Beyer and R.B. Linsday *Rev. Mod. Phys.* **23** 353 (1951).

[22] D. Sette, in "*Encyclopedia of Physics*", edited by Flügge S., Vol. "Acoustic I and II" (Springer-Verlag, Berlin) 1969.

[23] E. Herzfeld and T.A. Litovitz, in *Absorption and Dispersion of Ultrasonic Waves*, (Accademic Press, New York) 1959.

[24] M. Haluska, D. Havlik, G. Kirlinger and W. Schranz, *J. Phys.: Condens. Matter*, **11**, 1009 (1999)

[25] F. Bencivenga, A. Cunsolo, M. Krisch, G. Monaco, G. Ruocco and F. Sette, *Eurohys. Lett.* , **75**, 70 (2006).

[26] J. Frenkel and J. Obraztsov, *J. Phys. URSS*, **3**, 131 (1940); *J. Exptl. Theor. Phys. URSS*, **9**, 1081 (1939)

[27] J.J. Markham, *J. Acoust. Soc. Am.*, **22**, 628 (1951)

[28] L. Hoff, *J. Acoust. Soc. Am.*, **23**, 12 (1951)

[29] G.D. Patterson, G.R. Alms and C.P. Lindsey, *J. Chem. Phys.*, **69** 4802 (1978).

[30] G. Fytas, C.H. Wang, D. Lilge and Th. Dorfmüller, *J. Chem. Phys.*, **75** 4247 (1981).

[31] M.G. Sceats and J.M. Dawes, *J. Chem. Phys.*, **83** 1298 (1985).

[32] W. Götze, L. Sjogren, *Rep. Prog. Phys.*, **55**, 241 (1992)

[33] A.R. Dexter and A.J. Matheson, *J. Chem. Phys.*, **54** 3463 (1971).

[34] Y.H. Jeong, S.R. Nagel and S. Bhattacharya, *Phys. Rev. A*, **34** 602 (1986).

[35] Y. Yang and K. Nelson, *J. Chem. Phys.*, **103** 7732 (1995).

[36] D. Fioretto, U. Buchenau, L. Comez, A. Sokolov, C. Masciovecchio, A. Mermet, G. Ruocco, F. Sette, L. Willner, B. Frick, D. Richter and L. Verdini, *Phys. Rev. E*, **59** 4470 (1999).

[37] G. Monaco, A. Cunsolo, G. Ruocco and F. Sette, *Phys. Rev. E*, **60** 5505 (1999).

[38] A. Cunsolo, G. Pratesi, R. Verbeni, D. Colonnesi, C. Masciovecchio, G. Monaco, G. Ruocco and F. Sette, *J. Chem. Phys.*, **114** 2259 (2001).

[39] G. Ruocco and F. Sette, *J. Phys.: Condens. Matter*, **11** R259 (1999).

[40] R. Angelini, P. Giura, D. Fioretto, G. Monaco, G. Ruocco and F. Sette, *Phys. Rev. B*, **70** 224302 (2004).

[41] E. Pontecorvo, M. Krisch, A. Cunsolo, G. Monaco, A. Mermet, R. Verbeni, F. Sette and G. Ruocco, *Phys. Rev. E*, **71** 011501 (2005).

[42] A. Giugni and A. Cunsolo, *J. Phys.: Condens. Matter* **18**, 889 (2006).

[43] G. Monaco, D. Fioretto, C. Masciovecchio, G. Ruocco and F. Sette, *Phys. Rev. Lett.* **82**, 1776 (1999)

[44] G. Ruocco, F. Sette, R. di Leonardo, G. Monaco, M. Sampoli, T. Scopigno and G. Viliani, *Phys. Rev. Lett.*, **84**, 5788 (2000).

[45] D. Fioretto, L. Comez, G. Socino, L. Verdini, S. Corezzi, and P.A. Rolla, *Phys. Rev. E*, **59** 1899 (1999).

[46] A. Monaco, T. Scopigno, P. Benassi, A. Giugni, G. Monaco, M. Nardone, G. Ruocco, and M. Sampoli, *J. Chem. Phys.*, **120** 8089 (2004).

[47] T. Scopigno, U. Balucani, A. Cunsolo, C. Masciovecchio, G. Ruocco, F. Sette and R. Verbeni, *Europhys. Lett.*, **50** 189 (2000).

[48] E. Burkel, "*Inelastic Scattering of X-Rays with Very High Energy Resolution*", Springer-Verlag, (1991).

[49] E. Burkel, *Rep. Prog. Phys.*, **63**, 171 (2000)

[50] P.A.M. Dirac, "*The principles of quantum mechanics*", Oxford University Press, Oxford (1958).

[51] E.R. Pike and S. Sarkar, "*The quantum theory of radiation*", Oxford University Press, Oxford (1995).

[52] J.J. Sakurai, "*Modern Quantum Mechanics. Revisited Edition*", Addison-Wesley Publishing Company (1994).

[53] W. Marshall and S. W. Lovesey, "*Theory of Thermal Neutron Scattering*", Clarendon Press, Oxford (1971).

[54] W. Schulke W, "*Inelastic scattering by electronic excitations*", in Vol. 3 of "*Handbook on Synchrotron Radiation*", G. Brown and D.E. Moncton, Elsevier Science Publications (1991).

[55] S. Takeno and M. Gôda, *Prog. Theor. Phys.*, **45**, 331 (1971)

[56] S. Takeno and M. Gôda, *Prog. Theor. Phys.*, **47**, 790 (1972)

[57] M. Gôda, *J. Phys. C*, **6**, 3047 (1973)

[58] M. Krisch, *J. Raman Spectrosc.*, **34**, 628 (2003)

[59] R. Verbeni, F. Sette, M. Krisch, U. Bergmann, B. Gorges, C. Halcoussis, K. Martel, C. Masciovecchio, J.F. Ribois, G. Ruocco, H. Sinn, *J. Synchrotron Radiat.*, **3**, 62 (1996)

[60] C. Masciovecchio, U. Bergmann, M. Krisch, G. Ruocco, F. Sette, R. Verbeni, *Nucl. Instrum. Methods. B*, **111**, 181 (1996)

[61] C. Masciovecchio, U. Bergmann, M. Krisch, G. Ruocco, F. Sette, R. Verbeni, *Nucl. Instrum. Methods. B*, **117**, 339 (1996)

[62] A. Bergamini, G. Cavagnero and G. Mana, *J. Appl. Phys.*, **82**, 5396 (1997)

[63] Nova Swiss, Cesson, France.

[64] Epothech, Taichung, Taiwan.

[65] Cryomech, Syracuse (NY), USA.

[66] Top-Industry, Vaux le Penil, France.

[67] F. Franks, "*Water: a comprehensive treatise*", Plenum Press, New York (1972).

[68] MINUIT, D516-CERN, Computer 7600, Interim Program Library.

[69] R. Torre, P. Bartolini and R. Righini, *Nature* (London), **428**, 296 (2004).

[70] C. Masciovecchio, S.C. Santucci, A. Gessini, S. Di Fonzo, G. Ruocco and F. Sette, *Phys. Rev. Lett.*, **92**, 255507 (2004).

[71] C. Petrillo, F. Sacchetti, B. Dorner and J.B. Suck, *Phys. Rev. E*, **62**, 3611 (2000)

[72] F. Sacchetti J.B. Suck, C. Petrillo and B. Dorner, *Phys. Rev. E*, **69**, 061203 (2004)

[73] F. Sette, G. Ruocco, M. Krisch, C. Masciovecchio, R. Verbeni and U. Bergmann, *Phys. Rev. Lett.*, **77**, 83 (1996)

[74] M. Sampoli, G. Ruocco and F. Sette, *Phys. Rev. Lett.*, **79**, 1678 (1997)

[75] International tables for X-ray crystallography, Kynoch press, (1962).

[76] T. Scopigno, U. Balucani, G. Ruocco and F. Sette, *Phys. Rev. Lett.*, **85**, 4076 (2000)

[77] T. Scopigno, U. Balucani, G. Ruocco and F. Sette, *Phys. Rev. E*, **65**, 031205 (2002)

[78] T. Scopigno, G. Ruocco, F. Sette and G. viliani, *Phys. Rev. E*, **66**, 031205 (2002)

[79] C.M. Davis and T.A. Litovitz, "*Physical Acoustics*", W.P. Mason, New York (1969).

[80] J. Rouch, G.C. Lai and S.H. Chen, *J. Chem. Phys.*, **65**, 4016 (1976).

[81] J.O. Hirschfeld, C.F. Curtiss and R.B. Bird, "*Molecular Theory of Gasses and Liquids*", John Wiley & Sons, New York (1954).

[82] A. Cunsolo and N. Nardone, *J. Chem. Phys.*, **105**, 3911 (1996).

[83] F. Huth, *Cryogenics*, **3**, 368 (1962)

[84] D.G. Naugle, *J. Chem. Phys.*, **44**, 741 (1966).

[85] A.A. van Well and L.A. de Graaf, *Phys. Rev. A*, **32**, 2396 (1985).

[86] G. Harrison, "*The dynamic properties of supercooled liquids*", Academic Press, New York (1976).

Résumé

Cette thèse concerne une étude expérimentale sur la dynamique microscopique dans quatre systèmes prototypes (c'est-à-dire : le Néon, l'Azote, l'Ammoniaque et l'Eau) dans leurs phases liquide et supercritique. La technique expérimentale utilisée a été la diffusion inlastique des rayons-X (IXS). Le facteur de structure dynamique cohérent, $S(Q, \omega)$, a été déterminé dans une gamme de moment transférés, Q (2 - 15 nm^{-1}), et de fréquences, ω (1 - 60 THz), correspondant à les longueurs et à des temps caractéristiques de la dynamique microscopique dans le régime des nanomètres et des picosecondes. Les données expérimentales ont été interprétées dans le cadre de la théorie hydrodynamique généralisée. Ce formalisme permet d'identifier les processus de relaxation qui décrivent la dynamique microscopique du système et de fournir des valeurs quantitatives pour les temps et les forces des processus de relaxation. Il est aussi possible de déterminer des quantités macroscopiques comme la vitesse du son et la viscosité. En allant de la phase liquide à la phase supercritique, une phénoménologie commune a été qualitativement observée. Les conclusions principales sont les suivantes : (i) Un affaiblissement de la dispersion positive associée à la relaxation structurelle. (ii) Un changement dans les mécanismes principaux responsables des interactions intermoléculaires à un niveau microscopique. Dans la phase liquide les interactions intermoléculaires sont surtout des liens intermoléculaires, d'autre part, dans la phase supercritique, ces interactions sont dominées par les collisions intermoléculaires.

Mots clés: processus de relaxation, diffusion inélastique de rayons X, phase supercritique, dynamique microscopique.

Summary

The thesis reports an experimental investigation of the microscopic dynamics in four prototype systems (i.e. Neon, Nitrogen, Ammonia and Water) in their respective liquid and supercritical phase, utilising inelastic X-ray scattering (IXS). The coherent dynamic structure factor, S(Q,) was determined in the momentum transfer, Q (2 - 15 nm^{-1}), and a frequency, ω (1 - 60 THz), range corresponding to characteristic length and time scales of the microscopic dynamics in the nanometers and picoseconds regime. The experimental data have been interpreted in the framework of the generalized hydrodynamic theory. This formalism allows identifying the relaxation processes describing the intermolecular interactions, and provides quantitative values for the relaxation times and strengths, as well as related macroscopic quantities (sound speed and viscosity). On going from the liquid into the supercritical phase, a qualitative common phenomenology has been observed. The main findings are the following: (i) A weakening of the positive sound dispersion associated to the structural relaxation. (ii) A change in the dominant microscopic mechanism responsible for intermolecular interactions that, in the liquid phase, are mainly represented by bonds while, in the supercritical phase, are dominated by intermolecular collisions.

Key words: Relaxation processes, inelastic X-ray scattering, supercritical phase, microscopic dynamics.